Australian Government

Department of Defence

Defence Science and
Technology Organisation

The Safety of Aircraft Exposed to Electromagnetic Fields: HIRF Testing of Aircraft using Direct Current Injection

Chris Leat

Air Operations Division
Defence Science and Technology Organisation

ABSTRACT

Even the original developers of Bulk Current Injection now make the point that the use of BCI at aircraft level will become increasingly difficult. Direct Current Injection has the potential to replace aircraft level BCI, while also solving many of the longstanding problems of BCI. These problems include lack of synergism, inaccurate current distribution within bundles and limited numbers of injection sites due to time and cost considerations. However, calibration, the question of how much power to apply as a function of frequency, is much more complex to answer for DCI than BCI. One potential method of calibration, the use of modal skin currents, is developed in this work. This is the first time that DCI calibrated using skin-currents has been shown to generate cable currents which are at least as accurate as BCI. Power levels of approximately 20 kW are required for small aircraft. Numerical modelling based on Method of Moments, and skin and bundle current measurements are employed.

RELEASE LIMITATION

Approved for public release

APPROVED FOR PUBLIC RELEASE

The Safety of Aircraft Exposed to Electromagnetic Fields: HIRF Testing of Aircraft using Direct Current Injection

Executive Summary

Military aircraft require testing to ensure they are safe and mission effective when in radio wave fields in the High Frequency (HF: 1-30MHz) range of up to 200V/m. A primary means of doing this High Intensity Radiated Field (HIRF) testing is known as Low Level Swept Current (LLSC) and Bulk Current Injection (BCI), where numerous wiring looms have a current transformer clamped around them in order to induce the Radio Frequency (RF) currents on the current looms. This method has had systematic faults since its introduction but is also now becoming difficult to apply due to loom access difficulties on modern aircraft. A promising alternative known as Direct Current Injection (DCI) places the currents onto the aircraft skin rather than the looms, but it has proven challenging to determine how much current to inject onto the aircraft skin, and where exactly it should be injected.

In this work, a novel method of controlling the skin currents was proposed and tested. Firstly, phased skin current density samples were taken at 14 locations on a Macchi aircraft. These were used to validate LLSC and DCI numerical electromagnetic models of the Macchi aircraft. These numerical models were then subject to eigencurrent analysis; a method of reducing the complex skin current distributions to a small number of independent modal current distributions. Three of these modal current distributions were then used to control the amount of power applied to the DCI sites on the aircraft. The currents on cable bundles were finally compared using DCI controlled in this manner against an accepted method, LLSC.

It was found that for most cable bundles the DCI generated cable bundle currents equalled or exceeded the maximum envelope of the LLSC cable bundle currents taken over the 8 antenna polarisations and positions. The typical difference seen between the LLSC maximum bundle current envelope and the DCI bundle current was of the order 6dB.

DCI has inherent advantages over BCI including simultaneous stressing of redundant systems, speed of testing and effectively testing all cable bundles, rather than a select few. A disadvantage of DCI is the high amplifier power required. This work found for the case of the Macchi aircraft, that 20kW would be required for a planar ground plane test at 200V/m horizontal polarisation. However 10kW would provide 200V/m over most of the HF range, and 175V/m from 10MHz-16MHz. Similar power levels would be required for most helicopters and fighter aircraft.

Authors

Dr Chris Leat
Air Operations Division

Dr Leat has a PhD in Computational Electromagnetics from the University of Queensland. He worked as a Postdoctoral Fellow at the University for three years in UXO detection theory and has a joint patent in Ground Penetrating Radar system design. He has been working in Electromagnetic Environmental Effects at DSTO since June 2002.

Contents

1. Introduction

Intersystem HIRF (High Intensity Radiated Field) testing consists of a variety of techniques, having varying levels of fidelity, which together attempt to simulate the effects on an aircraft avionics of flying in the propagating electromagnetic fields of Radio Frequency (RF) transmitters.

The testing consists partly of tests at the LRU[1] level, where the LRU is exposed to radio frequency free-space plane-wave propagating fields (Radiated Susceptibility) and guided-wave propagating fields on cables (Conducted Susceptibility). These tests have the advantage of small test volume requirements and thus can be conducted fairly inexpensively indoors using as much of the spectrum as desired with modest RF powers. A great strength of the LRU testing is the thoroughness with which the spectrum is covered. A weakness in the LRU tests are the assumed levels[2] of coupling between the fields external to the aircraft and the reverberant plane-wave and guided-wave environment where the LRUs are located, which depends on many factors of aircraft design and equipment installation. In principle these coupling factors can be measured. But, due to the sequence of subsystem and system development, the LRU testing often occurs prior to aircraft development, and generic levels of coupling factors and aircraft external environment are assumed when testing the LRUs. However, LRU testing is an essential part of a modular approach to HIRF compatibility.

An additional phase of testing may then be required when the aircraft is assembled or following significant modification. This whole-aircraft testing seeks to apply a test RF environment roughly[3] equivalent to that which the aircraft will be exposed in operations. At frequencies greater than 30 MHz, plane-wave fields are impinged upon the aircraft exterior. This may be done to a sequence of sub-regions of the aircraft surface, by movement of the antenna footprint, in an Open Area Test Site (OATS) or Anechoic Chamber (AC); or, it may be done in a Reverberation Chamber (RC), where a large fraction of the aircraft surface is simultaneously exposed to a random simultaneous set of plane wave fields. In the reverberation chamber, unexposed regions are exposed in turn by random changes in the plane-wave mix as the stirring device is used. Discussion of the relative merits of these two basic methods is beyond the scope of this report.

Below 30 MHz, the wavelengths are too long to make illumination of a sub-region of the aircraft practical, or to support sufficient non-evanescent standing waves in a reverberation chamber. Three methods are used below 30 MHz, and a further three are experimental:

- Full Field (mostly) Vertical Polarised (FFVP). The United States' NAVAIR, Patuxent River has a V dipole/monopole antenna with reflector elements which can expose a whole aircraft to vertical polarised fields in the order of 100V/m [1]. Very large input powers are required by reason of the large area over which the Poynting flux is spread: A 300 kW amplifier is used. Spectrum limitations must be observed. Approximately twenty frequency points are available typically. The low strength of

---

1 Line Replacement Unit or "box".

2 The generic coupling levels from plane wave to cable currents have been based on the highest levels from measurements of numerous aircraft in the past.

3 The equivalence might be rough due to compromises on the number of frequencies used and angles of illumination for example. The test field may exceed the operational fields by a test margin.

horizontally polarised fields is a significant factor in this method not achieving complete equivalence to the environment encountered when flying. Although the antenna may be phased to provide a horizontally polarised wave, the field levels available near the ground are relatively low, due to the ground plane shorting effects. Similar systems are used in the United Kingdom and France.

- Full Field Horizontal Polarised. (FFHP) It has been reported to the author that EADS have a HIRF facility at Manching, Germany, where fighter sized aircraft can be elevated to a height of around 60m on a wooden tower. This would eliminate the field shorting problems mentioned above, but would still require very large powers to achieve circa 200 V/m.

- Low Level Swept Coupling – Bulk Current Injection (LLSC-BCI). The intent of this method is to revisit the LRU conducted susceptibility testing by actually measuring the coupling between the external plane-wave field and the LRU cable currents, and then injecting the appropriate currents on the cables with the LRUs in-situ. This is done on an OATS. (It is not yet practical to numerically model the entire aircraft including the internal cabling and features to obtain these coupling figures.) One strength of this method is the very modest RF power requirement (<1 kW). This enables the use of inexpensive, relatively safe, linear amplifiers that don't require tuning. Furthermore, it is possible to use BCI at any frequency selected without spectrum limitations, as the cables don't radiate significantly. The main weakness of the method is that it is not practical for cost and accessibility reasons to measure and inject all individual cables entering all LRUs independently. Thus a limited number of *bundled* cables are measured and injected at a limited number of locations. In many cases it may be impossible to obtain physical access to inject important cable bundles. The result of injecting onto bundles is that the test engineer has no control over the relative distribution of currents on the individual cables inside the bundle. For example, a measured current might be predominantly contributed by one cable in a bundle. However the reinjected currents will be spread over all the cables in proportion to their insertion loss [2]. This can result in errors of order 20 dB [3]. Another problem with this method is the usual lack of simultaneous stressing of subsystems. It may be, for example, that a system has multiple redundant parts, which will mask the interference on any one system. In a real situation, however, the cables all experience interference simultaneously. Much work has been reported considering the challenges of achieving realistic EUT stress using LLSC-BCI, for example [4-6] in addition to those already cited.

- Low Level Swept Coupling - Direct Current Injection (LLSC-DCI) [7]. In this method, the cable bundle currents are measured subject to a plane wave field on an OATS, the same as in LLSC-BCI. However, instead of reinjecting currents into the cable bundles, the aircraft nose, tail and wings may be subject to RF injection or loading, known as DCI. The bundle currents are again measured subject to the low level current injection onto the nose, tail wingtips etc. The two coupling measurements are then used to calibrate the required full field equivalent DCI levels required. Independent control of the bundle currents can't be achieved, however the strength of this method is that, to the extent skin currents are accurate, all LRU cables are suitably and simultaneously RF excited. Unlike the FFVP method, horizontal polarisation is taken account of by this method. Powers of the order 10-100 kW are required to achieve equivalence to 200 V/m. This can be further reduced using a conformal earth return rig [8].

Significant incidental power radiation to space occurs, which together with the requirement for tuned power amplifiers, means that limited test frequencies are practical. The method is briefly mentioned in reference [9] and more thoroughly in reference [10].

- Skin Current Swept Coupling –Direct Current Injection (SCSC-DCI). This method approaches the Direct Current Injection calibration through considering the aircraft skin currents – either measured or modelled – rather than the cable bundle currents. The benefits relative to LLSC-DCI are that the inconvenience and inaccuracy of LLSC measurements made on a ground plane may be avoided though modelling, and that the skin currents, by being explicitly considered may be manipulated to better resemble the real situation. Thus LRU cable currents may better resemble the real world. Like the LLSC-DCI, FFHP and FFVP methods the power requirements are large (10-100 kW) and frequency test points are limited if conducted outdoors, or without an effective earth return rig. This method has not been conducted successfully prior to now, and is the objective of the work described in this report. It has been proposed for the case of missile HIRF testing [10].

- Whole Aircraft TEM cells. These are a separate area of investigation at DSTO [11]. No full scale testing has yet been performed. Benefits include lack of radiation into space and, in the case of hybrid RC/TEM cells, a test location that may serve multiple band requirements, reducing the requirement to move the aircraft. However, power requirements are expected to be similar to DCI and horizontal polarisation is challenging. TEM cell resonances and limited test volume are likely problems, and are areas of particular research at DSTO.

This report describes work aimed at developing the SCSC-DCI method. Previously, a reference was made to the potential for achieving more realistic skin currents if they are the means of the calibration, rather than being ignored. The emphasis in this work was therefore placed on understanding the RF skin currents and thus developing a conceptual framework for controlling the skin currents using the DCI method. This methodology was trialled at low signal levels on a Macchi aircraft. The report layout is as follows:

- Section 2 describes a method adapted by the author to conveniently understand the complex pattern of RF currents occurring on the skin of a jet trainer aircraft in the range 1-30 MHz. This method divides the current modes into two types; a capacitive type which flows between charge concentrations and an inductive type which flows in closed loops, without charge concentrations.

- Section 3 applies the method developed in Section 2 to understand the skin currents on a Macchi aircraft when flying in free space and subject to incident plane waves in the range 1-30 MHz from above, beside and in front and with two orthogonal polarisations. Airframe resonances will be clearly shown to exist in the capacitive type modes and circulating type modes will be shown to occur at low and uniform levels with frequency. The inadequacy of using vertical polarisation alone to test an aircraft will be clear from this section.

- Section 4 applies the method of Section 2 to understand the skin currents present on a Macchi aircraft when on an Open Area Test Site when conducting LLSC measurements. It will be shown that the skin currents are significantly different to the

free-space case due to the presence of the conductive ground plane. Measurements are used to validate the modelled results.

- Section 5 applies the method of Section 2 to the skin currents excited using a variety of DCI topologies.

- Section 6 takes a promising DCI topology, and the capacitive mode currents are used to control the direct injected current to achieve approximate equivalence to the LLSC situation. Measurements of cable bundle currents achieved using SCSC-DCI are compared to the cable bundle currents achieved using conventional LLSC. The required power to achieve DCI equivalent to a 200 V/m horizontally polarised EME is calculated.

2. Understanding the Skin Currents of an Aircraft at HF using Eigencurrents

In this section, the text is partly based upon a conference paper by the author. [12]

The Direct Current Injection (DCI) method was originally proposed for frequencies 10 kHz-5 MHz [13] and applied to an aircraft above a metallic ground plane. The purpose was to enable accurate measurement of the very low coupling levels seen on cable bundles at this frequency: Actual full field testing would then still use BCI. Bolsover et al. [7] have reported the use of a conformal earth return rig around the fuselage to achieve an improved travelling wave, and suitable performance up to 100 MHz was achieved. In the latter case, however, only a simplified range of current modalities could be excited, which excluded the differential mode across-wing currents and any asymmetrical circumferential currents. The authors used a variety of measurements to compare with the LLSC method including both skin and loom currents. The authors' comments were inspiring on the subject of calibration: "The difficulty encountered in deciding on a particular surface current position effectively ruled out surface current as a calibration tool." This brings us to a purpose of the present section: to methodically combine the numerous surface current locations into a few easily recognisable current modalities for effective calibration and control of the DCI method, or alternatives such as TEM cells.

In the HF range, wavelengths range from 300 m to 10 m, and are therefore large compared to a fighter/trainer aircraft, such as the Aermacchi MB326H (Macchi), which has length and wingspan of approximately 9m. Vector current densities should therefore change relatively slowly with location on the fuselage. In spite of the myriad of possible current modes, the small electrical size of the aircraft suggests to intuition that a modest number of modes might be used to describe, and hence calibrate the aircraft skin currents. One way of computing the modes is by the use of eigenvector analysis.

2.1 Description of Eigencurrents

The eigencurrent work is based upon the Method of Moments, originally developed by R.F.Harrington for one dimensional wire elements, but since extended to include a variety of basis functions to describe two and three dimensional current flows. In this work, the

Rao-Wilton-Glisson [14] triangular basis functions were used.[4] These are well adapted to describe current flows on conductive surfaces of arbitrary shapes. As is well known, the moment method has at its heart, the matrix equation:

$$\overline{V} = \overline{\overline{Z}} \cdot \overline{I} \; ,$$

where $\overline{I}$ is the vector of complex current amplitudes of the sub-sectional basis functions, $\overline{V}$ is the excitation vector and $\overline{\overline{Z}}$ is the impedance matrix.

Let the impedance matrix, $\overline{\overline{Z}}$ be of dimension N x N. Eigenanalysis of the impedance matrix then produces N eigenvector-eigenvalue pairs that satisfy the equation:

$$\overline{\overline{Z}} \cdot \overline{I}_i = z_i \overline{I}_i \; ,$$

where $\overline{I}_i$ is the ith eigenvector, and z_i is the ith eigenvalue. The eigencurrents are the dot products of the eigenvectors with the sub-sectional basis functions[5] , $\overline{j}(\vec{r})$:

$$\overline{J}_i(\vec{r}) = \overline{I}_i \cdot \overline{j}(\vec{r}) \; ,$$

and give surface current densities on the Macchi skin corresponding to the eigencurrent mode.

The eigencurrents are constituted of two main types of current modes: Electric dipole modes, which flow parallel to the wings, tailplane and the fuselage; and circulating, solenoidal currents which flow around the fuselage and on the skin surfaces generally. The electric dipole currents are associated with charge concentrations since they involve divergent (that is, Div **J**≠0) current flows. I will henceforth refer to them as capacitive modes. The circulating currents, being solenoidal, are by definition divergence-free, and hence have no charge accumulations. I will henceforth refer to them as inductive modes, as the energy is stored in magnetic fields. They might also be thought of as being similar to eddy currents.

When the impedance matrix is calculated at a sub-resonant frequency, such as 2 MHz for the Macchi, capacitive modes will have high impedance and inductive modes will have low impedance. Thus, the eigenvalue-eigenvector pairs may be sorted according to the eigenvalue magnitude, $|z_i|$. This is shown in Figure 1. It is found that the inductive, solenoidal eigencurrents have the lowest impedance, with the capacitive, electric-dipole, eigencurrents having the highest. Furthermore, the current distributions with high spatial frequency occur at the extreme ends of the impedance scale: Small loop-area inductive currents have very low impedance, and multi-charge[6] dipole current distributions have very high impedance. The region of most interest occurs in the middle of the impedance range, where transition takes place from large current loops with relatively high inductive impedance, to simple half-wave dipole distributions with relatively low capacitive impedance. These are the eigencurrents

---

4 The commercial code FEKO was used for the modelling in this work: Intermediate results such as matrices were exported and processed with various Matlab utilities, and the results were in some cases read back into FEKO for representation.

5 $\overline{j}(\vec{r})$ is a vector of N subsectional basis functions, each of which is defined over the 3 spatial dimensions. R-W-G basis functions are defined over pairs of adjacent triangles which share an internal edge. The current is thus distributed over the surface rather than being confined to wires as in NEC for example.

6 These multi-charge dipole distributions are intuitively equivalent to electric dipoles of 1 wavelength or greater, though more complex because of the two-dimensional nature of the aircraft skin.

most strongly excited by plane waves at HF. They occur close to the steep section of the curve in Figure 1.
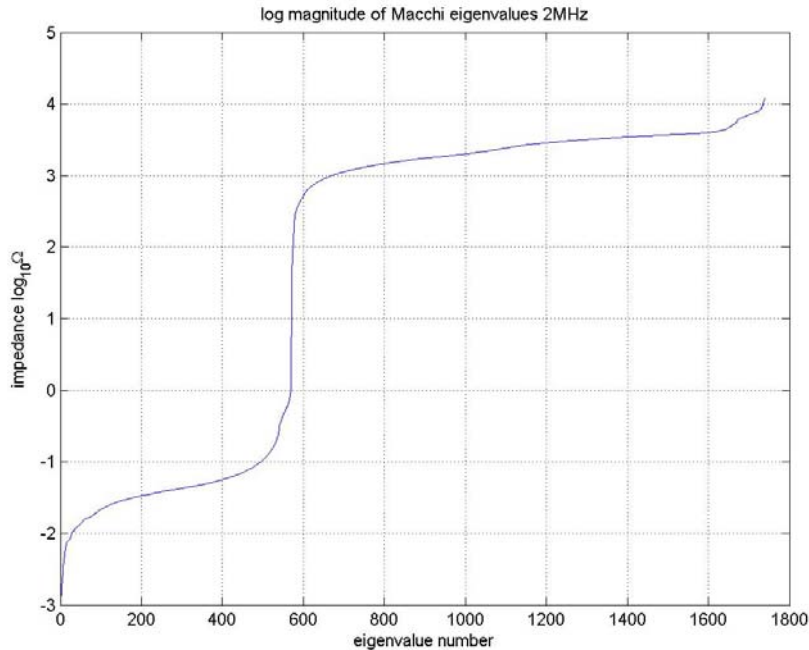

Figure 1   The Macchi eigenvalues sorted according to the log of their magnitude: The steep area marks the transition from inductive to capacitive eigencurrent modes.

In the data shown in Figure 1, a specific model is described. The Macchi was modelled in free space using 1739 triangular current basis functions. **The numbers derived from this sorting operation from 1, the lowest impedance eigencurrent, to 1739, the highest impedance eigencurrent, will be used throughout this report to refer to the Macchi eigencurrents.** The transition from inductive to capacitive eigencurrents occurred between eigencurrent numbers 570 and 571 in this case. Of course the numbering is arbitrary and a function of the particular model considered. However the methodology is general, in that fundamental capacitive modes for the wings, fuselage and tailplane could readily be identified – and these are the eigencurrents that are proposed to be used to calibrate the DCI method. The numbering scheme used seems unsatisfactory to the author, however it is not clear how a generic naming scheme could be designed for the eigencurrents on the aircraft. Aircraft structure is very complex compared to the canonical structures, such as rectangular cavities and spherical reflectors, for which rigorous resonance naming schemes have been used in the past.

2.2 Capacitive Macchi Eigencurrents (#571-#578)

The capacitive eigencurrents are numbered from 571 to 1739 in this model, however only the more simple and lower impedance eigencurrents were found to be significantly excited at 1-30 MHz. Thus in this section only numbers 571 through 578 are described.

The lowest impedance *capacitive* eigencurrent is number 571. It has current flowing parallel to the fuselage axis, between charge concentrations at the tail, and the nose and wingtips, as shown in Figure 2. A close-up of the current along the fuselage is shown in Figure 3. One would expect that such an eigencurrent would be strongly excited by an incident electric field parallel to the fuselage axis.
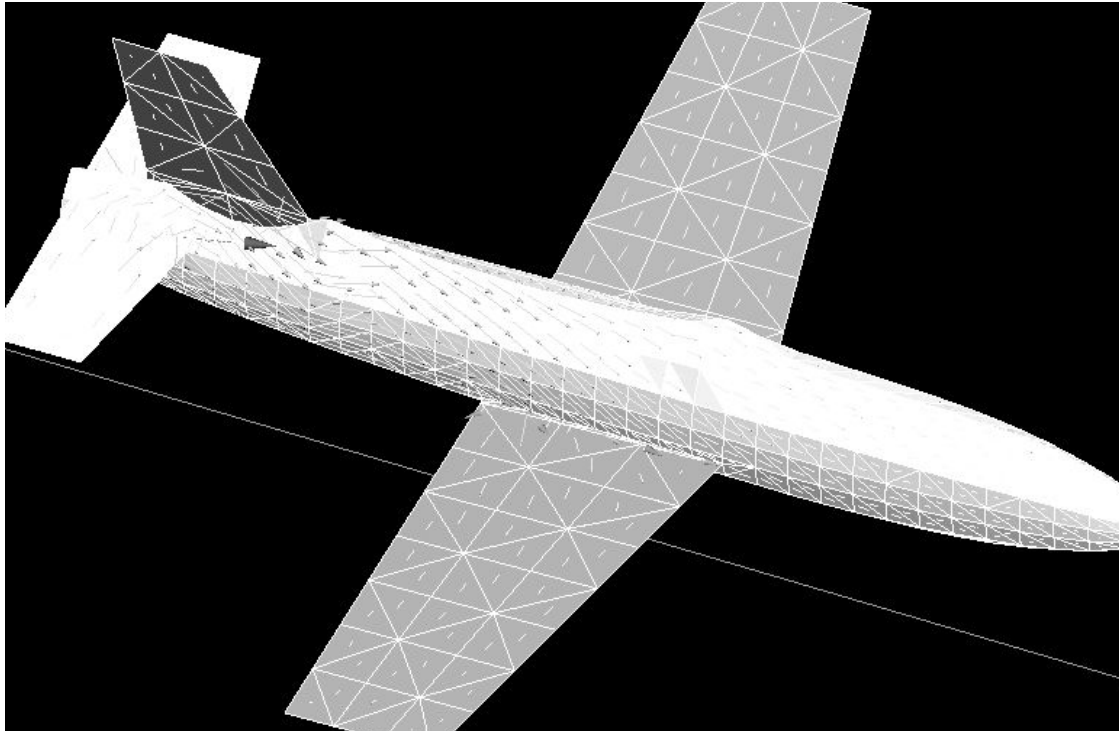
Figure 2 Macchi eigencurrent #571. Current flows mainly along the fuselage.

It is important to note that the tail plane and fin have one polarisation, while the nose and wingtips have the other polarisation at the point in the cycle when charge stops flowing.
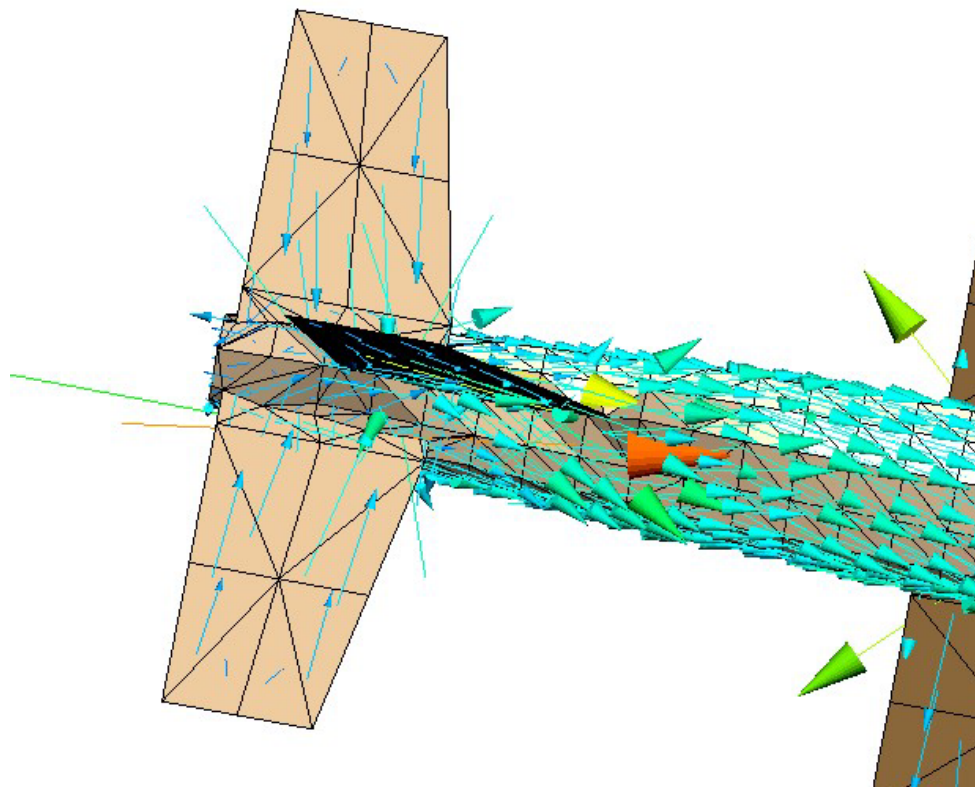

Figure 3   A close-up of the current flow for #571 which can be seen to move charge from the tail to the wings and nose

Another electric dipole mode is the across-wings current, which is represented by two mirror-image eigencurrents; essentially[7] one for each wing. This mode is expected to be excited by an incident electric field parallel to the wings. Eigencurrent #572 is shown in Figure 4. With symmetric excitation, the two wing capacitive eigencurrents (#572, #573) tend to occur in equal quantities, though with either the same or inverse phases, depending on whether they are driven in common or differential mode. More detail is given in section 3.

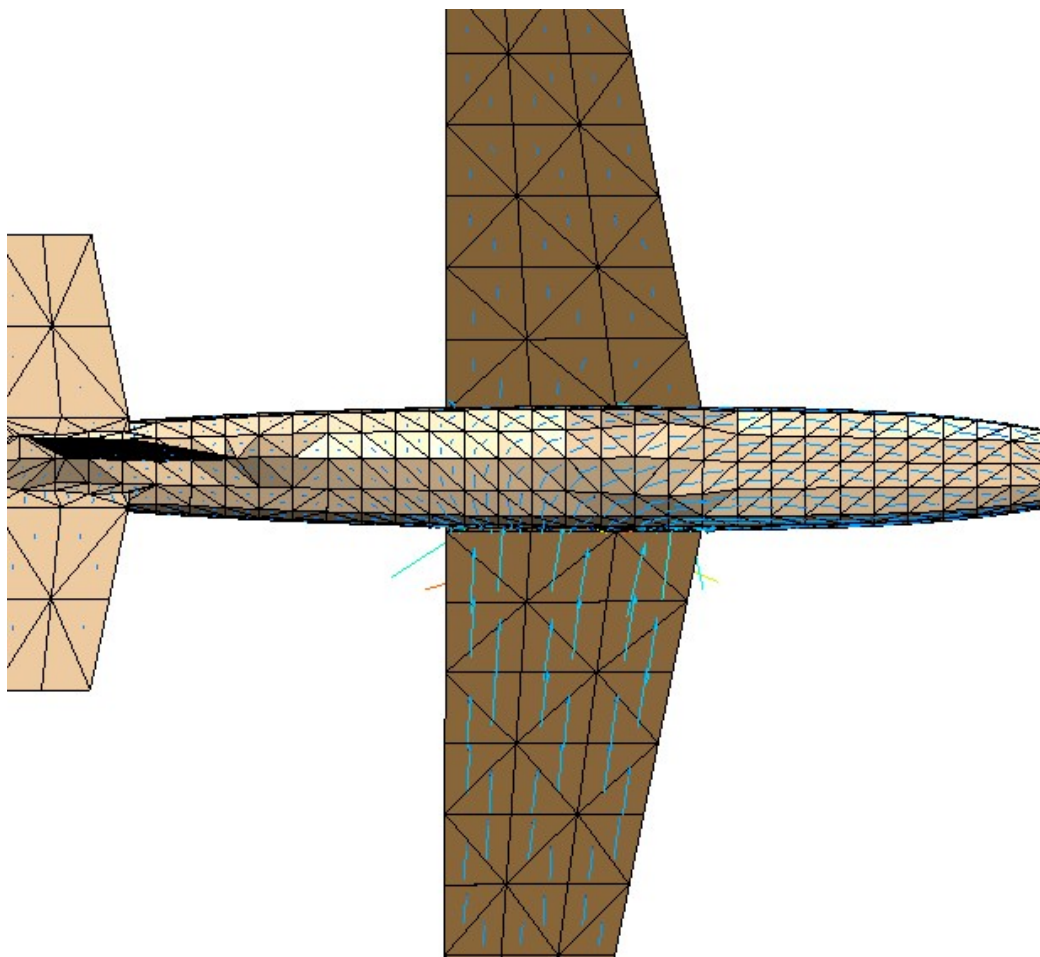*Figure 4   Macchi eigencurrent #572, the starboard wing fundamental capacitive mode. A mirror image eigencurrent, #573 occurs for the port wing.*

---

7 I say 'essentially' because the currents are present on both wings but predominate on one wing.
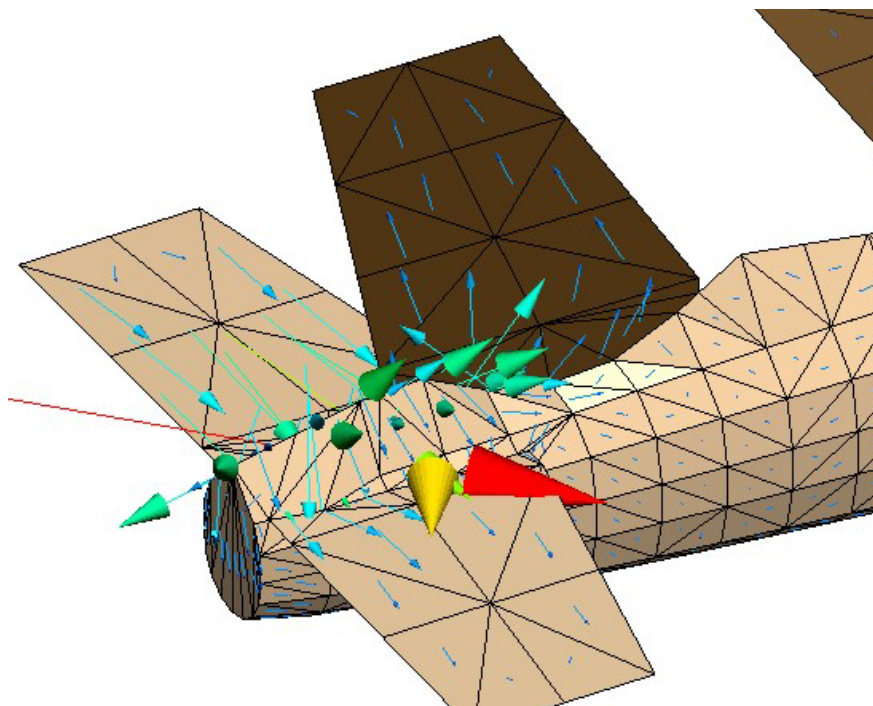
Figure 5   Eigencurrent #575 : A capacitive mode involving current flow across the port tailplane. A mirror image mode exists with most current flowing on the starboard tailplane: #574.
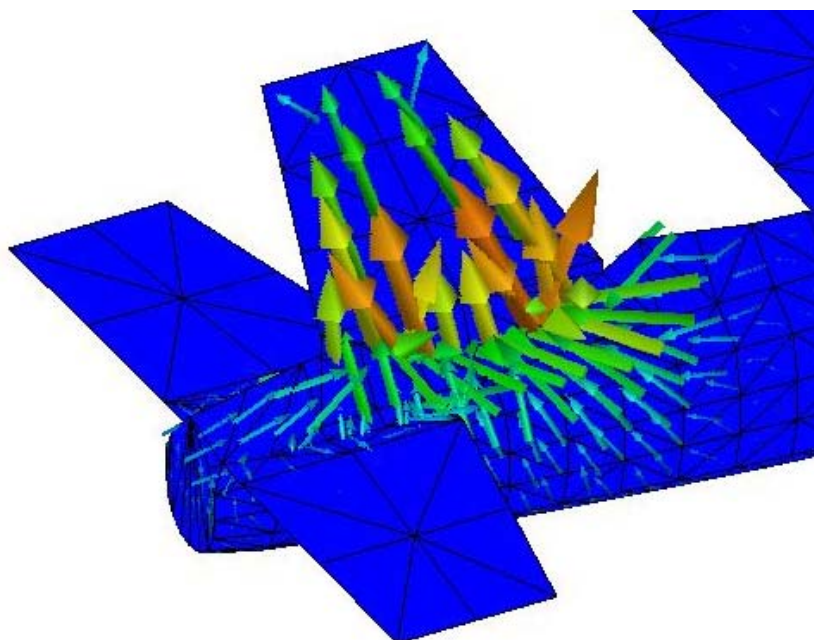
Figure 6   Eigencurrent #576. This is mostly a vertical current on the tail fin. It would be excited by vertically polarised electric fields.

The equivalent modes for the tailplane are #574, #575. Eigencurrent #575 is illustrated in Figure 5. It is easy to imagine that if this mode were combined with an equal and opposite phased, mirror-image mode, that the currents in the fin would cancel, and a strong current would flow from port to starboard tailplane tips.

The mode #576 is shown in Figure 6. This mode has current flowing from the tail fin into the rest of the aircraft. It would be expected to be excited by vertically polarised electric fields.

In some modelling, higher order capacitive current modes were seen. Mode #577, a second order fuselage mode is shown in Figure 7. The third order fuselage mode is shown in Figure 8
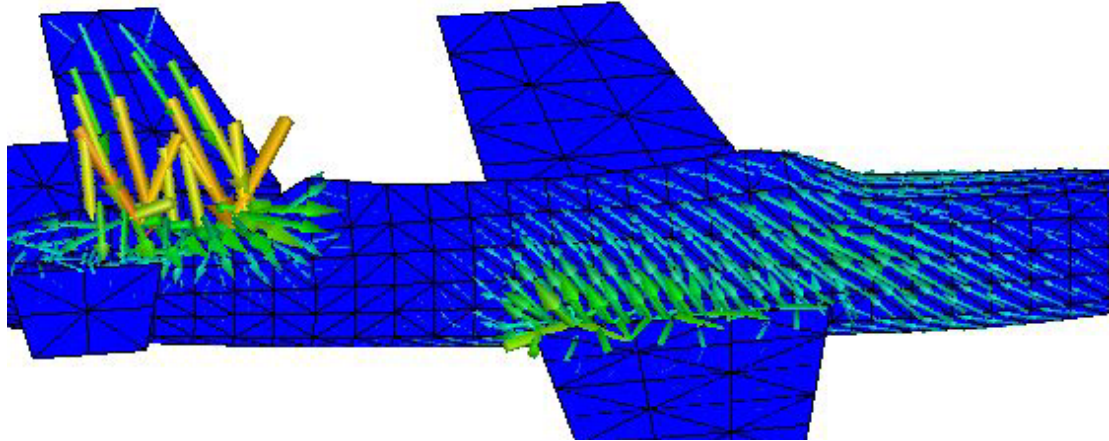

Figure 7   Eigencurrent #577. This second-order capacitive mode has three charge concentrations along the fuselage: The usual two terminal charges plus an intermediate charge region between wings and tail.
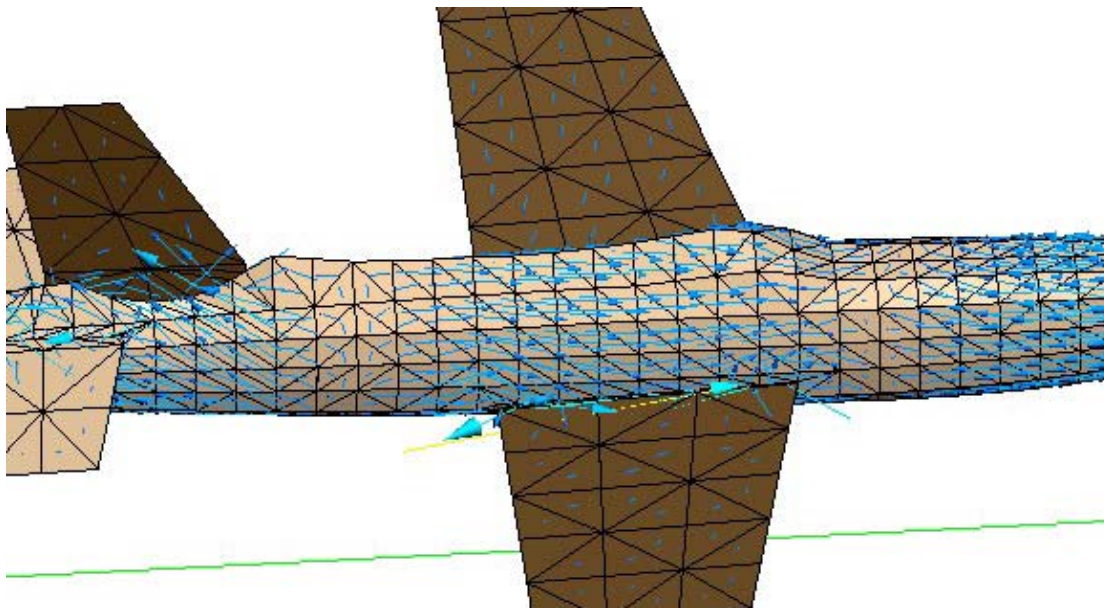

Figure 8   Eigencurrent #578, a third order fuselage mode. Two intermediate charge concentrations are seen in addition to the terminal charges.

Table 1   Categorisation of capacitive eigencurrents on the Macchi according to direction of exciting electric field and location on the aircraft.

Location ➡️ E field axis ⬇️ for excitation ▼	Wings	Fuselage		Tailplane	Fin
		Fundamental	Higher mode		
Pitch Axis	#572(s) #573(p)			#574(s), #575(p)	
Roll Axis		#571	#577(2) #578(3)		
Yaw Axis					#576

2.3 Inductive Macchi Eigencurrents (#531-#541,#544 , #569, #570)

As mentioned earlier, inductive current modes result from circulation of current rather than convergence of current to a charge concentration. In vector calculus, such vector fields are known as solenoidal. In the case of the inductive current modes, this is an apt description as they often resemble the single turn solenoid, as described below.

Inductive current modes can occur anywhere that a return path is provided: In the plane of a conducting surface as in number 569 or where a double skin is located, such as around the fuselage circumference and around the wing. These modes would be expected to be dominant at the lowest frequencies due to their impedance being proportional to frequency. Furthermore, it would be expected that their level would be relatively constant because the Electromotive Force (EMF) is also proportional to frequency:
The EMF is given by

$$V_i \approx A_i \, j\omega B \, ,$$

and the impedance by

$$z_i \approx j\omega L_i \, ,$$

and hence

$$\therefore I_i \approx \frac{A_i B}{L_i} \, , \text{ which is independent of frequency.}$$

For some simple inductive modes, such as circulation around the fuselage, the current may be compared to a long, single-turn solenoid of length l_i, and area A_i. Then:

$$L_i \approx \mu_0 \frac{A_i}{l_i} \, ,$$

which may be substituted into the equation for current to give:

$$\frac{I_i}{l_i} \approx \frac{B}{\mu_0} \approx H$$

Thus the current density $\dfrac{I_i}{l_i}$ (A/m) resulting from ideal incident field polarisation is not only constant, but equal to the magnetic field intensity of the incident field, H[8]. In the magnetostatic case, sufficient current density is generated to exclude the magnetic field from penetrating within the solenoid. Of course, the above magnetostatic analysis is only accurate at low frequencies.

This frequency independence of the inductive modes contrasts with the capacitive modes, which are initially weakly excited, but which become strongly excited at half-wave resonance[9], due to the minimisation of their reactance.
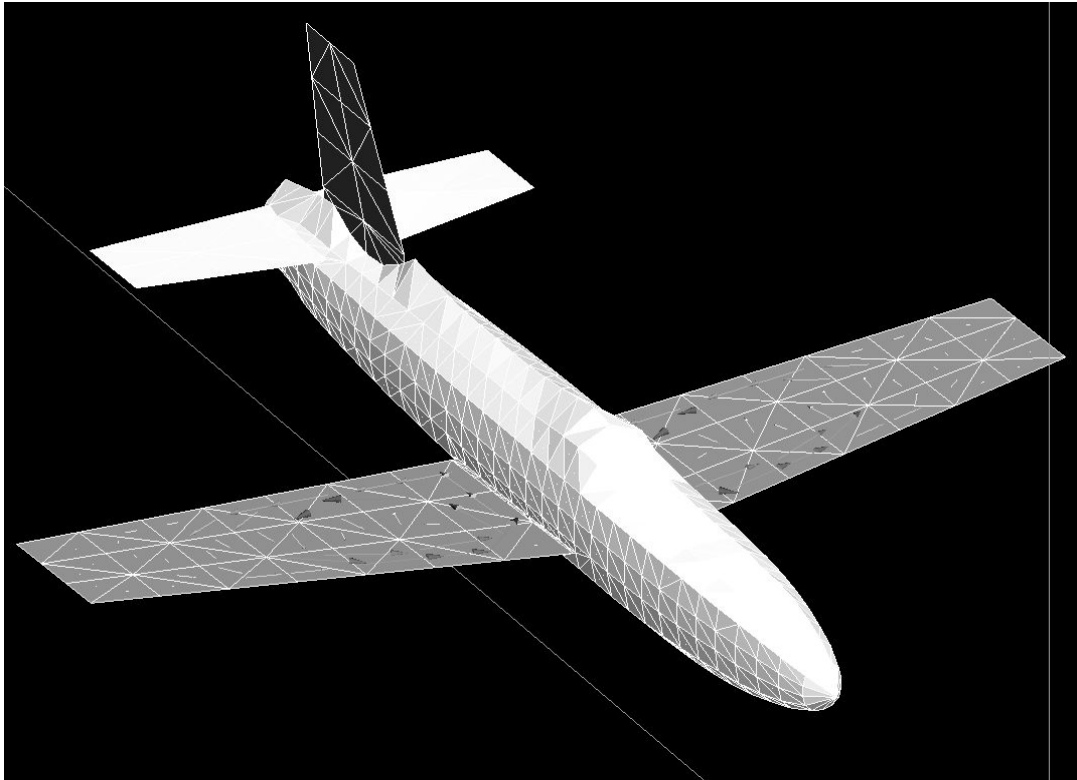

Figure 9   Inductive eigencurrent number 569. Circulating currents are primarily in the plane of the wings with the same rotational direction on both wings. Eigencurrent 570 is similar but with opposite sense of circulation on each wing.

The highest impedance inductive eigencurrent is #570, in which currents circulate in the plane of the wings with opposite direction on each wing. In eigencurrent #569, shown in Figure 9, a similar type of circulation occurs but with the same circulation direction on each wing.

---

8 These currents may be compared to the optical current densities that occur on electrically large conductive sheets subject to a normally incident plane wave, where current density approaches *2H A/m*. The increased current density is the result of complete reflection of the incident wave in the optical case, so that adjacent magnetic field intensity is doubled, whereas an infinitely long solenoid has a vanishingly small external (reflected) field.

9 Here I am speaking of the fundamental modes - higher order modes have peak occurrence at higher order resonances

Now, we consider a group of eigencurrents which represent currents circulating on the fuselage. Only sufficient are mentioned to describe the dominant fuselage circulating currents in subsequent sections.

The eigencurrent #531 is shown in Figure 10. It is a complex pattern of circulations, strongest in the plane of the fin, but also on the fuselage. Generally speaking, for inductive modes, as impedance and eigencurrent number get larger the circulation pattern becomes simpler with larger effective solenoid area, and less field cancellation by adjacent counter-circulations.
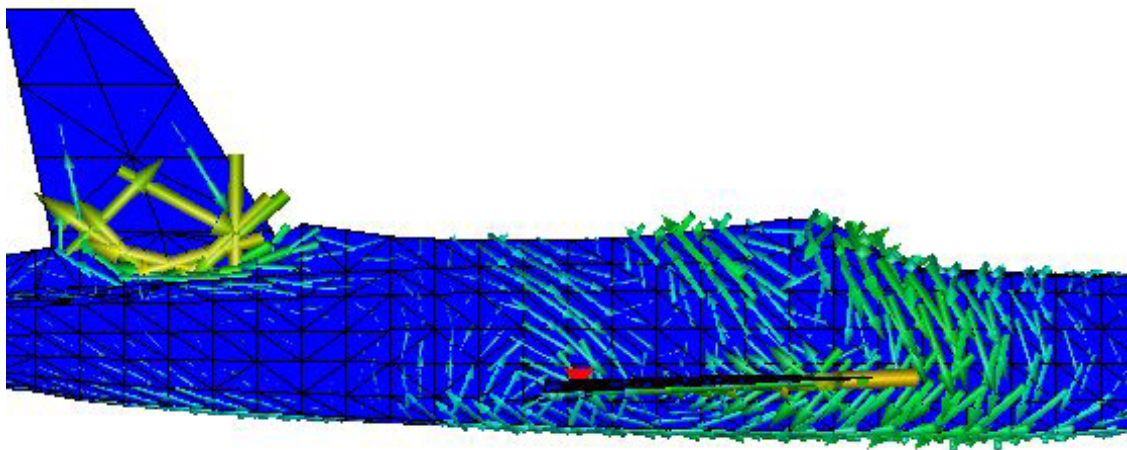
Figure 10   Eigencurrent #531. This is a complex pattern of interlocking circulations that defies easy conception. There is a strong circulation in the fin as well as on the mid fuselage.

The eigencurrent #532 is shown in Figure 11 and Figure 12. Although it is somewhat complicated in the area of the wing root, elsewhere it may be seen to be a circulation around the fuselage axis, which should be excited by a magnetic field parallel to the fuselage axis. In this respect it is similar to a long solenoid around the roll axis of the aircraft. It would thus be expected to respond to magnetic fields aligned with the roll axis, that is parallel to the fuselage.

Figure 11   Mode #532. This inductive mode, though complicated in the wing root region, is essentially a circulation around the circumference of the fuselage. The underside is shown here.
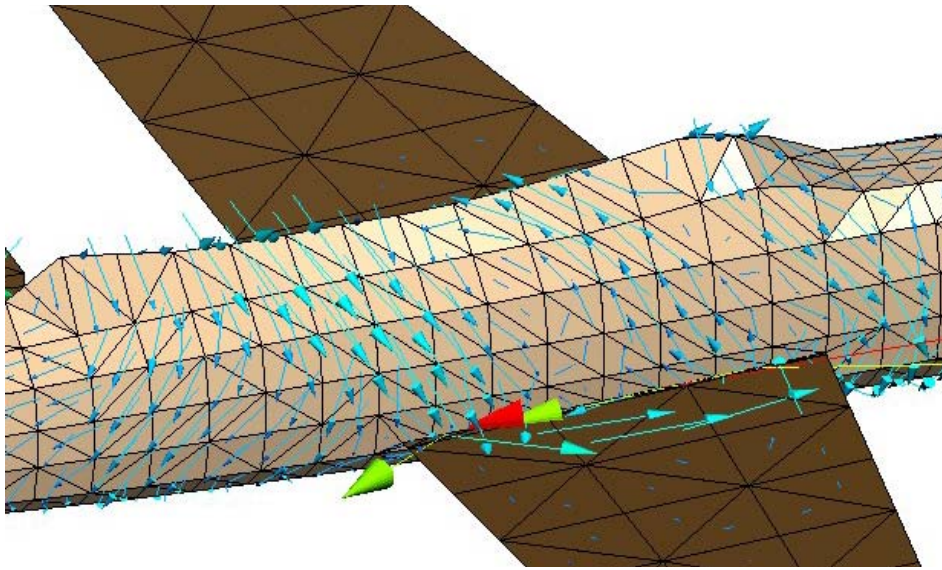
Figure 12 Mode #532. A perspective view. from the aft starboard direction.

In mode #533, shown in Figure 13, currents circulate around the fuselage in a largely horizontal plane. As it resembles a horizontal loop around the fuselage plan, it should be excited by a magnetic field aligned with the vertical or yaw axis of the aircraft.
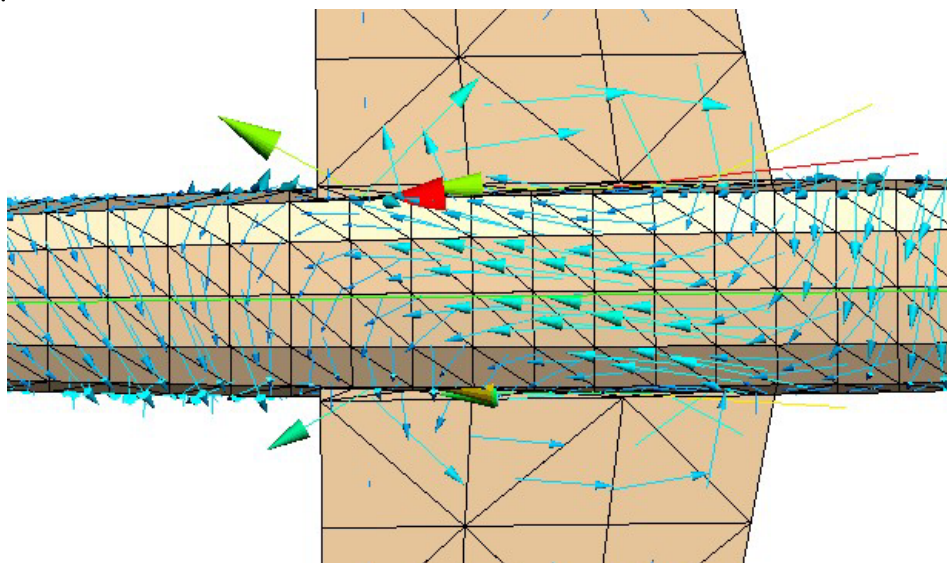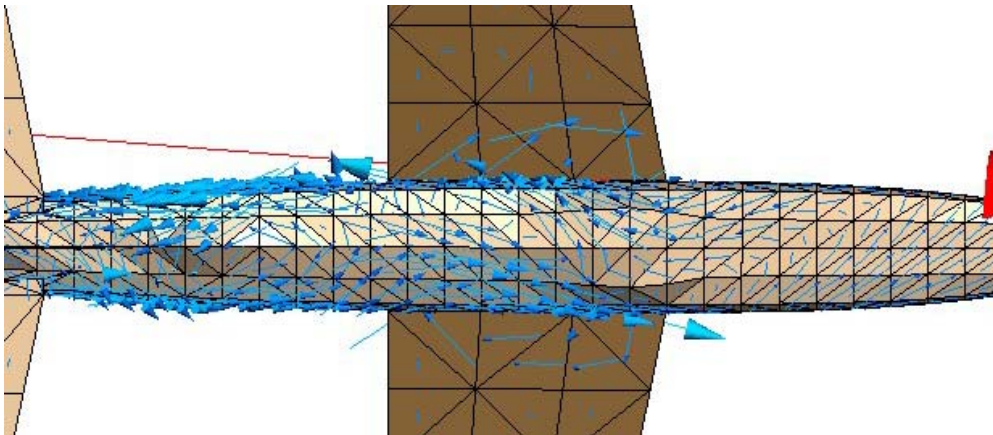

Figure 13   Mode #533. Currents circulate around the plan of the fuselage. This view is from beneath.

In mode #534, shown in Figure 14, currents circulate around the axis of the fuselage, but in about 4 bands which are reversed in direction relative to the adjacent bands. It is not clear how such a mode would be excited, as a plane wave with magnetic field aligned with the roll axis would not have the suitable changes of phase along the fuselage. However if the magnetic field was aligned between the roll axis and the pitch axis, it could still have a significant field component in the roll axis while having a phase variation along the fuselage length.

It is worth remembering that there is no necessity for an eigencurrent to be excited by a single plane wave. The eigencurrent definition merely requires that, in order to excite one eigencurrent alone, the incident electric field at the aircraft skin should be everywhere parallel to the eigencurrent. Furthermore, this only applies at the frequency for which the eigencurrent is an eigenvector of the moment matrix. There will be more about this subject, later.
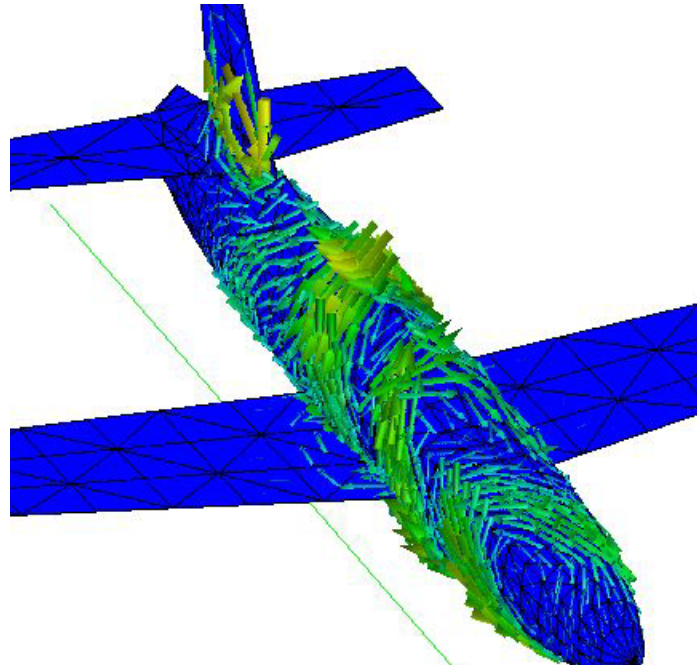
Figure 14   Mode #534. This mode has counter-rotating bands of current circulating about the fuselage axis.
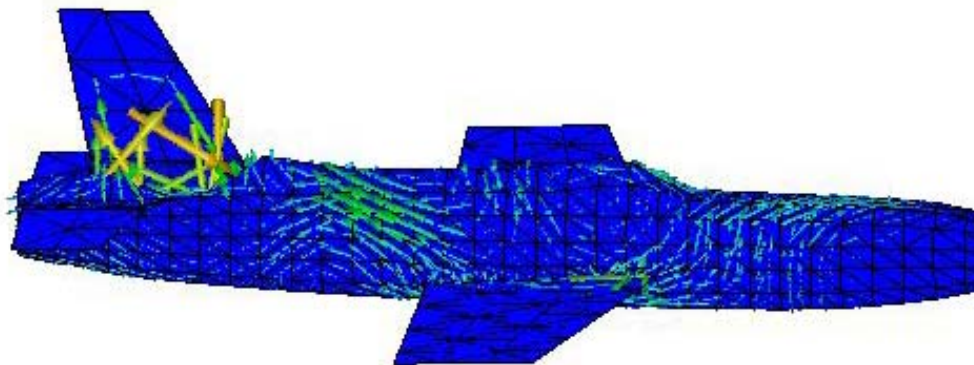
Figure 15   Mode #535. This mode has circulation mainly in the plane of the fin, but there is also circulation around the fuselage in the horizontal plane.
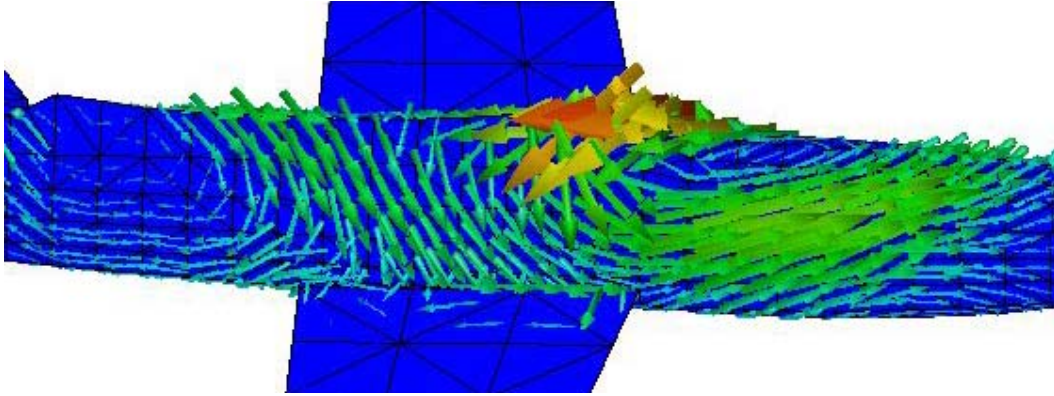
Figure 16   Mode #536. This is a circulation on the forward fuselage mainly in the horizontal plane. It should be excited by vertically polarised magnetic fields.

Modes #535 and #536 are shown in Figure 15 and Figure 16. Mode #535 has significant circulation in the plane of the fin and should be excited by a magnetic field aligned with the pitch axis. Mode #536 exhibits circulation in a horizontal plane on the forward part of the fuselage. It should be excited by fields with vertical magnetic component.

Mode #537 is shown in Figure 17. As well as having a circulation in the plane of the fin, this mode has a circulation in a band around the fuselage at the leading edge of the wing. It should be excited by magnetic fields having components in both the roll and pitch axis.
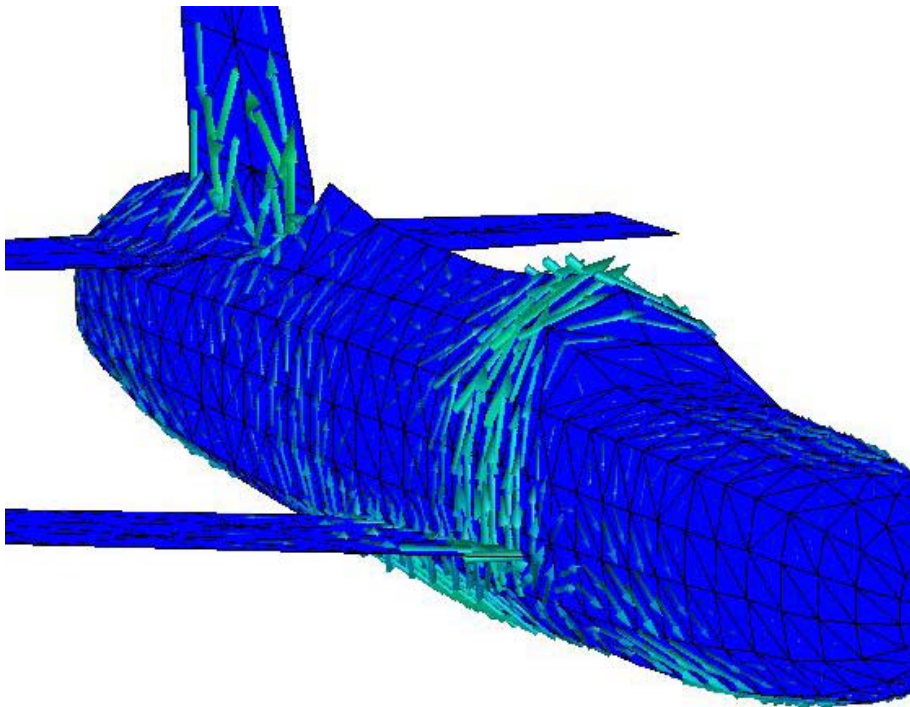
Figure 17   Mode #537. This mode has some circulation on the fin, but also a circulation around the fuselage axis mainly in the area of the wing leading edge.

16

Mode #538 is a very complex and fascinating current distribution. Two views are shown. The current appears to be two helical streams, flowing in opposite directions. A similar effect could result if a circular loop of metal strip were taken, elongated to an eccentric ellipse and then twisted about the long axis of the ellipse. It is not clear how a plane wave field would excite this mode, however the twisted loop planes could present to any of the aircraft axes.
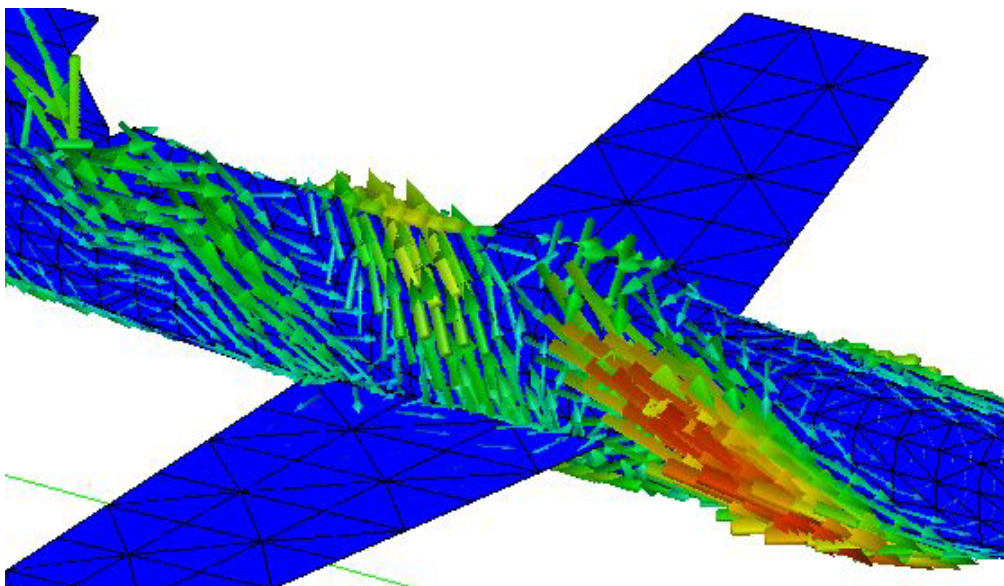
Figure 18 A starboard view of mode #538. The current appears to be two opposed helical streams.
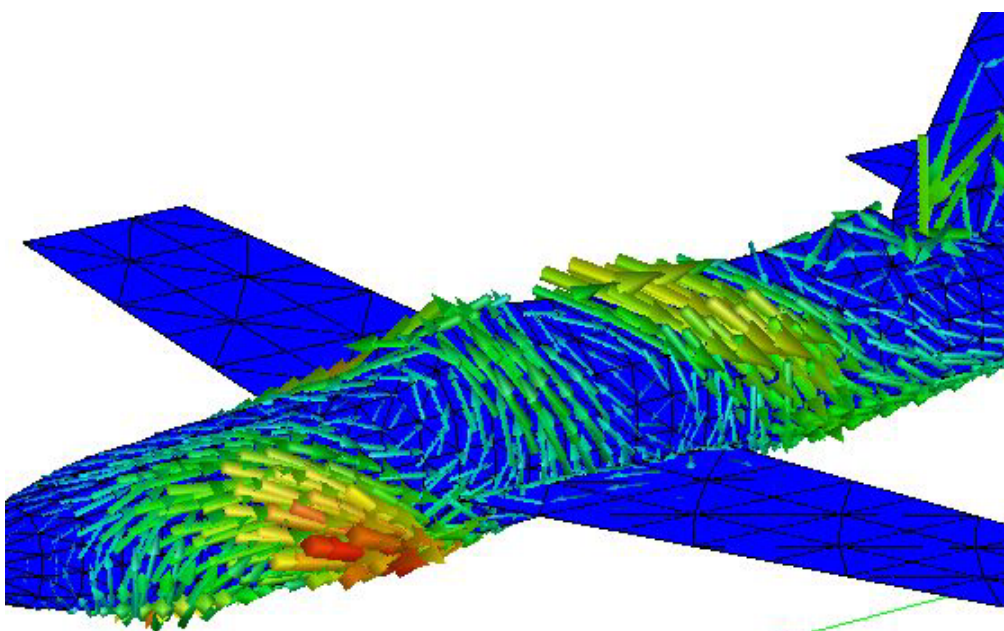
Figure 19 A port view of mode #538. See the starboard view also.

Modes #539 and #541 are shown in Figure 20 and Figure 22. These modes are similar in that they are circulating in a vertical plane about an axis parallel to the pitch axis. The main difference lies in the location where the current is concentrated: further aft on #539 and further forward on #541. It would be expected to see these modes excited to similar degrees by plane wave fields with magnetic fields aligned with the pitch axis.
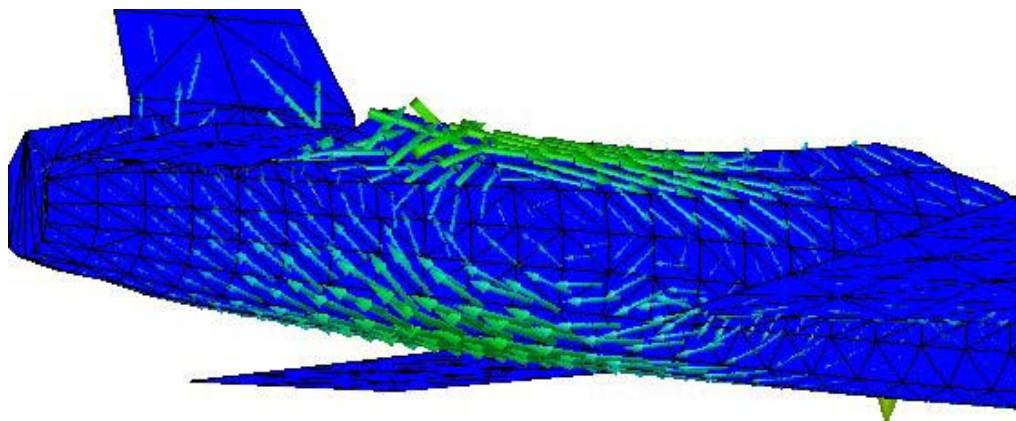
Figure 20   Mode #539. This inductive mode runs froward on the upper fuselage and aft on the lower fuselage. It should be excited by magnetic fields polarised parallel to the pitch axis of the aircraft.

Mode #540 is shown in Figure 21. The current circulates on the forward part of the fuselage about an axis at about 45 degrees to the aircraft axis. It could be excited by plane wave fields with horizontal *magnetic* polarisation incident either from ahead or abeam.
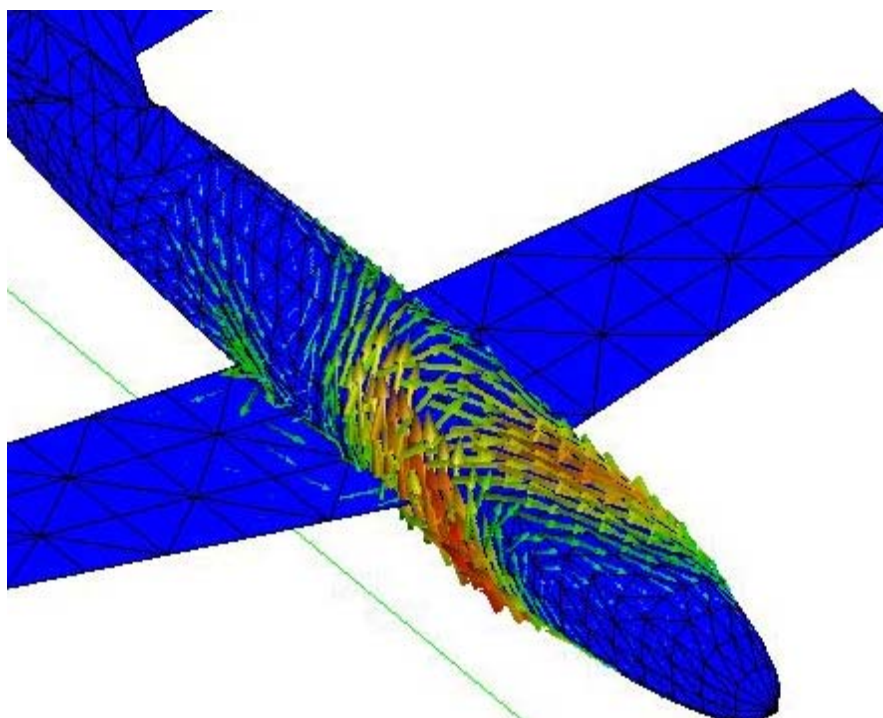
Figure 21   Mode #540. Current circulates about an axis which is intermediate between the fuselage roll axis and the pitch axis. It could be excited by magnetic fields parallel to either the pitch or roll axis.

18
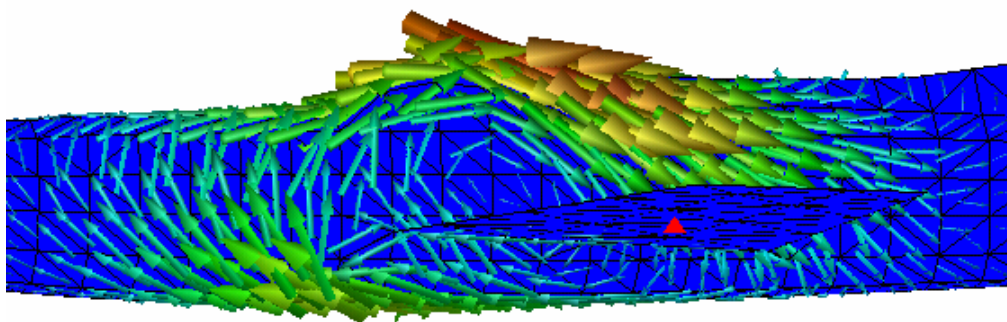
Figure 22 Mode #541. This circulating mode rotates about the aircraft's pitch axis and should be excited by magnetic fields parallel to the pitch axis.
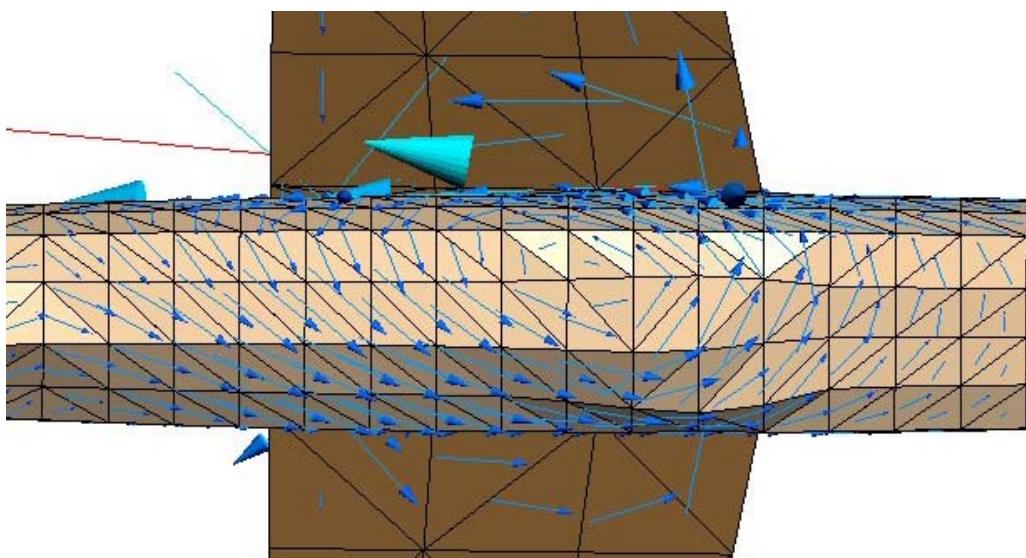
Figure 23   Mode #544. This is a circulation in the horizontal plane on the fuselage. Like #533, it should be excited by vertically polarised magnetic fields.

Mode #544 is a circulation of current on the central portion of the fuselage in the horizontal plane. It should be excited by horizontally incident electric fields with vertical polarisation of the magnetic field.

Table 2   Approximate categorisation of inductive eigencurrents according to the axis of circulation (and hence stimulating magnetic field direction) and principle location on aircraft.

location ⟶ H field axis ↓ for excitation	Fin	Fuselage front	Fuselage central	Fuselage rear	Wings
Pitch Axis	#535 #531 #534 #537 #538	#541#538	#541 #539	#539 #540	
Roll Axis		#532 #531#538	#532 #537	#532 #540	
Yaw Axis		#536 #533#538	#533 #544	#533	#569 #570

A categorisation of the inductive eigencurrents by their number is given in Table 2. This may be used in the following way: For a given incident plane wave field, one first determines whether the magnetic field is parallel to the pitch, roll or yaw axis of the aircraft. Then by reading across the table one may read the modes likely to be excited and where they occur. For example, an (electric field) vertically polarised wave incident from the aircraft front has a magnetic field parallel to the pitch axis. Then we see that any of #539, #540 ,#538 and #541 may occur on the fuselage and any of #535, #531, #534, #537 #538 could contribute currents on the fin. The table may be used in the reverse fashion. If a test excitation causes a particular set of circulating modes, we may see which magnetic field directions it is contributing and where the circulations occur on the aircraft.

2.4 Resolution of computed total skin currents into the eigencurrents

An important property of eigenvectors for this purpose is their orthonormality: That is to say, they are all of unity magnitude and orthogonal to each other, giving a zero dot-product for different eigenvectors:

$$\bar{I}_i \cdot \bar{I}_j = 0; i \neq j$$
$$\bar{I}_i \cdot \bar{I}_j = 1; i = j$$

The computed current vectors could thus be resolved into the eigenvectors using:

$$\alpha_i(f) = \bar{I}(f)_{planewave}^T \cdot \bar{I}_i \,,$$

where α_i (f) is the (complex) amplitude to which the particular eigencurrent is excited by the plane wave incident field and $\bar{I}(f)_{planewave}^T$ is the computed complete current vector for the plane wave as a function of frequency.

Such a resolution into eigencurrents would be of little value if a very large number of eigencurrents required significant amplitudes to describe the total current. The initial hypothesis behind this work was that only a small number of eigencurrents would be required due to the large wavelengths involved relative to aircraft size. Now is the time to test that hypothesis.

Recall that previously the *eigenvalue amplitudes or impedances* were sorted to obtain the numbering of the eigencurrents and to classify them into inductive or capacitive. On this occasion, the *excitation amplitudes*, $\alpha_i(f)$, may be sorted by magnitude. Now, the relative eigencurrent excitation amplitudes will change with frequency. Thus the squared absolute amplitudes were summed over frequency and then sorted to average this effect.

The following example is used; plane wave excitation is incident from the front of the aircraft. In this case the electric field is parallel to the wing axis. The resulting main excitation amplitudes are shown in Figure 24. The relative cumulative amount of (summed, squared) amplitudes as the sorted eigencurrents are combined is referred to as the cumulative energy and may be expressed with the following equation:

$$y(m) = \sum_{i=1}^{m} \sum_{f=1}^{N_f} \left| \alpha_i(f) \right|^2 / \sum_{i=1}^{N} \sum_{f=1}^{N_f} \left| \alpha_i(f) \right|^2$$
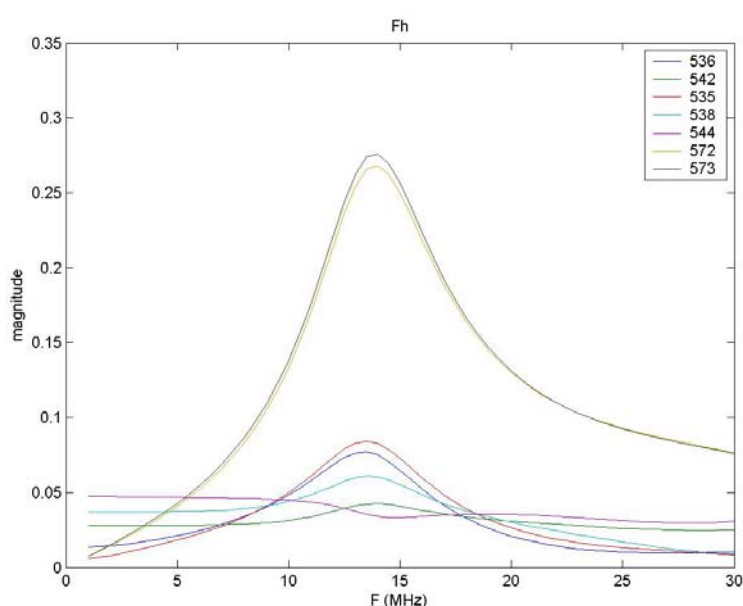
Figure 24   Largest seven eigencurrent excitation amplitudes for the Macchi in free space with horizontal polarised plane waves incident from the front, as a function of frequency.

The variation of cumulative energy with number of additional eigencurrents is shown in Figure 25. The first two eigencurrents each contribute 32% of the total of all eigencurrents. Together they account for 64% of all energy. The largest seven together contribute 75% of all the energy. The largest 100 contribute 96%: In other words the eigencurrents from the eighth largest to the hundredth largest contribute only another 20%, or on average 0.2% each. There is little additional benefit in considering eigencurrents smaller than the seven largest, which is consistent with the hypothesis that a small number of eigencurrents would be adequate to describe the current distribution. In all subsequent work, only the largest seven eigencurrents of the total 1739 are plotted.
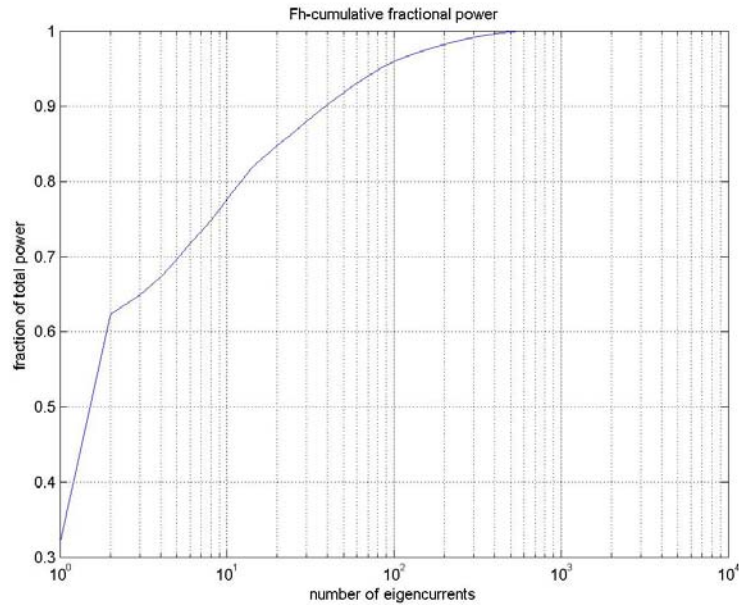
Figure 25 The cumulative 'energy' present in the sorted eigencurrents.

2.5 Limitations of the Eigenvectors

This work is based on the idea of the eigenvectors of the impedance matrix, but they are eigenvectors of the impedance matrix only at the frequency for which the matrix was calculated: In this case that is 2 MHz. If different eigencurrents were computed for each frequency it would be an additional challenge to track the identity of the eigencurrents from frequency to frequency; that is to form a one-one mapping between eigencurrent indices computed at adjacent frequencies. It is also conceivable that if an algorithm could be developed to perform the mapping that, as eigencurrents changed over frequency, they could morph into multiple eigencurrents. The problem could be akin to looking for the source of the Nile.

Of course, even though this work has used the 2 MHz eigencurrents for the HF range, the eigenvectors retain their ortho-normality and are thus still capable of resolving the total currents into components. The cumulative energy study shows that the amplitudes so calculated using a small number of 2 MHz eigencurrents represent 75% of the total energy in the skin currents. Thus in this practical sense the approach is valid.

However, what are the implications of the use of 2 MHz eigencurrents at frequencies as high as 30 MHz? The main effect is that we can not assume the 2 MHz eigencurrents are actually independent of each other. In other words, it becomes possible for the oscillation of one eigencurrent to parasitically excite another eigencurrent at frequencies other than 2 MHz. At 2 MHz, the scattered voltage vector in the moment equation is parallel to the oscillating eigenvector :
If

$$\overline{V}_i = -\overline{\overline{Z}}\,\overline{I}_i$$

then
$$\overline{V}_i = -z_i \overline{I}_i \,,$$
by definition of the eigenvector.

Now consider this scattered voltage vector as the incident voltage vector for the other eigencurrents:
$$\overline{V}_i = \overline{\overline{Z}} I$$
then
$$\overline{V}_i = \overline{\overline{Z}} \sum_1^N \alpha_j \overline{I}_j$$
$$\therefore \overline{V}_i = \sum_1^N \alpha_j \overline{\overline{Z}} \overline{I}_j$$
$$\therefore \overline{V}_i = \sum_1^N \alpha_j z_j \overline{I}_j$$

The coefficients α_j can be obtained by taking the dot product of both sides by the eigenvectors in turn:
$$\overline{V}_i \cdot \overline{I}_j = \sum_1^N \alpha_j z_j \overline{I}_j \cdot \overline{I}_j$$
thus, if i≠j
$$0 = \alpha_j z_j$$
And thus the parasitically excited amplitude of any other eigenvector is zero.

Thus we see that a true eigencurrent is unable to excite the oscillation of a different eigencurrent. A further convenient property of the eigenvectors, shown above but unused in this work, is that the moment equation doesn't need to be solved for different voltage vectors. If the eigenvectors and eigenvalues are known, then dot products can be directly taken with the voltage vectors to compute the amplitudes.

However, if the ortho-normal vectors are not eigenvectors, due perhaps to being used at a different frequency, then the scattered voltage in the moment equation is not parallel to the oscillating current vector. Thus it is possible for the fields so produced to couple to a different current vector. This phenomenon is seen in some cases in the following work. It is especially obvious where dominant capacitive 'eigencurrents' go into resonance and perturbations are visible in other 'eigencurrents'. In the remainder of this report, although it is not strictly correct to refer to the 2 MHz 'eigencurrents' as eigencurrents at all frequencies, the quotation marks are dropped and they are referred to interchangeably as eigencurrents or modes.

A further warning is necessary to those using or interpreting results based on eigencurrent analysis. Because several eigencurrents may have significant currents on a particular aircraft part, it is necessary to consider them together on occasions and to note relative phases and amplitudes. An example may be made with the #571, #572, #573 capacitive modes. All these have currents on the wings. #571 has a common mode current on both wings, and #572 and #573 have most current on the starboard and port wings respectively. A suitable amount of #571, and equal amounts of #572 and #573 can be combined with similar phases to produce zero current on the wings. In another example, #572 and #573 can be combined in equal amounts with opposite phases to cause a differential flow of current from wingtip to wingtip. If equal amounts of #572 and #573 are combined with the same phase, then a common mode of current flows simultaneously inward on both wings. These might produce very different amounts of coupling to internal cables if the cables link one wingtip to the other. The difference might be small, however, if cables link a wingtip with the fuselage.

The moment method model of the Macchi used in this work uses zero-thickness plates to represent the wings and tailplanes. This simplification can be expected to fail to model certain kinds of inductive modes, where currents flow in opposite directions on the upper and lower skins in actuality.

2.6 Summary

The work in this section has, to the author's best knowledge, described a novel way of understanding the currents on an aircraft's skin at HF frequencies. Discussion, understanding and publication of data gathered in experimental or numerical LLSC and DCI work has previously been hampered by the very large quantity of data gathered over frequency at numerous cable loom and skin current density sites, usually without phase measurement.

It is accepted that those knowledgeable in the art of EMC for aircraft have long been familiar with the concept of fuselage and wing resonance. However the present work provides a rigorous mathematical basis to these concepts, which may be applied without too much requirement for arbitrary judgement. It has also drawn attention to a group of circulating modes that greatly complicate the appearance of the skin currents, and which could easily dominate the current distribution in artificial circumstances.

It was shown in one example that only seven of 1739 eigencurrents automatically chosen from a numerical model represented over 75% of the total 'energy' of the skin current modes at HF frequencies. The magnitudes and phases of these modes then represent all the EMC engineer needs to know about the required currents on the aircraft skin when in free space, subjected to a plane wave. The engineer may then approach the problem of DCI, or other HF HIRF test methods, as controlling the available parameters to target the major eigencurrents. This could be through the simultaneous control of DCI injection phases and magnitudes. However in a simple test approach, only one parameter may be available, such as input power. The use of the eigencurrent approach will provide a rigorous basis to such tests, by enabling the control of the dominant capacitive modes to match the modelled worst-case plane-wave situations.

3. Free Space Skin Current Distributions

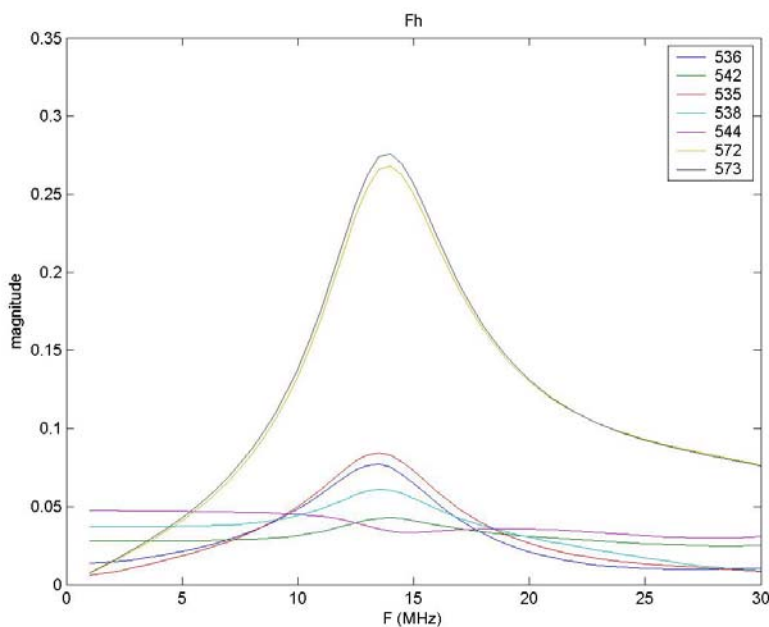## 3.1 Horizontal Polarisation

Figure 26   Eigencurrent amplitudes of the Macchi model when exposed to horizontal polarised waves from the front.

The largest seven Macchi eigencurrent amplitudes when exposed to horizontal polarised, plane waves from the front are shown in Figure 26. In order to understand the capacitive currents, we need to first consider the aircraft axis to which the incident electric field is parallel. In this case, the electric field is parallel to the pitch axis. Now, by consulting Table 1, we see that the two wing modes #572 and #573 could be excited, as could the two tailplane modes, #574, #575. We see from the figure that the two wing capacitive eigencurrents, #572, #573 are exactly equally excited, as would be expected from symmetry, and reach a resonant peak at 14 MHz. The tailplane modes are not noticeably excited, possibly due to shadowing from the wings. The remaining 5 most strong eigencurrents are inductive. To understand these we must consider the orientation of the incident magnetic field. In this case the magnetic field is vertical, and thus parallel to the yaw axis. We see from Table 2 that such a magnetic field can excite modes #533, #536, and #544 on the fuselage and #569 and #570 on the wings. Of these, #544 and #536 appear in the top seven modes. #544 has a nearly constant level, consistent with the theory of section 2.3. The next most prominent eigencurrent is #538, the complex helical pattern. This pattern was too complex to guess, from the current form, the magnetic field directions to which it would respond. Interestingly, there are two inductive eigencurrent modes, #535, #536 which appear to become resonant at the same frequency as the wing capacitive modes. It is not clear why this would be: It might be supposed that the resonant excitation of the wing modes would couple into some fuselage circulations. However, the eigencurrents, because of their mutual orthogonality should not couple together. It must be remembered however, that the eigencurrents are only eigenvectors of the impedance matrix at the low frequency of 2MHz. At higher frequencies the eigencurrents may change slightly, whereas in this work it is assumed they remain constant. Thus, there could exist coupling between eigencurrents.

Finally, the eigencurrent phases are plotted in Figure 27. Note that the two wing modes, are almost exactly π radians out of phase. Thus the current flows inwardly on one wing and outwardly on the other at a given time. This is consistent with the idea of the wings jointly functioning as a dipole. Note also that #535 and #536 become very close in phase to each other and to mode #572 at the wing resonance frequency and then diverge again.

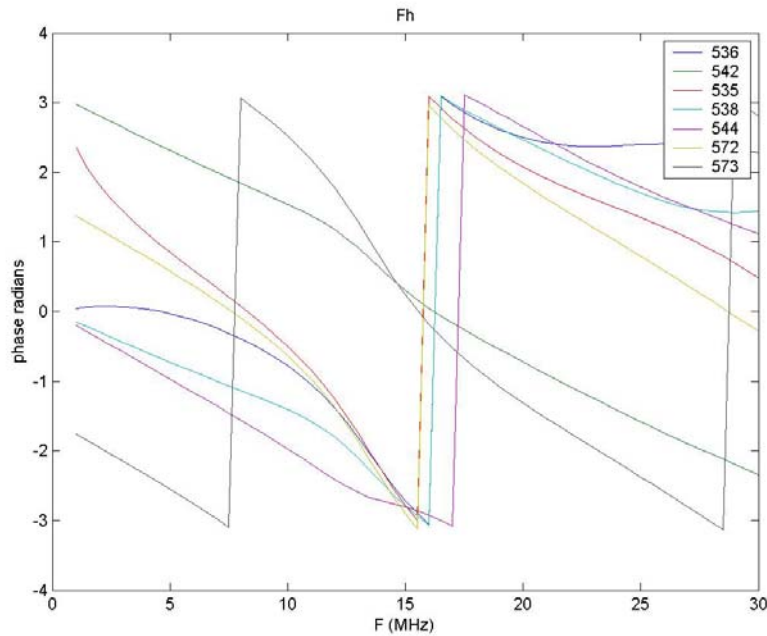*Figure 27 Eigencurrent phases for the case of horizontally polarised plane waves incident from the front of the Macchi.: The wing modes #572 and #573 are oppositely phased. Thus, current flows in the same direction on both wings, viewed in Cartesian but not polar coordinates.*
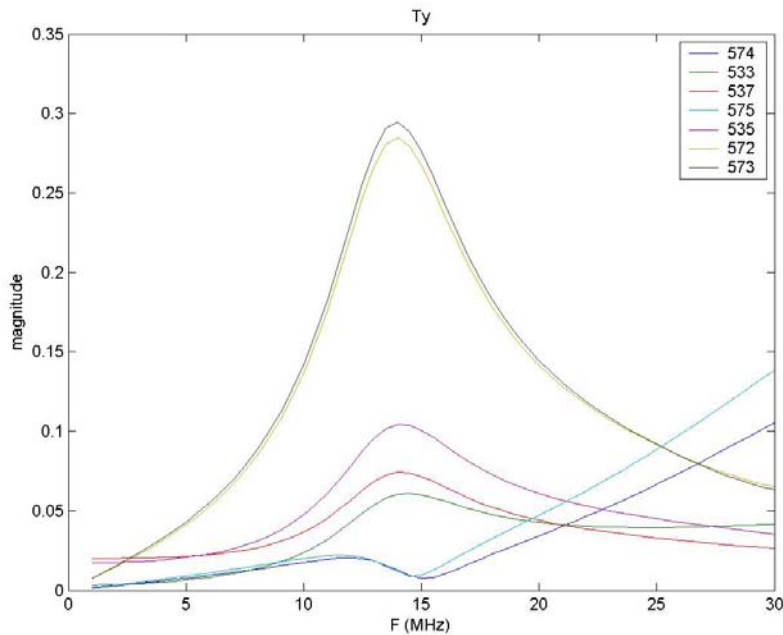

Figure 28 Eigencurrent amplitudes of the Macchi model when exposed to plane waves from above polarised parallel to the wings.

If plane waves are incident from above (zenith) or beneath the aircraft, then due to their transverse nature, they are necessarily horizontally polarised. The electric field may be polarised parallel to the pitch axis (wings) or the roll axis (fuselage). The eigencurrent amplitudes for the former case are shown in Figure 28. The excitation of the wing modes is almost identical to that of Figure 26, with an amplitude of ~0.3. This is strong evidence that the important thing at HF is the electric field orientation to determine the capacitive mode excitation. The main differences relative to Figure 26 are:

- Significant excitation of the tailplane modes #574, #575. These rise steadily with frequency. In the HF range the resonance is not reached due to the small electrical size of the tailplane. The non-excitation of these in Figure 26 may be due to shadowing by the wings.
- A different set of inductive modes. This would be expected as the magnetic field direction is now the roll axis. #535 #537 #533 dominate the inductive modes. From Table 2, the expected modes for this direction of magnetic field are #537, #532, #540, #531.

In Figure 29, the incident plane waves have an electric field vector parallel to the roll axis (fuselage). In this case the plane waves were incident from the side. The effect is dramatically different to the previous two examples, which had an electric field vector parallel to the pitch axis (wings). There is very strong excitation of the fuselage fundamental capacitive mode, #571, which rises to a resonant peak of 0.65 at 12 MHz. The resonance is quite broad, with a 3dB bandwidth of 4 MHz. At 16 MHz, the wing modes #572, #573 appear to receive excitation. This coincides with a change of behaviour of the mode #571, which has a kink in the otherwise smooth resonance peak shoulders. This, combined with the fact that the incident electric field is not ideally polarised to excite the wing modes suggests some coupling between the two modes, which are not true eigencurrents, and hence not necessarily uncoupled at 16 MHz. Of course this discussion is based upon a simplified view of the eigencurrents, which have currents not only on the wings, but also on the fuselage.
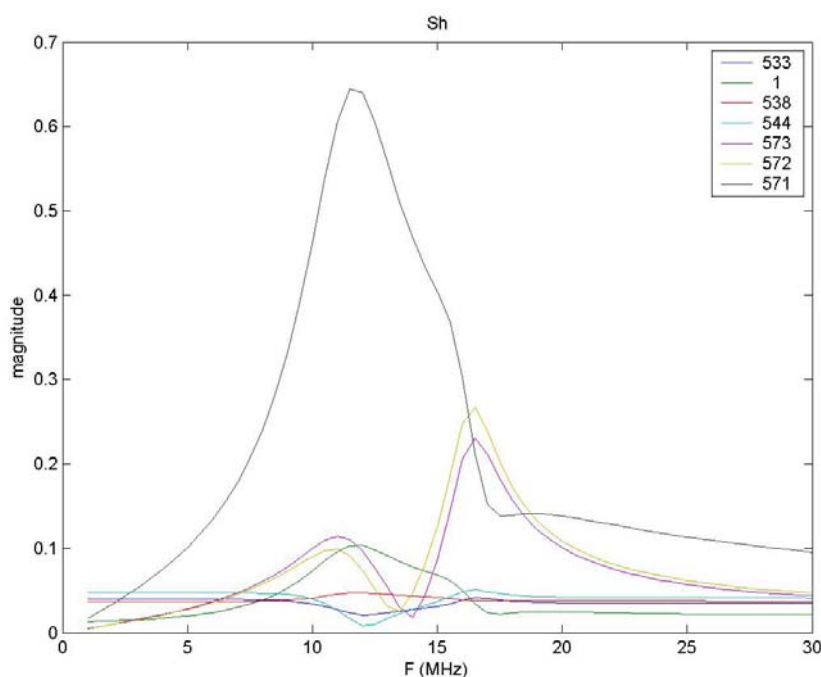
Figure 29   Eigencurrent amplitudes of the Macchi model when exposed to H-polarised plane waves from the side.

A further understanding of the interaction between the wing and fuselage modes may be gained by considering the phase plot, shown in Figure 30. We see that, firstly, the wing modes, #572, #573 have the same phase, and thus are operating in common mode against the fuselage, rather than in the differential or dipole mode of the earlier examples. Secondly, the wing modes have the same phase as the fuselage mode #571 below 12 MHz, but rapidly diverge in phase as the wing resonance is approached at 16MHz. Because of the opposite direction of wing currents for the fuselage mode and the wing modes at the nominal same phase, we can conclude that, below 12 MHz the reason for the wing modes is merely to eliminate currents on the wings. Conversely at the wing resonance of 16 MHz, the fuselage and wing modes have opposite phases, and thus both contribute common mode currents to the wings.

Considering now the inductive modes, we see that #544 #538 and #533 are present[10]. As the magnetic field is vertical and thus parallel to the yaw axis, we see from Table 2 that modes #544 #533 #536 #538 might be expected. The results are thus consistent with the understanding so far established.
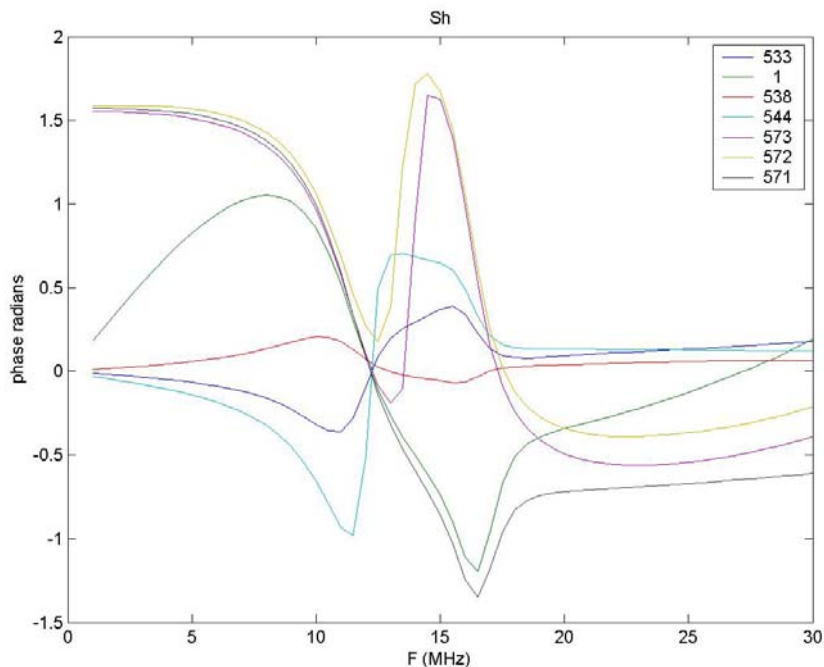
Figure 30   A phase plot of the eigencurrent excitations due to a side incident, H-polarised plane wave.

---

10 Mode #1 is associated with one specific triangle and appears to be an artefact of the modelling.
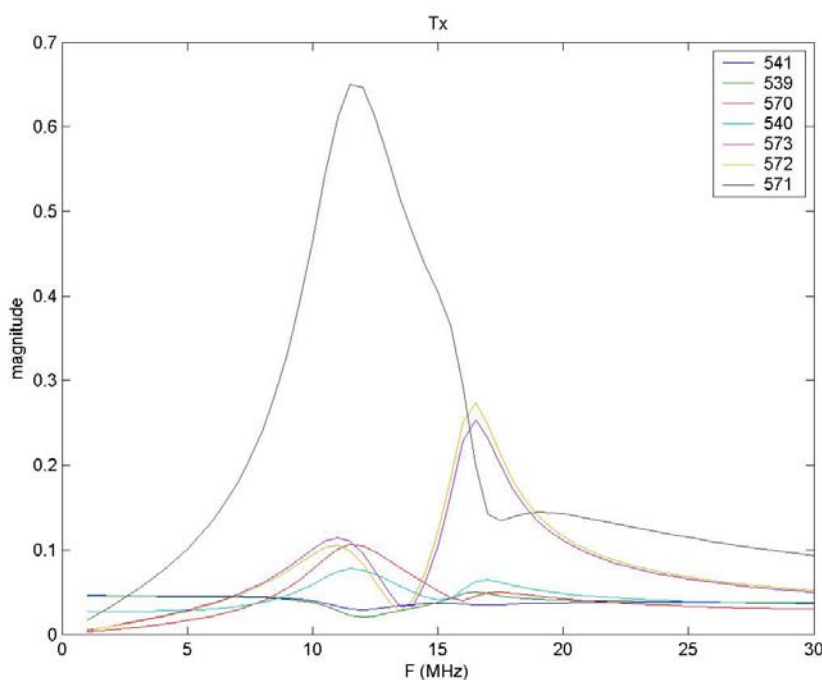
Figure 31 Eigencurrent amplitudes of the Macchi model when exposed to plane waves from above polarised parallel to the fuselage.

In Figure 31, the waves are incident from above (zenith) but the electric field is still parallel to the roll axis. The capacitive modes are, as would be expected, the same as for the case where the field is horizontal polarised but incident from the side, shown in Figure 29. The inductive modes excited include #539 #540 #541. Given that the magnetic field is parallel to the pitch axis, we see from Table 2 that the modes #538, #539, #540, #541 may be excited. Thus the results are consistent with understanding. A curious result is the presence of mode #570, which is a pair of mirror symmetric circulating currents in the plane of the wings. Mode #570 should not be directly excited as it requires a vertical magnetic field. [11] Another interesting result is the fact that the mode is not excited uniformly with frequency as would be expected of a directly excited inductive mode. Instead, it rises in proportion to the excitation of the wing capacitive modes. This suggests that the mode is working to alter the capacitive wing modes, through changing the relative current densities at leading and trailing edges. For reference, the phases are shown in Figure 32.

---

11 Not only must the magnetic field be normal to the plane of the wings, but due to the opposite circulation direction on each wing, the magnetic field must vary in intensity between the two wings. Such a variation would require a curl in the magnetic field parallel to the roll axis.

Figure 32   Phases of the eigencurrents for the case where the fields are top incident and electric field is polarised parallel to the aircraft fuselage.

3.2 Vertical Polarisation

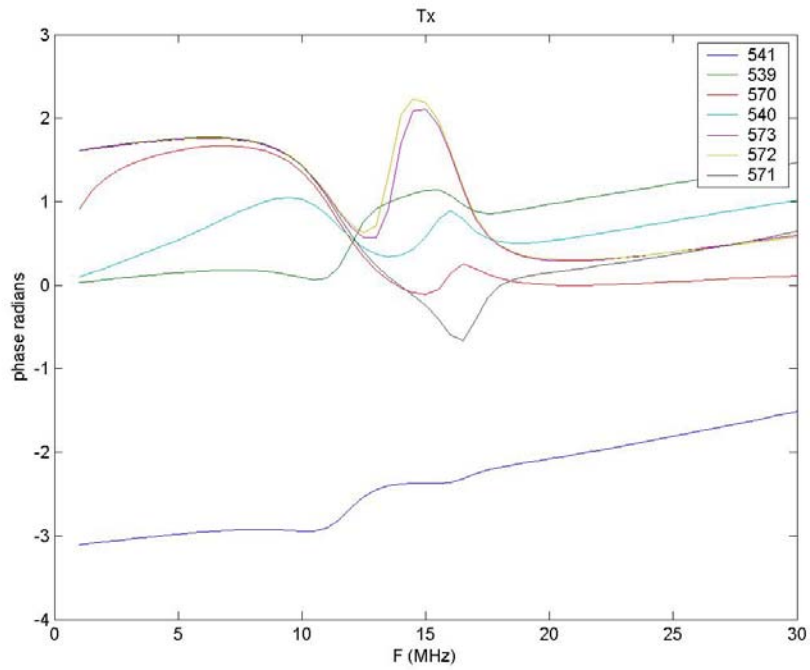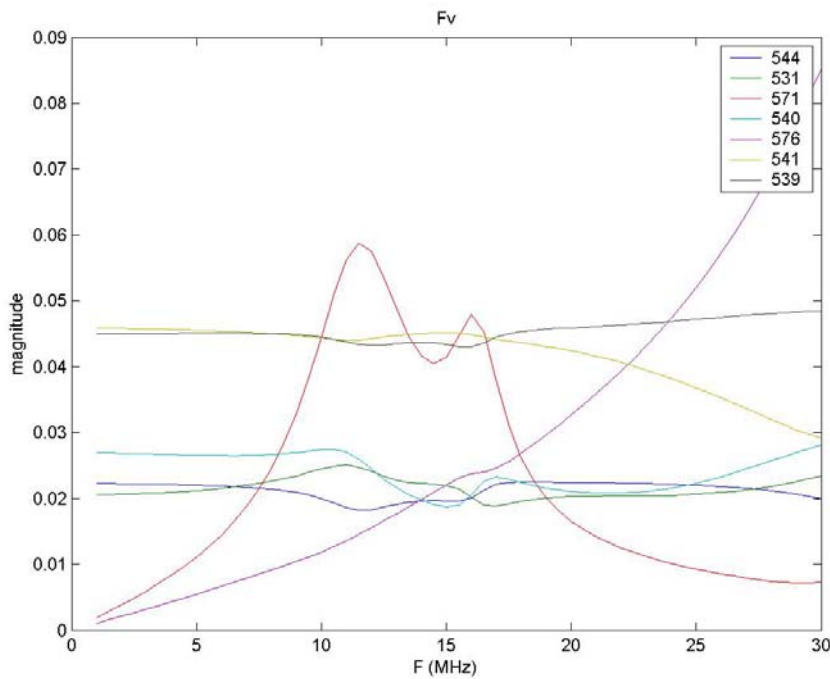*Figure 33   Eigencurrent amplitudes of the Macchi model when exposed to V-polarised plane waves from the front. Note that amplitudes are ~20dB less than for H polarised waves. Wing currents (#572,#573) are barely excited.*

The vertical polarised free-space eigencurrents are shown in Figure 33 and Figure 34. The similarities between the two are most striking:

- Both are much lower (~20 dB) than typical peaks seen for horizontal polarisation. This is due to the electric field not being aligned to any resonant length dimensions to excite capacitive modes.
- The circulating modes are dominant, and of similar overall level (~0.04) to that for H polarisation.
- The fin capacitive mode (#576) can be seen to monotonically increase over the frequency range, as the fin becomes electrically taller.
- The fuselage capacitive mode (#571) is weakly driven (-20 dB) relative to the ideal horizontal polarisation but still forms a significant mode. It has a double peak at 12 and 16 MHz. It may be being parasitically excited by the fin component, which, being asymmetrical, introduces an effective slope to the average, apparent fuselage axis so it presents some component to vertical electric fields. The apparent slope may be computed by taking the arcsine of the relative excitation (~0.1) which gives ~6 degrees for the apparent slope, which would agree with visual estimation. This hypothesis could be tested by exposing the aircraft to a field with electric field tilted ~6 degrees from the vertical towards the nose. The above explanation would predict that #571 mode would be unexcited.

The main differences are the sets of inductive modes excited. In the case of frontal excitation, Figure 33, modes #539, #540 and #541 are dominant, which is consistent with Table 2 in that these modes have a circulation about the pitch axis, and hence are excited by magnetic fields parallel with the wings. This is the case for vertical polarised electric plane waves which are incident from front or rear.

In the case of the waves which are incident from the side, as in Figure 34, the dominant inductive modes are #532, #540, #531, #537. Looking at Table 2, we expect #532, #537, #531 and #540 to be excited by magnetic fields parallel to the roll axis, as is the case here. We would not expect current circulation on the fin, which is a part of mode #531. However, the eigencurrents must be understood in combination together as complex quantities. The presence of a current on a particular aircraft part is not implied by the presence of an eigencurrent having current on that aircraft part: It is possible for this current to be cancelled out by a suitable eigencurrent with currents on that aircraft part. Thus, the fin circulation may be being cancelled by the presence of suitably phased mode #535. The #531 and #535 modes can be seen to have similar magnitudes. The phases are shown in Figure 35. It is clear that the phases are also similar. Thus it is likely that the fin current circulations are being cancelled by the presence of the two modes.
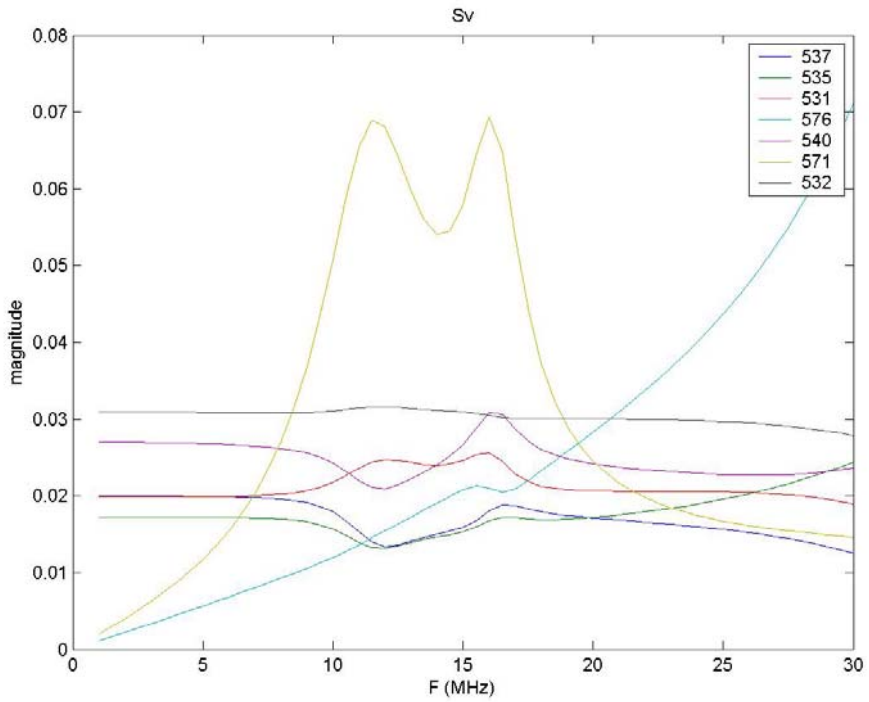
Figure 34 Eigencurrent amplitudes of the Macchi model when exposed to V-polarised plane waves from the side. The ramping up blue line (#576) is for the capacitive currents in the fin, which are approaching resonance.
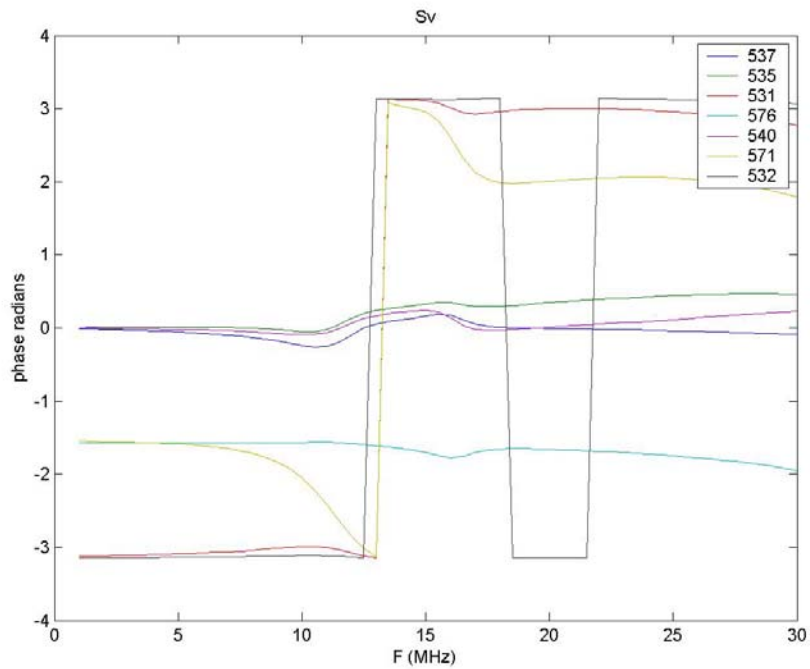

Figure 35 Phases of the eigencurrents for the case of vertical polarised waves incident from the side.

3.3 Summary

In summary, the skin currents on the Macchi in free-space may be simply understood as follows:

- A variety of inductive eigencurrents of relatively uniform amplitude with frequency exist. They combine to produce a current density approximately equal to the magnetic field intensity, H on double-skinned structures. The modes excited depend on the orientation of the incident magnetic field. The inductive modes are dominant for vertically polarised electric fields. Thus control of the capacitive eigencurrents is unlikely to be effective for DCI simulation of vertically polarised electric fields.

- Varying amounts of the six capacitive modes for the wings, fuselage and tailplane and fin are excited. The capacitive modes dominate the inductive modes for horizontally polarised electric fields. The relative amounts are highly dependent on polarisation and frequency, with maximum amplitude achieved at 12MHz for the fuselage with electric field parallel to the fuselage, and at 14MHz for the wings with electric field parallel to the wings. The tailplane doesn't achieve resonance in the HF band, but experiences steadily increasing excitation over the band, if the incident electric field is parallel to the wing/tailplane. The fin is also sub-resonant in the HF band and can be seen to steadily increase in amplitude over the band for vertical polarised electric fields.

- Some apparent coupling is seen between capacitive modes at resonance and between capacitive modes and the inductive modes.

- To be correctly understood, the significant eigencurrents excitations must be considered together as complex quantities. It is possible for a set of eigencurrents to interact to eliminate currents on a particular aircraft part, or to increase them.

- A more speculative thought follows; In using a TEM cell to provide vertically polarised electric field testing for a whole aircraft, one should perhaps focus on providing H field uniformity, rather than E field uniformity. Furthermore, one should perhaps control the inductive modes not the capacitive modes, as the inductive modes dominate. Capacitive modes, which may become very high in Q in an enclosed environment, could be damped without much effect on the inductive modes.

4. Low Level Swept Current - Skin Current Distributions

Low Level Swept Current (LLSC) Bulk Current Injection (BCI) is widely acknowledged to be an acceptable means of testing aircraft at low frequencies. Underlying this approach is the understanding that the cable bundle currents are the main means of coupling of energy into avionics in the low frequency range. Thus any new method of testing must be able to show equivalence to LLSC in terms of the currents coupled to the cable bundles. The main reason for studying LLSC in this work was therefore to compare the DCI method against LLSC in terms of the currents coupled to the cable bundles.[12]

---

12 Sceptical readers may insist that equivalence should be shown between LLSC-BCI and DCI in terms of system upsets. However DCI should not reproduce the systematic errors of the bulk current injection part of LLSC-BCI and thus it should not be expected to show comparable system upset performance, in the opinion of the author. There will be more about this in the next section.

However, if it can be shown that DCI can achieve equivalent performance to LLSC, it should not be assumed that this is a sufficient goal. DCI could substantially improve upon LLSC-BCI by:

- Achieving more realistic distribution of currents among the wires in a bundle; BCI imposes a total current upon a wire bundle with the distribution depending inversely upon the wire impedances, and not at all upon the original (LLSC) distribution.
- Achieving current distributions, both on the skin and cable bundles, which are more representative of free-space than LLSC achieves;

In this section, the LLSC skin current distributions are considered. They will be modelled, and the model will then be validated with measurement. Finally, the modelled skin currents will be compared against free-space using the eigencurrent method. The performance in terms of bundle currents will be left to a later section for comparison with the DCI method.

4.1 Measured results and model validation

In any OATS work, a vital step is to measure the performance of the antenna system, through obtaining the electric field level applied by the various antennas at the location of the (absent) test item. Eight measurements were made at the centre of the test site at a height of 2 m above the PEC ground plane. Only measurements of the principal electric field polarisation[13] of each antenna were made. Using the equipment setup shown in section A.6, complex transfer function measurements were made using the PC controlled Vector Network Analyser of a propagation path including:
- the return fiberoptic equipment,
- the D-dot probe, integrator and low noise amplifier,
- the power amplifier,
- all associated cables and switches and
- the intended measurement – the propagation loss and phase from the feed point of the antennas to the electric field at the test item.

The raw magnitude data gathered this way is shown in Figure 36. It can be seen that a quite low signal to noise ratio was obtained, despite the use of a 30 dB low noise amplifier and integrator following the D-dot probe. The step increase in noise at 15 MHz appears to be due to the VNA switching between different internal RF circuitry at this point.

---

13 Earlier in this report, it was pointed out that at low frequencies, the horizontal antennas will produce non-TEM conditions characterised by low impedance, and a magnetic field component parallel to the propagation direction, due to the multi-path conditions.
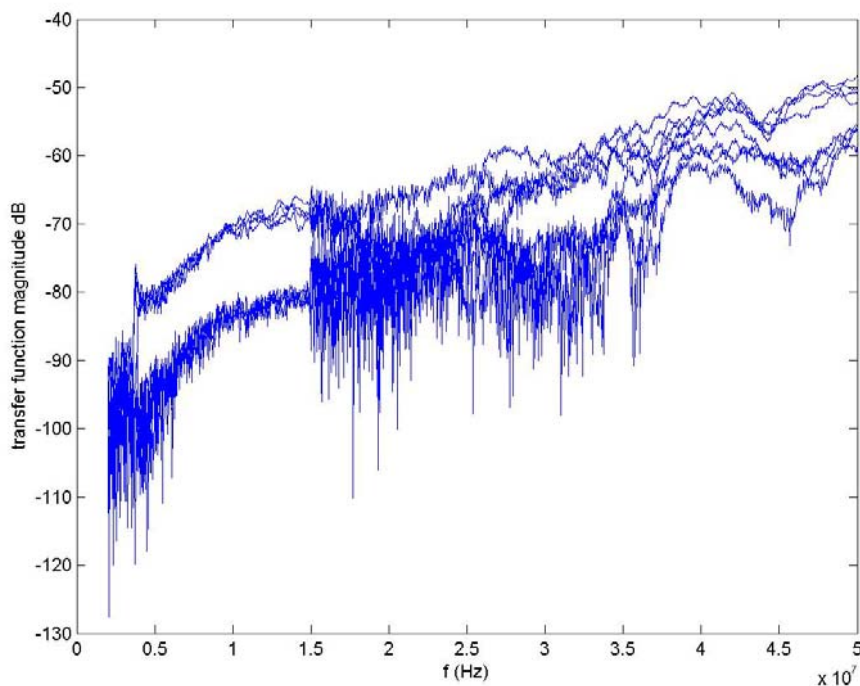
Figure 36   The raw data gathered using the D-dot probe and the 8 HF antennas. Significant noise is present.

One approach to improving the signal to noise ratio is to make multiple measurements and coherently average them. Instead of doing this, the redundancy of frequency points was used: 1201 points were taken which is at least an order of magnitude more than is required to capture the behaviour of the signal. Due to the slowly changing signal versus frequency, a moving average filter can be used to average adjacent values thus achieving the required result. Before taking this step however, the phase slope associated with the long delay must be removed, or the adjacent values will vary too much in phase and they will become incoherent. The phase slope is easily added back in after smoothing. In Figure 37 the data has been filtered in this way using a moving average filter of length 20. A 13 dB signal to noise ratio improvement should result and the figure shows significant signal to noise improvement. A result of the moving average filter is that the lowest 20 frequency points are biased towards zero because of zero padding. This corresponds to frequencies in the range 2 MHz-2.76 MHz.
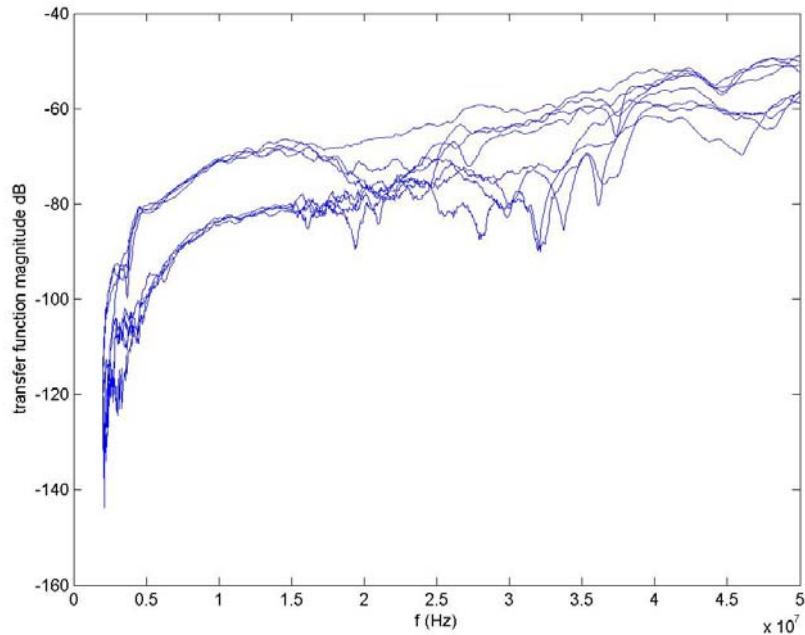
Figure 37 OATS calibration curves for the eight antennas with a 20 point moving average filter applied to reduce noise.

The Macchi aircraft was then placed on the insulated columns designed to place its axis 2 metres above the OATS ground plane, and was instrumented with 14 skin current (J-dot) probes as described in the Appendix A: and Appendix B: . It was then irradiated using the eight antennas while the complex skin current measurements were made. (Measurements were also made of the cable bundle currents but are not relevant in the present section.) Measurements were also made for calibration of parts of the propagation path of no interest, such as:

- Directional coupler to antenna to electric field level (as described above)
- Fiberoptic cables and small signal amplifiers
- Skin current probes

These dimensionless complex transfer functions were then divided out of the total transfer function to leave the transfer function: (Skin current density (A/m))/(electric field at the centroid (V/m) which has the unit the Siemen, as it is an admittance.

These transfer functions may then be compared against those modelled. Only a very small subset of the comparisons created will be plotted here as the data is quite vast – there are eight antennas, (times) fourteen current positions, (times) six numerical models, (times) two data types – magnitude and phase to be plotted, requiring 1344 graphs and thus about 600 pages if of legible scale. Complete comparison data for one antenna position – only one antenna position was modelled – is contained on the attached CDROM, and is described in C.2. In all the following cases, the comparison is for the starboard horizontal antenna.

The first model was of an aircraft above a PEC ground plane (400 m square) using UTD for the ground plane interaction with the MoM aircraft to reduce computational requirements. No half space was included. This model generally produced too high current levels at low frequencies. A typical example is shown in Figure 38. In this case the right, horizontal antenna

was used. The location number one[14] is plotted, which is a horizontal current density on the nose on the port side of the aircraft. Other locations produced much better agreement, especially at higher frequencies. This suggested that the difference lay in the infinite modelled ground plane, causing very low field impedances – and hence high magnetic fields - at low frequencies.
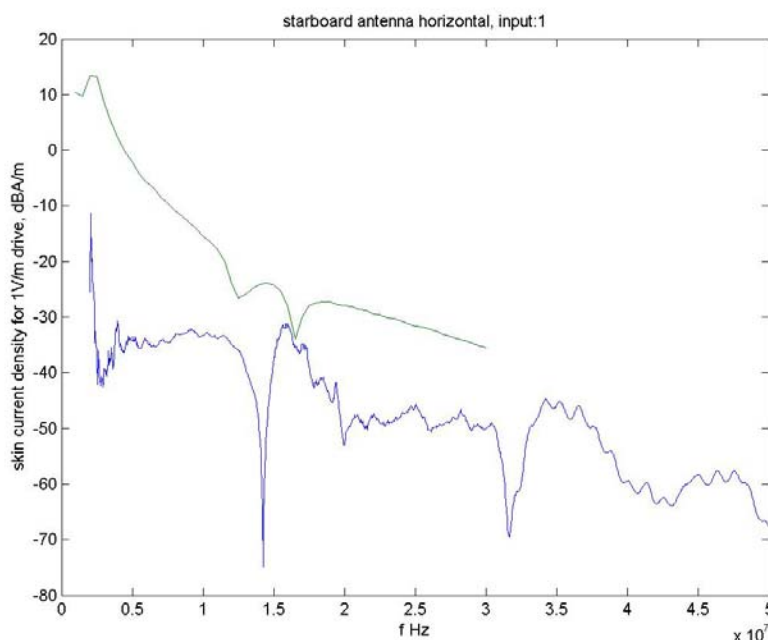
Figure 38   Skin current density for the position 1 (nose, horizontal direction): A comparison between measurement and a numerical model with PEC ground plane 400 m square.

The next model contained a finite ground plane 20 m in diameter underneath the Macchi, but also located in free space – that is without any half space to represent the earth. The current density for this model is shown in Figure 39 for the same current measurement position as the previous case. Much better agreement is obtained. The location of the null at 14 MHz is very well reproduced and generally the agreement is good to within 6 dB. This result is typical of those produced.

The huge difference between the small and large ground plane is concerning as it suggests that the variable and unknown dielectric and conductive properties of the underlying earth – effectively unshielded by the small ground plane at low frequencies - may have a significant effect upon the currents induced on the aircraft. Thus some dielectric earths were included in the model using the half space Green's functions available in FEKO. This trial was cursory rather than comprehensive, as the range of parameters, including layered grounds is too vast, and also the focus of the work is to obtain comparison with DCI not to investigate LLSC in its own right. One model, included a homogeneous half-space of permittivity 7, conductivity 0.02 S/m, which commences 0.1m below the 20 m diameter ground plane. The current density comparison for this model is shown in Figure 40. The result is not much different to the model without the earth, however the resonances of the ground plane, seen as peaks at 2.5 MHz and 8 MHz are considerably damped.

---

14 A diagram showing test point locations on the aircraft is contained in Appendix C.
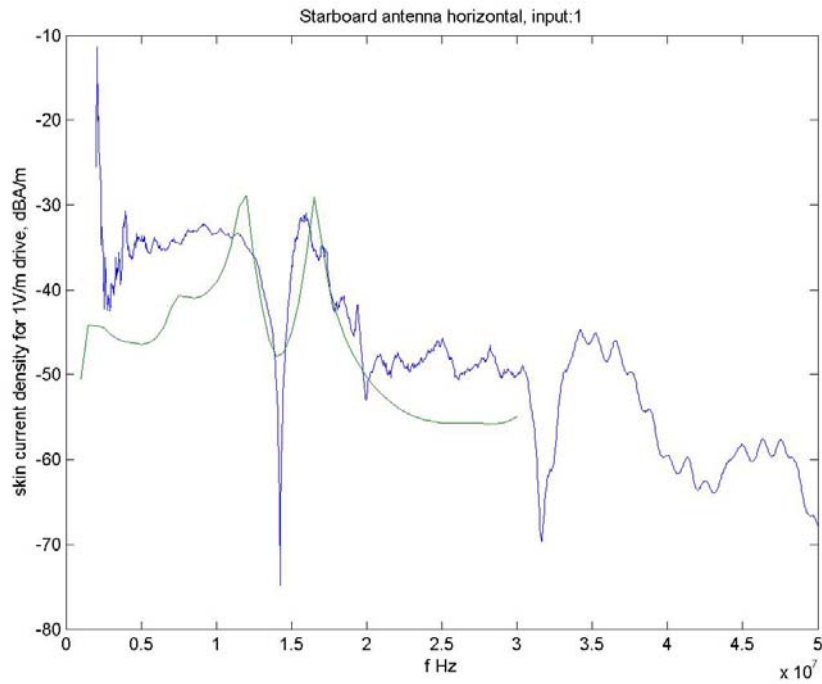
Figure 39   Skin current comparison between a model having a 20 m diameter ground plane and measurement
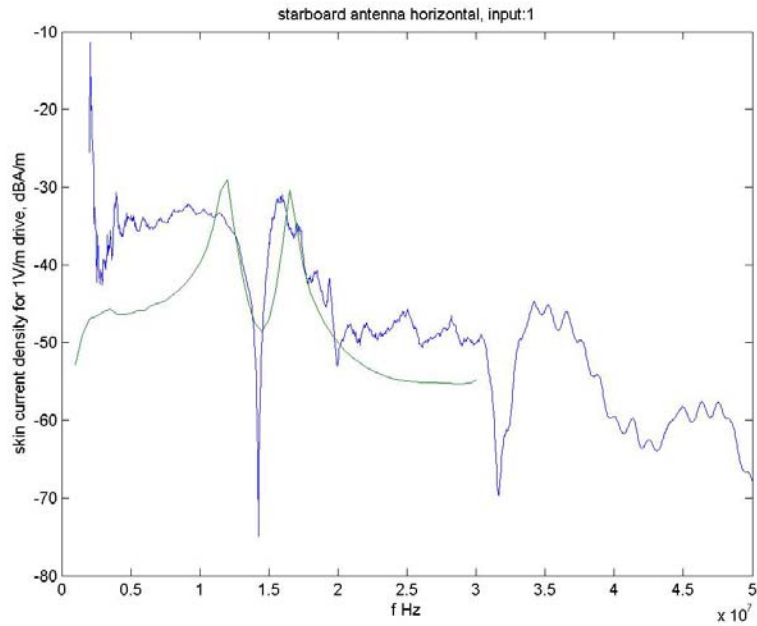
Figure 40   Skin current comparison for a model with a 20 m diameter ground plane above a dielectric earth

Another model included the coaxial cables arranged from the central OATS pit (where they may be connected to the coaxial from the power amplifier) out to the antennas. These are long conductors with potentially low frequency resonances which could affect the calibration fields measured, if not the currents coupled to the aircraft.
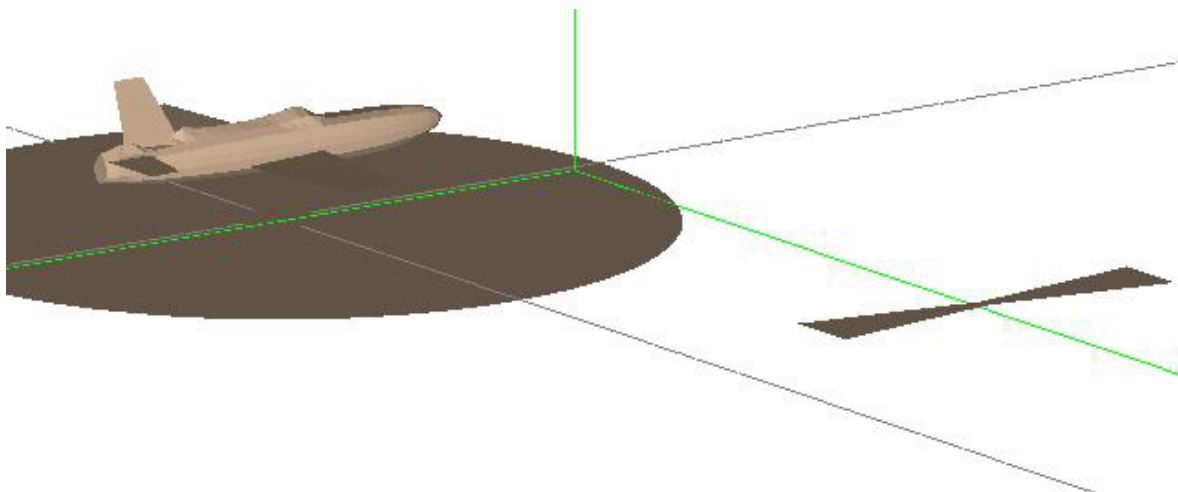
Figure 41 The model adopted as best matching the measurements of skin currents. It includes 4 floating wires, which represent the coaxial lines to the antennas. A lossy ground was included with epsilon relative = 3, loss tangent = 0.1.

The layout of the model, with meshed MoM ground plane, Macchi, bowtie antenna and coaxial lines (represented by four floating wires shown as grey lines) is shown in Figure 41. The resulting current comparison for the same position as the earlier figures is shown in Figure 42. This model successfully reproduces the peak in the skin current seen at 3 MHz. To obtain the correct position of the 3 MHz peak, a range of dielectric ground properties were used, with relative permittivity of 3, loss tangent of 0.1 providing the fit shown. The peak can be interpreted as a result of the presence of the coaxial lines to the unused nose and tail antennas, which have coupled additional energy to the aircraft at the resonance of the coaxial lines. Incidentally the internal, coaxial nature of the coaxial lines is irrelevant to the model; only the exterior conductor plays a role.

Considering the plot, the overall agreement is satisfactory, with typical disagreement of 6-7 dB in two regions, and very close agreement elsewhere. However the null is not as deeply formed in the model. Null depth can be sensitive to small parameter changes, and this is not considered a serious issue. [15] The measured data appears to be lower Q in its resonances than the modelled data. Several variations of half-space permittivity were tried in an attempt to couple more ground losses to the aircraft model resonances. However the agreement with measurement could not be significantly improved. The discrepancy could be a result of any or all of the following:

- Greater losses in the (real) aircraft skin mainly due to panel bonding contact points;
- Lack of radiation purity in the (real) antennas due to common modes excited on the feed cables radiating vertically polarised fields;
- General modelling geometry errors.

---

15 Note that the 'spike' in the measured data as the frequency tends to zero, is an artefact of the calibration data moving-average filtering, in which the lowest 20 data points are averaged with padded zeros.
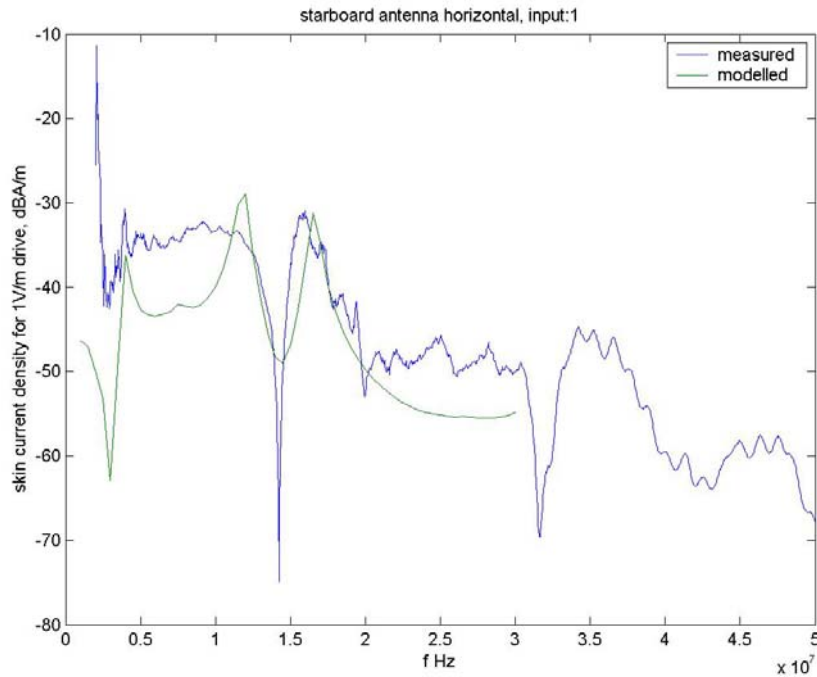
Figure 42   Skin current density comparison for a model having circular ground plane, radial coaxial lines and a lossy dielectric half-space with OATS measurement

There was insufficient time to positively identify the cause of the remaining disagreement. Although this was disappointing, the understanding of LLSC was never the aim of this work. However, any errors in the modelled LLSC skin currents will flow through to the DCI generated bundle currents, which are controlled using model-based eigencurrents: The comparison has considerable opportunity to accumulate errors, as it is based on modelled currents in both the DCI and LLSC situations, and measured bundle currents in both situations. This will be discussed further in section 5.4.

A few additional current locations magnitudes and phases are now considered with a view to validating the LLSC model. For complete validation data, the reader is referred to the enclosed CDROM.

It is interesting to consider the current density on the opposite side of the aircraft nose, to see to what extent the asymmetric excitation causes bilateral asymmetry in the currents.
The distribution is shown in Figure 43. Note the much smaller null in the measured data.
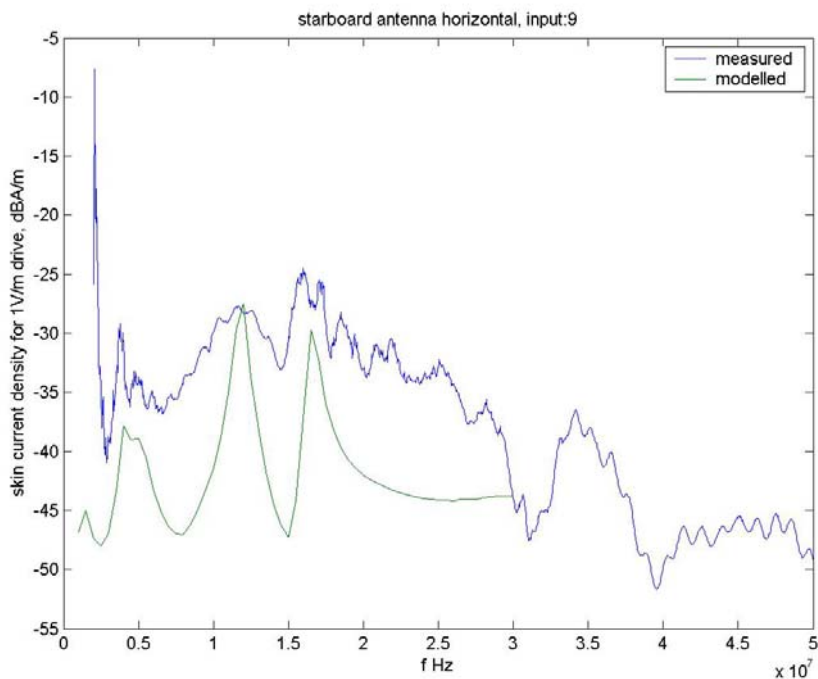
Figure 43 Skin current comparison on starboard side of nose

A plot for the port side of the tail, horizontal current density is shown in Figure 44. The level of agreement is similar to the equivalent location near the nose.
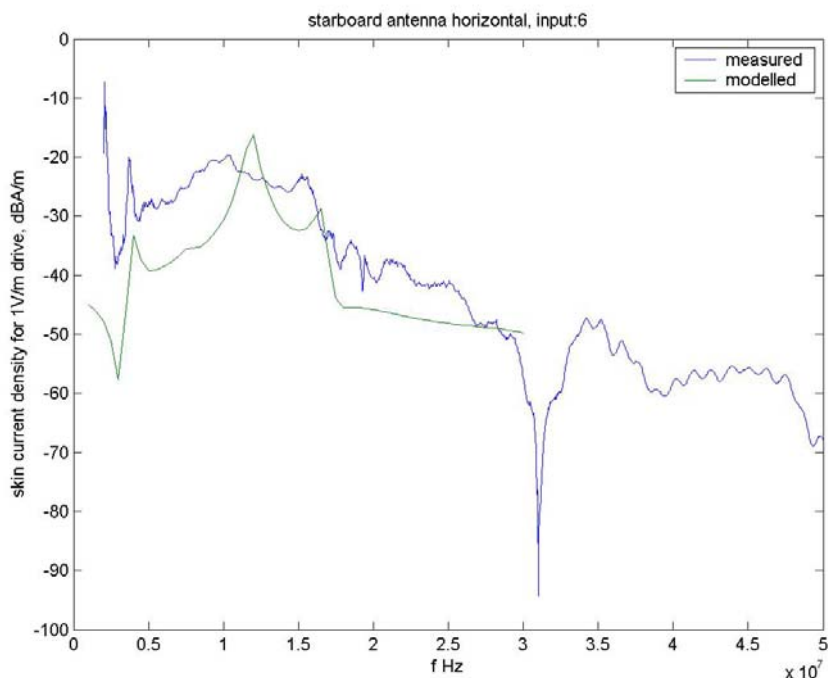
Figure 44 Skin current comparison, port side of tail

It is also interesting to see the agreement in the vertically oriented skin current densities. The port side nose location is shown in Figure 45. The current levels are generally much lower, reflecting the polarisation direction of the exciting antenna – which is horizontal.
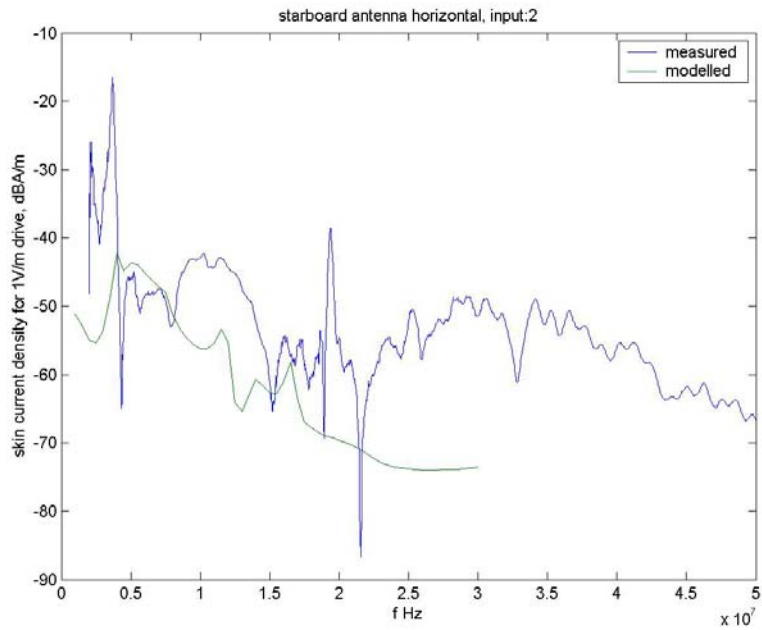
Figure 45 Vertically directed current density

To emphasise that the measured and modelled data are all complex, the phase is shown in Figure 46 for the same location and direction as in Figure 43. The overall agreement is very good, when it is considered that very large calibration phase gradients have been wound out of the measured data, which results in an accumulation of errors. The large apparent error at 17 MHz is not as bad as it appears when one remembers that phase is cyclic, and the data has just crossed the pi radians limit from negative to positive definition. It may be worthwhile to recall that the plots all compare the ratio of the measured complex current density to the horizontal electric field level at the aircraft centroid (when the aircraft is absent). Thus the phase slope measures the delay (or advance) that occurs between the driving field at the centroid and the skin current.
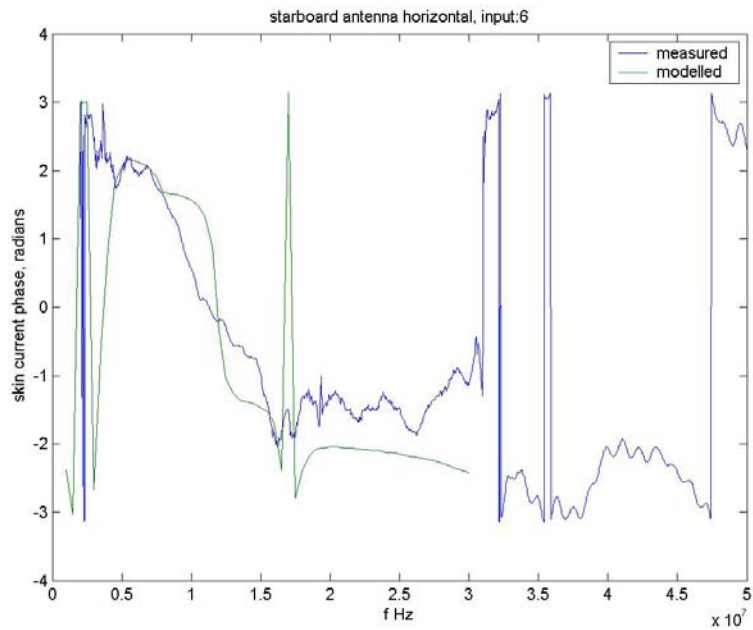
Figure 46 Comparison of current phase of the current density at location 6

4.2 Modelled results – Eigencurrent behaviour

The best matched model geometry was shown in Figure 41. This used a MoM modelled PEC ground plane beneath the Macchi, and a set of 4 wires, floating with respect to the other PEC components, which represent the outer conductors of the heliax coaxial lines used to convey the RF power from a central pit to the four antenna pairs surrounding the ground plane.[16] This was all placed over a dielectric ground with relative dielectric constant 3, and loss tangent 0.1. As is the case with the earlier comparisons with measurement, two runs of the model were taken. One run was without the aircraft present to record near-field electric field values at the aircraft centroid, to enable subsequent calibration of the eigencurrent amplitudes and point skin-current density values. This is analogous to the method used for LLSC in actual HIRF testing.

Having developed a validated numerical model for the LLSC situation, it is now possible to apply the eigencurrent analysis to compare the LLSC situation against the ideal, plane wave free space situation which it attempts to simulate. The LLSC amplitudes of the seven most significant (in free space) eigencurrents are compared with the free space situation where the plane wave field is incident from the same direction in Figure 47 to Figure 50.
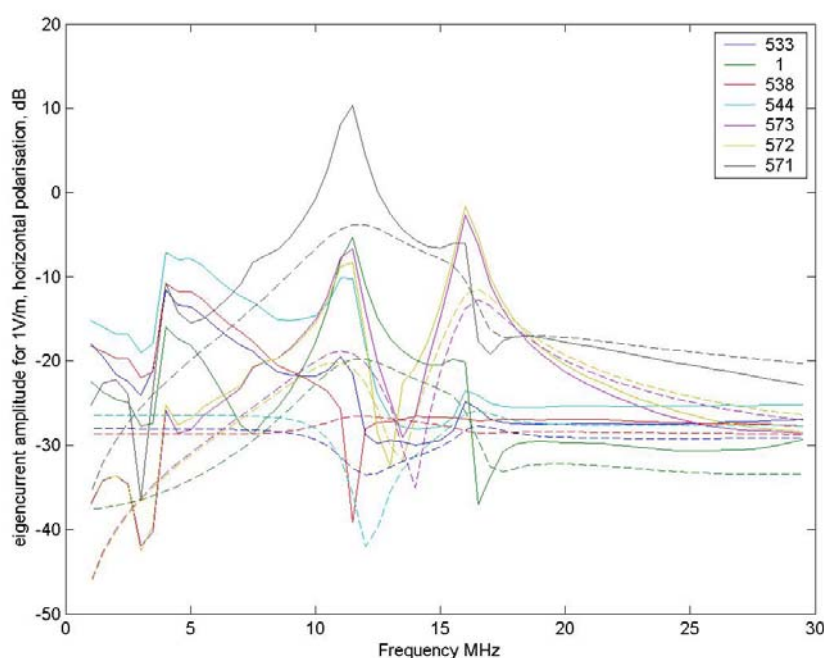
Figure 47   The seven strongest eigencurrent amplitudes for the horizontally polarised LLSC (solid lines), with starboard side illumination, compared on a dB scale with the equivalent plane-wave free-space situation (dashed)

---

16 Although only one heliax is used at any time, the other three are left in position, due to their weight and awkward handling characteristics.
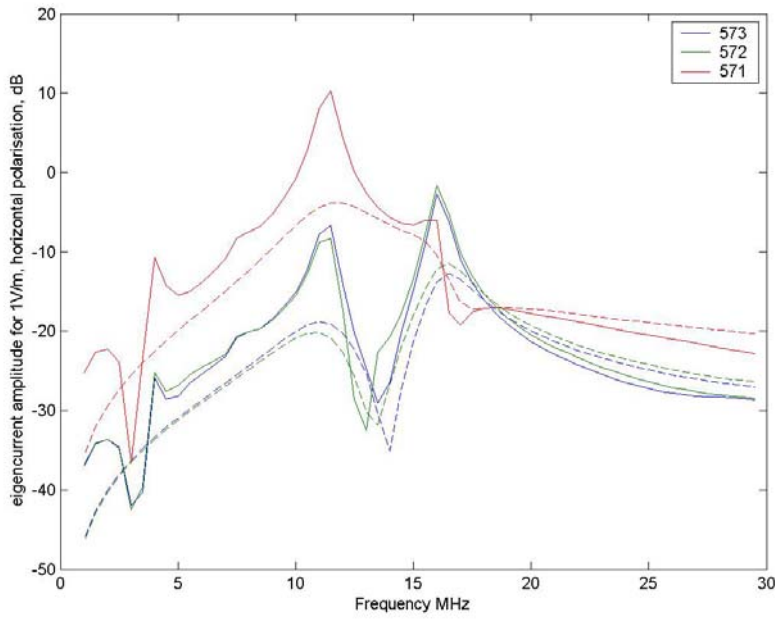
Figure 48   The three largest capacitive eigencurrent amplitudes for the LLSC situation (solid lines) plotted together with free space amplitudes (dashed). Though similar in level above the wing and fuselage resonances, the LLSC amplitudes have higher Q resonances, at 12 MHz and 16 MHz, where the fuselage and wings resonate, and also show a peak at 4.5 MHz due to the resonant behaviour of the ground plane and heliax cables.
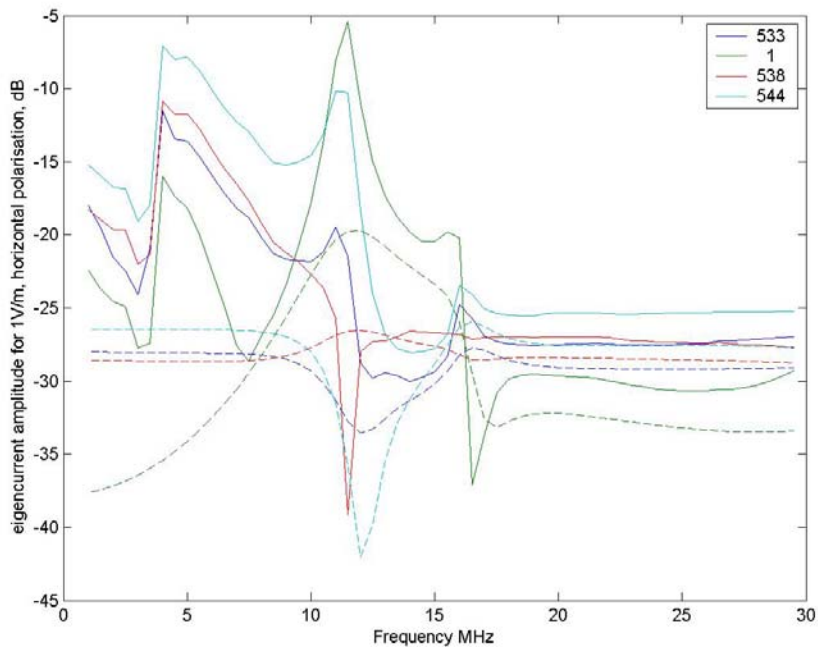
Figure 49   The four largest inductive eigencurrent amplitudes for the LLSC situation (solid lines) plotted together with free space amplitudes (dashed). Though similar in level above the wing and fuselage resonances, they are over-excited by about 20 dB in the resonant range.
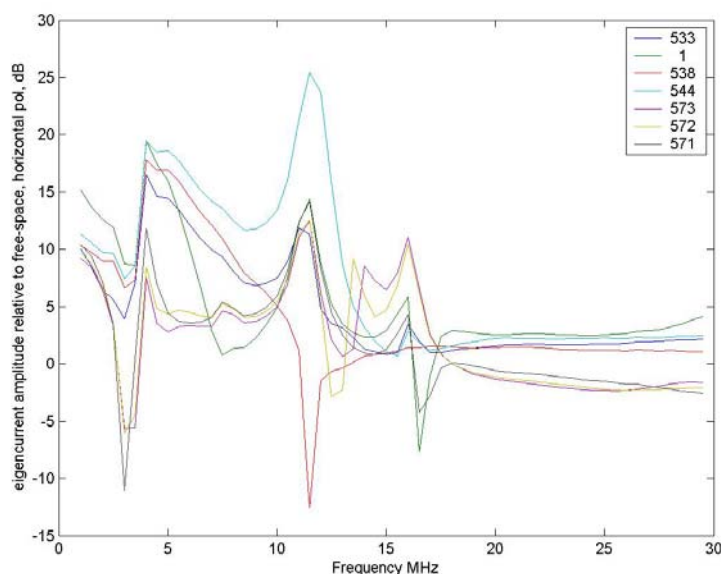
Figure 50. The seven strongest eigencurrent amplitudes, divided by the free space amplitudes and plotted on a dB scale. The 0 db level represents perfect performance of the LLSC environment.

The results of the comparison with free-space are interesting:

- All eigencurrents are close to free space excitation above 16 MHz.
- The fundamental fuselage capacitive mode, #571, is resonant at the correct frequency, but is over excited at resonance and appears much higher in Q. This is consistent with the presence of the PEC ground plane reducing the amount of radiated energy from the mode, resulting in less damping and higher Q. A similar heightening of the Q is apparent for the wing modes, #572, #573.
- The inductive eigencurrents are well behaved above 16 MHz, but are progressively more over-excited as the frequency decreases toward 4 MHz. The worst case is 20 dB at 4 MHz.
- The finite ground plane and heliax wires produce a peak 20 dB above correct levels for all eigencurrents at 4 MHz. Interestingly, this is mainly a result of the calibration procedure; there is a 20 dB dip in the field measured at the calibration point, whereas the uncalibrated amplitudes are relatively smooth in this region. Yet, calibration is an integral part of the LLSC method. This problem is easily avoided if the unused heliax cables are removed during testing.

The third phenomenon may be explained through the existence of an excessive level of magnetic field relative to electric field for a horizontally polarised wave system near a horizontal PEC ground plane. The relative increase in H field may be estimated by the use of Maxwell's curl equation for the magnetic field:

$$\frac{\partial B}{\partial t} = -\nabla \times E$$

Let the horizontal electric field have an x direction, with y being the direction of propagation of the waves. From the above equation we obtain, assuming only x component of electric field:

$$\frac{\partial B}{\partial t} = -\hat{j}\frac{\partial E_x}{\partial z} + \hat{k}\frac{\partial E_x}{\partial y}$$

Normally, for an infinite plane wave, only the partial derivative with respect to the direction of propagation (y) would be involved and this gives the usual transverse magnetic field related to the electric field by the impedance of free space. However, in the case of the near field of the PEC ground plane, the electric field has a partial derivate with respect to z also, since it must increase from 0 V/m at the PEC surface to the calibration level at the aircraft centroid, say 1V/m. Note also, that the resulting magnetic field is not transverse to the electric field, but parallel to the direction of propagation. To estimate the relative size of the two components of magnetic field, an example may be considered: Let f=4 MHz, hence λ=75 m. The partial derivative of E_x with respect to y will change from 0 to peak (1 V/m) in one quarter wavelength or 19 m. However the partial derivative with respect to z will change from 0 at the PEC surface to 1 V/m at the calibration height of 2 m. Thus we could expect the magnetic field from the latter effect to be 19/2=8.5 times as strong or 19 dB greater. This is the order of over-excitation of the inductive modes at 4 MHz seen in Figure 50. At still lower frequencies, this effect would become greater if the PEC ground plane was infinite (or 400 m in width as described in an early model). However in this case, the finite size of the ground plane causes its effects to diminish below the ground plane resonance frequency, where it becomes electrically small.

4.3 Discussion

The horizontally polarised OATS LLSC method used at HF was shown *in modelling* to over-test[17] the aircraft at very low frequencies by up to 20 dB and to also over-test the aircraft at fuselage and wing resonances by up to 15 dB.

The low frequency (4 MHz) over-test is probably least significant, as very low bundle current signals are found here anyway due to both the difficulty of achieving adequate external field strengths and the reduced coupling to the cable bundles. The common practice is to use the lowest measurable coupling levels, at say 5 MHz and project these coupling levels (as a constant level) to lower frequencies. This is a conservative assumption as when the fuselage goes below resonance the coupling levels typically fall at 20 dB per octave. However even at 5 MHz, there is significant over excitation of the inductive eigencurrents evident from the modelling of ~ 15 dB. It would be interesting to determine the relative significance of inductive modes in the generation of coupling to bundles. Intuition, a notoriously fallible guide to RF behaviour, suggests this might be less than for capacitive modes

Of more concern is the over-test in capacitive modes at the resonances. However, the measured skin current data did not appear to display such high Q resonances as the model, being ~6 dB lower in current density at resonance than the model, and this must qualify my model-based critique of the LLSC method. The expectation of the resonance over-test could be used to reduce the coupling levels measured at fuselage and wing resonances by 10-15 dB with suitable supporting data. Supporting data could include skin current density measurements and modelling. The coupling levels at the resonances are typically the highest measured, and thus are often the point of avionics susceptibility. Such a change might allow an aircraft to pass an intersystem test, which would otherwise show exceedances using the existing practices. It is interesting to note, that the simulation and measurement described

---

17 In this sense 'over test' refers only to the skin currents excited on the aircraft and potentially the bundle currents excited relative to free space. It does not include the errors associated with BCI which would add to the LLSC errors and result in either slight under testing or gross over testing at the resonance frequencies.

used a fuselage height of 2 m. Typically, aircraft are tested on their undercarriages which may position the aircraft significantly lower. This would tend to increase resonance Q and thus LLSC resonance frequency overtest.

Both the above inadequacies in the OATS LLSC could be improved by increasing the separation between the aircraft and the PEC ground plane, such as by using dielectric ramps, or suspension from cranes. An alternative might be to not use a PEC ground plane at all, but use a defined earth material such as dry sand or gravel and strictly control ingress of moisture.

An additional insight from the modelling and measurement done for LLSC, was that it is necessary to remove unused coaxial lines from the vicinity of the aircraft during measurement, as these possess their own resonances which mainly impact on the accuracy of the measured calibration fields.

5. DCI excited Skin Current

5.1 Introduction

In DCI, the RF currents that would be remotely induced on the skin of an aircraft subjected to an EME are applied conductively to the skin, typically with a transmission line. This generally involves a combination of an RF source attached between one point on the skin and a ground and resistive loads attached between one or more skin points and a ground. Together, these are used in an attempt to establish a travelling current wave over the skin.[18] A benefit of DCI is that the method will stress all cable bundles. Thus the cost of performing numerous BCI site tests is avoided. Furthermore, if correct skin current distributions can be achieved, the distribution of currents on wires within a single bundle can be accurate, rather than uncontrolled, as with BCI. In addition, where multiple redundant systems are employed in the avionics, DCI can stress all the systems simultaneously. This is known as synergism, and is difficult to achieve using BCI as it requires multiple simultaneous injection [3].

In fairness to LLSC/BCI and other illumination methods, DCI also has its own limitations. Whereas in far-field illumination, aircraft capacitive skin currents go to zero at the extremities, in DCI they are at their maximum at the injection/load sites which are typically at the extremities. Furthermore, with DCI it is difficult to achieve even remotely accurate excitation of the inductive or circulating currents

All EMC test methods require calibration. In the case of the DCI method, calibration requires that we establish the levels of directly injected current that corresponds to a given electromagnetic plane wave field. Previous workers have approached this in different ways: G.Barber [15] carried out work at DERA in the UK on a ground plane type rig. He measured a transfer function using low level DCI (LLDCI) between DCI current and cable bundle current. He then measured the equivalent Low Level Swept Current (LLSC) transfer function between cable current and applied plane wave field. The two transfer functions can then be divided

---

18 However, given the previous discussion about resonant capacitive modes, it is worth keeping an open mind as to whether a travelling wave ought to be the goal of the technique.

over the frequency band to determine the DCI currents required to achieve the equivalent stress to the electric field specified in the EME. This method is a quite straight-forward extension of EMC calibration methods. Yet, a problem arises as follows: If a DCI skin current distribution could be achieved equivalent to that from the LLSC, then the calibration factor determined would be the same no matter which cable was used. However, at the present state of the art, the DCI skin current distributions do not match those using LLSC and different calibration factors are determined for different cable bundles. Without an understanding of the skin currents, which might be used to improve the DCI skin current distribution, we are left with taking a brute-force approach.

One brute force approach is to simply increase the DCI injected current until all (measured) cable bundles receive at least the same current magnitude as they receive from LLSC. This would seem to be conservative; avionics should be subjected to conditions at least as bad, if not worse than the designed EME.

However, Barber [15] describes using a "correction factor" which is the (dB) difference between the *maximum* coupling envelopes measured for LLSC and LLDCI. Presumably, this is based on the LLSC maximum coupling over all bundles and antennas and the LLDCI maximum over all bundles, and is a function of frequency. This would not be highly conservative, in the manner described earlier. Yet some of the figures have titles referring to "100% Cum Prob correction factor". To provide such a conservative correction factor one would presumably need to take the difference between the LLSC *maximum* coupling envelope and the LLDCI *minimum* coupling envelope. Equally curious, Figure 9 of [15] includes a graph having legends "95% 16 loom corr" and "100% 16 loom corr". Although not described in the text, this hints of a more elegant statistical approach which was also taken to generate the correction factor. DSTL/DERA has not published the exact details of their calibration method anywhere in the public domain to the present author's knowledge, however judging from Figure 9 of [15], the difference between using the statistically elegant 95% correction factor and the brute force 100% correction factor is negligible at all except one frequency.

Barber's validation method was based on creating "upsets" in specially built weak systems. These were actually operational amplifiers coupled to ribbon cable with meter readouts. This method provided reasonable agreement between DCI and free field illumination testing in generating system "upsets" EMV thresholds at up to 150 MHz on a PUMA helicopter. The worst disagreement was ~20 dB at 80 MHz, although the agreement was typically <10 dB. The added value of such artificial "upsets" vis-à-vis cable current measurements is questionable when one considers that the upset is a threshold, and thus effectively provides a one-bit, uncalibrated current measurement. It may have some persuasive value in the broader community, however.

In earlier work by Bolsover et al. [7], skin current density transfer functions were measured using LLSC and again for DCI, in the anticipation of using *them* for calibration purposes. As might be expected, an equivalent problem arose to that based on bundle current calibration: Calibration factors varied between skin current sites and made the choice difficult. The possibility of integrating skin current density around the fuselage was raised but not adopted in the work due to the loss of local variation. The need for accurate phase measurements was not mentioned but possibly also a consideration. In the terminology of the present report, the integrated current would provide a fairly good measure of the fundamental capacitive fuselage mode, while the local variation mentioned is due to the inductive modes and other

higher-order modes. Ultimately, a single loom current was adopted for the calibration based on the quite reasonable argument that it should be a safety critical loom with the highest LLSC transfer function.

All the above methods attempt to adjust the DCI skin currents equivalent to those for LLSC, but as we have seen, LLSC skin currents are not exactly the same as the ideal free-space situation at and below the aircraft resonances. The free-space skin currents are difficult to measure, and are better suited to modelling. However, all the above work does improve upon two fundamental weaknesses of LLSC-BCI; the uncontrolled distribution of current among the bundle wires and lack of synergism.

Apart from bypassing a vital aspect required for understanding and improving the skin current accuracy of DCI, using loom current measurements for calibration does not realise a further potential benefit of the DCI technique: That is the ability to avoid having to access cable bundles on modern aircraft.

The aim of the present work, apart from building knowledge of the state of the art, is to improve the fidelity of the DCI skin currents achieved and thus reduce the extent of over-testing which results from consideration of the cable currents alone. Present methods are based on analytical understandings of the aircraft as a transmission line with travelling waves, which is not a very accurate analogue for the range of aircraft shapes of varying cross section and intersecting wings and fuselage.

To improve the fidelity of skin currents, we need a metric for the currents. Furthermore we need a multi-dimensional metric which can describe, as well as measure, the currents and hence point the way to improvements in injection location or load impedance. The eigencurrent method has been developed for this reason.

In the following sections a range of DCI injection locations and loading scenarios are analysed using the eigencurrents. This was initially exploratory in nature: A range of possibilities of current control were initially conceived including multiple simultaneous injection in order to improve the eigencurrent match to free-space and it was hoped to find injection sites that could ultimately provide a well conditioned matrix in a control situation. Ultimately this level of complexity was not attempted: A single point injection method was adopted and the major three capacitive eigencurrents were controlled, one at a time. However, before describing the method which was more fully explored, some novel injection methods are briefly described, as they may be of interest to the reader. Readers interested mainly in the actual measured and validated DCI method can skip these and go directly to section 5.4.

5.2 Whip Antenna DCI Excitation

In unrelated work by the author, it was found that short HF antennas on aircraft worked well if they were whips projecting from the nose or tail. The reason for the good performance was that the whip antenna was recruiting the airframe to act, not as a ground plane, but as the major part of the antenna, by inducing significant skin currents. Thus the notion was conceived to adapt this method for DCI.

A potential benefit of using the whip antennas for DCI, it was hypothesised, is that by not using load resistors, larger efficiencies could be achieved. The airframe could be induced to

resonate, thus achieving high efficiencies. Because the DCI would take place adjacent to a PEC ground plane, it was recognised that a balanced drive would be preferable. Thus two whips were modelled, each fed in anti-phase, so that the aircraft mid-fuselage would remain at approximately earth potential.

5.2.1 Modelled Results
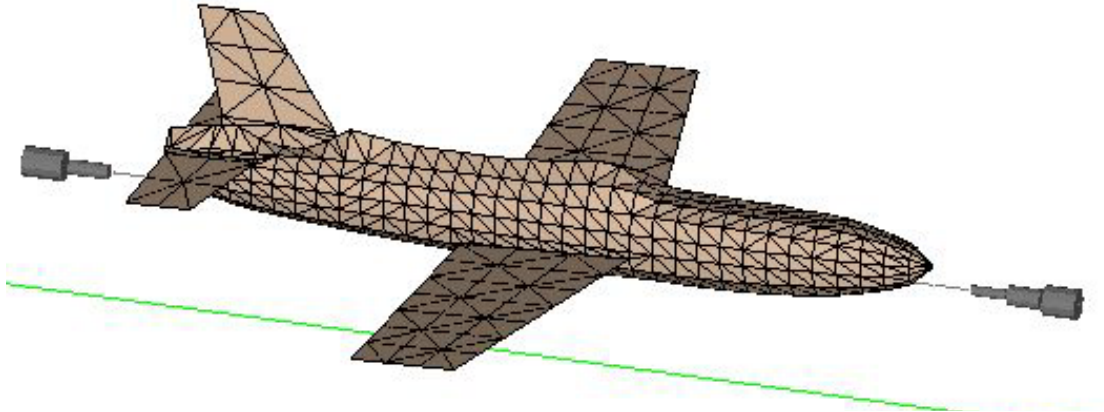
Figure 51   The Macchi model with push-pull monopoles at each end. The monopoles are conical to improve bandwidth.

The model design is shown in Figure 51. Two metre, conical whip antennas extend from both nose and tail. Four metres beneath the model centreline is a PEC ground plane. This was increased from the nominal 2 m to help improve the aircraft's resonance bandwidths.
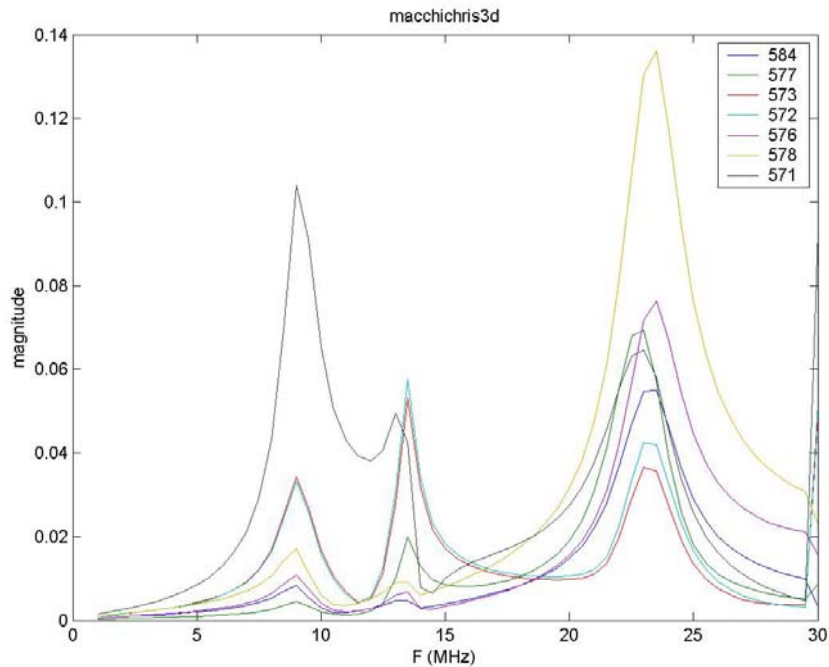
Figure 52   The eigencurrent amplitudes for the Macchi when excited by 2m nose and tail monopoles. The added resonance at 23MHz is an undesirable feature.

The resulting eigencurrent amplitudes when driven by the two 50 ohm sources at 1 V are shown in Figure 52. The notable features of the amplitudes are:
- the appearance of a new resonance at 23 MHz, at which frequency the eigencurrents are dominated by the 3rd order mode #578,
- the reduction in resonance of the fuselage resonance from 12 MHz to 8.5 MHz and
- the complete lack of significant inductive eigencurrents.

The first two effects are probably due to the increase in apparent length of the aircraft from 9m to 13m. The third effect could result from the axi-symmetric nature of the excitation.

The bandwidth of the resonances appear reasonable, however the efficiency of eigencurrent excitation is not much higher than was found in the pyramidal scheme considered later. Doubtless, the efficiency could be increased significantly using better impedance matching, but this would cause a commensurate drop in bandwidths. Practical difficulties may easily be imagined with coupling the massive RF power to the antenna feed points without providing an inductive path to earth.

Given all the above challenges, and especially the undesirable stimulation of the 3rd order fuselage mode, this model was not pursued further.

5.3 Loop Antenna DCI Excitation

One line of thinking was stimulated by the design of the skin current probes developed in this work and the principle of reciprocity: The skin current probes are intended to measure skin current on the aircraft. By the principle of reciprocity, we may expect to be able to use them to also inject skin currents onto the aircraft by feeding RF power into them. However, the existing current probes are not optimised for efficiency, but include other design parameters such as compactness, so that current is measured in a small region rather than averaged over a larger region. To improve the probe efficiency for injection, the loop area was increased.
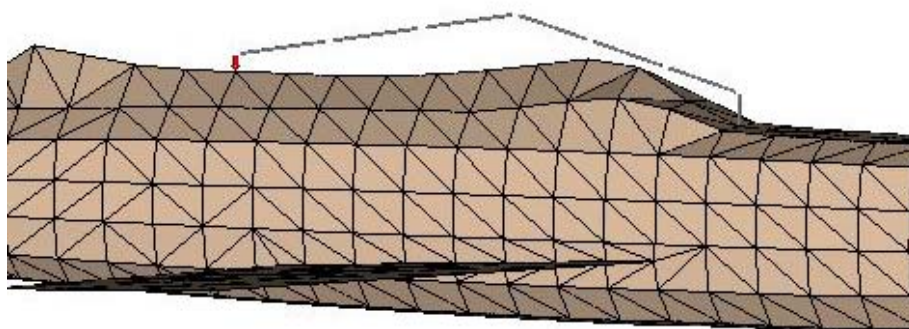
5.3.1 Modelled results

Figure 53   The Macchi model is driven by a large skin current probe working in reverse. The red arrow shows the feed location. The wire is shorted to the aircraft fuselage at the forward end. It might also be thought of as an HF antenna.

The modelled eigencurrents of the geometry shown in Figure 53 are shown in Figure 54. The dB scale is used because of the large range of values. Overall, the eigencurrent amplitudes display a great difference compared to the free-space plane-wave situations already described. The resonance of mode #571 is barely detectable, and the amplitudes are greatest at the lowest frequencies. The latter effect is a result of the inductive nature of the probe, and thus its vanishing impedance at DC. A further difference is that the inductive mode #541 is most strongly excited. This fits nicely with our understanding of the inductive nature of the injection geometry; the loop injection probe, because of its asymmetrical location and limited extent, is causing circulation of currents on the fuselage.

The loop injection approach is thus unlikely to be an efficient method of exciting the fundamental capacitive modes. The ability of this approach to principally excite particular inductive modes may prove useful in the future, by correcting over-excitation of inductive modes caused by the principal current injection topology. Or it might prove useful for providing a DCI simulation of vertically polarised EMEs, in which inductive modes predominate.
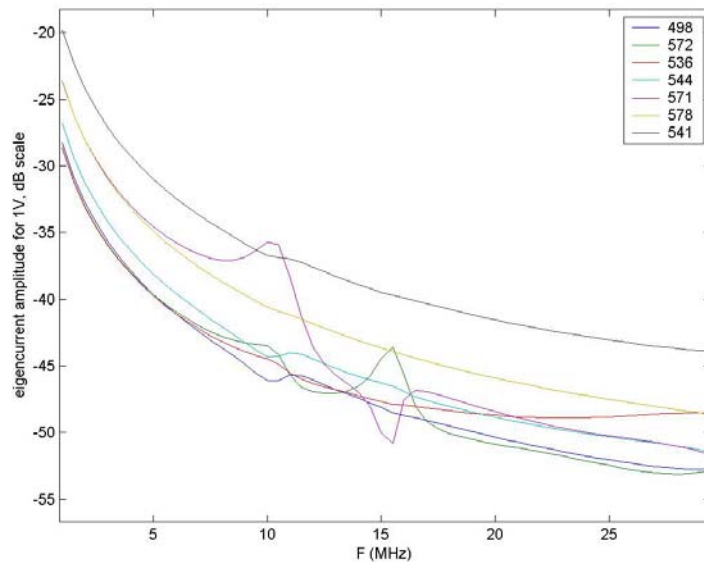
Figure 54   Eigencurrent amplitudes for the loop driven macchi model. Note the decline with frequency due to loop inductance of 6dB/octave and that the strongest excitation is of the inductive mode #541.

The loop excitation could be improved in efficiency by reducing the inductance of the return path in the loop. This could be accomplished by using sheet instead of wire. Taken to its logical conclusion, we would use a conducting ground plane as the return path of least inductance. The limiting inductance then becomes that of the aircraft itself and the connections between the aircraft and the ground plane. Furthermore, to increase the efficiency of excitation of the fundamental capacitive modes we would move the injection sites further apart and locate them closer to the axis of the aircraft. This brings us nicely to the design of the next injection method.

DSTO-RR-0329

5.4 Pyramidal coupling mechanisms above a planar PEC ground plane.

In this section, the external physical topology was inspired by an image from Nigel Carter's presentation to the author in October 2005. The research has been undertaken separately and the actual implementation may or may not be similar to those methods developed by Dr Carter.[19]

The present method uses metallic pyramidal structures, earthed to the ground plane and located at nose, tail and wingtips. The apices of the pyramids are conveniently close to the aircraft nose, tail, and wingtips, so that the inductance of the connecting conductor is as small as possible. For a Macchi aircraft, square-based pyramids of 60 degree included angle are used with a height of one metre. The pyramids may be thought of as providing a low inductance connection from the source or load to the ground plane, which acts as the return path. This method may also be seen as a logical extension of the loop method considered earlier, where the loop is replaced by a PEC ground plane and pyramids to reduce inductance, and the injection points are separated as much as possible.

The feed and loads may be considered, from an RF modelling perspective, to be located between the pyramid apices and the aircraft nose, tail, wingtip etc: If 50 ohms loads and source impedances are used, the actual physical loads and sources can be removed from the apex, and a 50 ohm coaxial cable outer conductor connected to the pyramid apex, and the coaxial inner connected to the conductor which contacts the aircraft skin. The coaxial cable may be neatly concealed within the pyramid and emerge at a feed-through at the pyramid base. This keeps the tapered, wide band form of the pyramid unobstructed. An important design principle is to keep the inductance of the apex connecting conductors as low as possible. This can be accomplished by minimising their length, using large diameter braids and using multiple braids. The use of flexible conductors, such as braid, is important, as the aircraft may move a significant amount on its undercarriage in high winds, causing fatigue to the conductors. The topology and details of the DCI setup are shown in Figure 55 and Figure 56.

The concept is to adopt several feed and load combinations, since a single combination can't adequately reproduce the free-space situations:
- Feed the nose and load the other three points;
- Feed the tail and load the other three points;
- Feed the starboard wingtip and load the other three points;
- Feed the port wingtip and load the other three points.

This gives the ability to separately target the fuselage capacitive eigencurrents, and each wing's eigencurrents. In a numerical simulation it would be possible, based on modelled linear relationships between the drive location input voltages and the eigencurrent magnitudes, to control the levels of the drive voltages simultaneously using the principle of superposition. In a practical test, this would require more complex and expensive equipment, including four power amplifiers of ~10 kW.

---

[19] Dr Carter did not have the time to discuss his calibration methods, which are based on multiple cable current measurements, and are not used here.
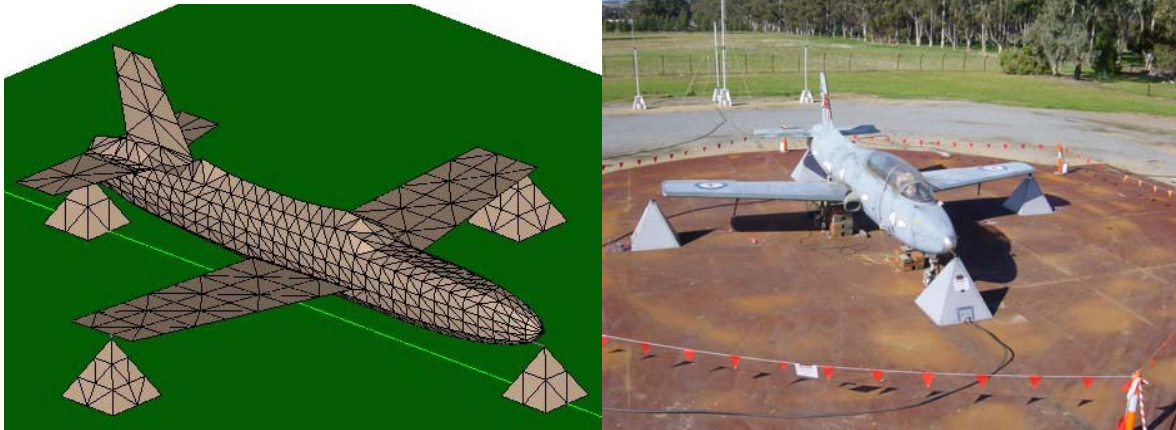
Figure 55   General topology of DCI using the pyramid method. Grounded pyramids are located at each aircraft extremity. Loads or sources are placed between the apices and the aircraft. In the experimental arrangement, the pyramids were constructed of galvanised 1.5 mm sheet steel and tack welded to the steel sheet ground plane.
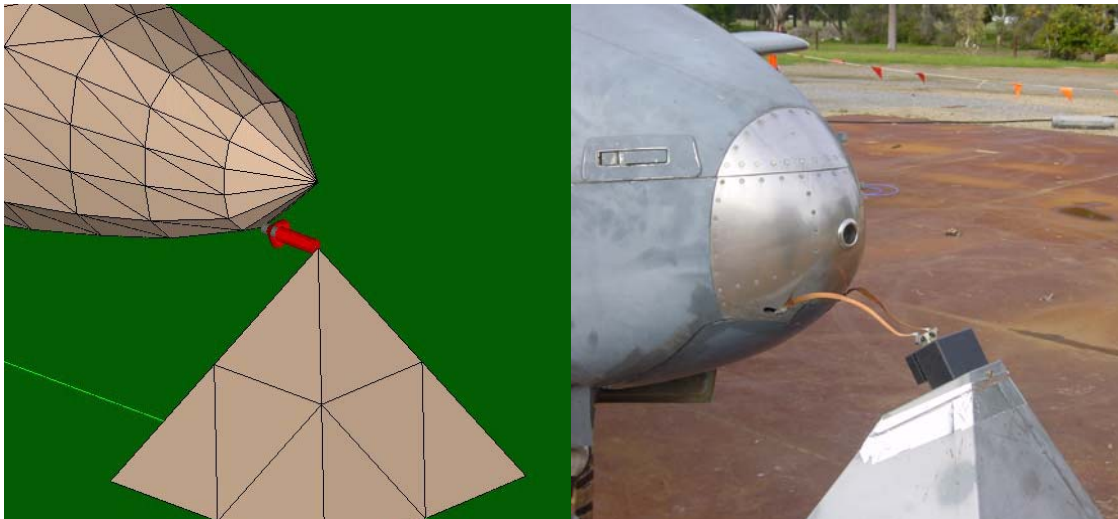
Figure 56   This figure shows the detail at the nose area. In this case a source is located between the nose and the apex of the pyramid, represented in the left figure by a red arrow. In the right figure, the inner conductor of a coaxial line is brought across to the aircraft nose by two heavy copper braids using bolted contacts. The coaxial outer conductor is earthed to the pyramid apex.
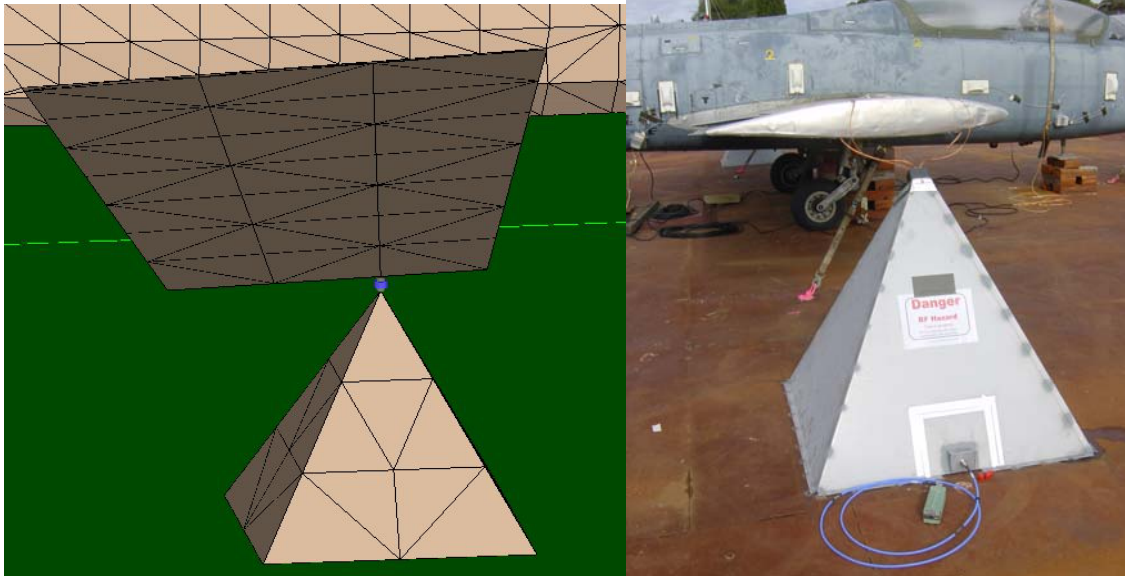
Figure 57 Detail showing proximity of pyramid apex to wingtip. In this case a load, represented by the blue cylinder, was placed on the wingtip. The right image shows how the situation was achieved in practice. The green object is a 50 W, 50 ohm RF load, which is coupled to the pyramid apex by coaxial line.

Figure 58 A detail of the sheet aluminium adapter bracket used to electrically connect from the pyramid at the tail to the aircraft jet pipe's existing screws and penetrations.

Figure 59 Details of the pyramid apex structure. On the left, the inside of the structure shows the N-connector with earthed outer connected to the sheet metal. On the right, the outside of the structure shows a nylon support block and terminal block connected to N-connector inner conductor.

5.4.1 Model Validation
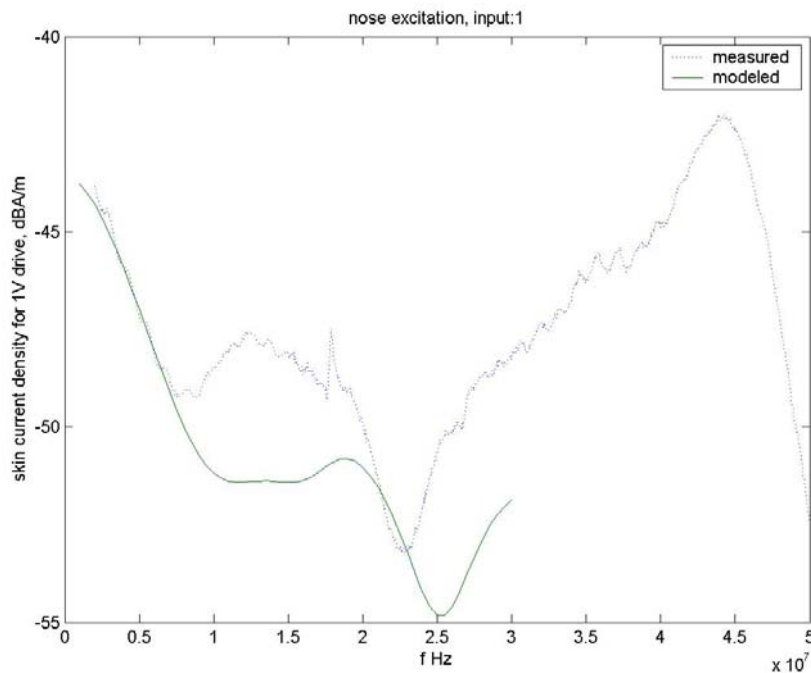
Figure 60 Comparison of skin current density for a point near the nose measuring axial current density is shown. In this case, the nose is the injection site, hence larger amplitudes are seen.

Complete data comparing the 14 current measurement points' amplitude and phase between model and measurement is contained in the attached CDROM and the files are described in Appendix C: Some representative results are shown below. In all cases, the skin currents are calibrated relative to a 1 V forward propagating coaxial line wave arriving at the injection site.[20]

---

[20] This reference to a forward propagating wave is important, and more fully explained in the appendix. It comes naturally out of the VNA calibration approach scattering parameters. However, for the model, the same was simulating by using a 2V constant voltage source in series with a 50 ohm load.

In Figure 60, the horizontal skin current density for the same point considered earlier – the port side of the nose – is shown. The injection site is also at the nose, with loads on the other three extremities. Agreement is better than 4 dB. In Figure 61, the same location is shown, this time for the injection site moved to the tail. Agreement is excellent with about 1 dB separating measurement and the numerical model.
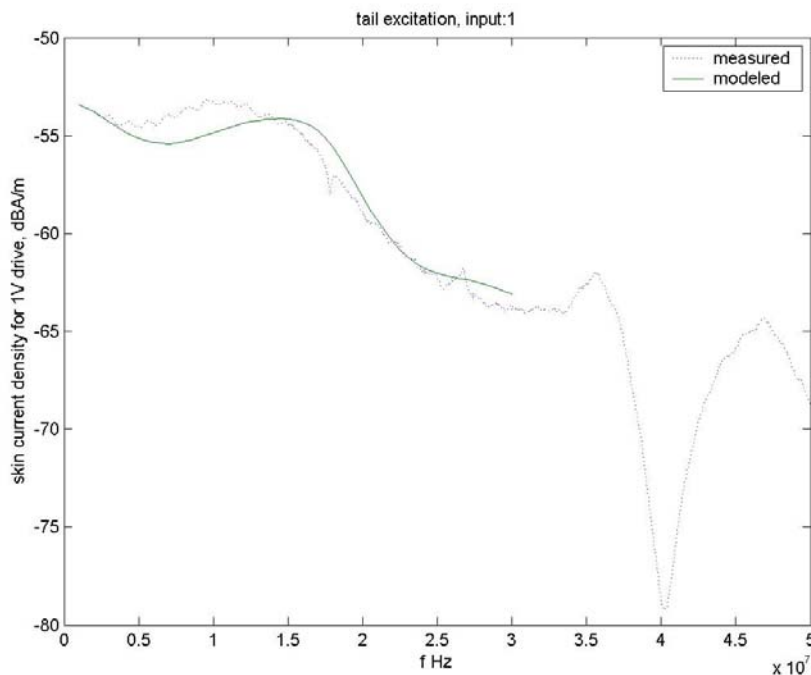
Figure 61   Comparison of skin current for a point near the nose, but with the source applied to the tail, and with loads on the other three points. The agreement is extremely close.

This has the same appearance to the load as a coaxial line with the 1 V forward wave. In both cases the voltage applied to the load will vary depending on its impedance and the reflected wave amplitude. Thus if Z_L=infinity, the voltage applied would be 2 V in both cases. For a matched load the voltage applied is 1 V in both cases.

5.4.2 Eigencurrent amplitude.
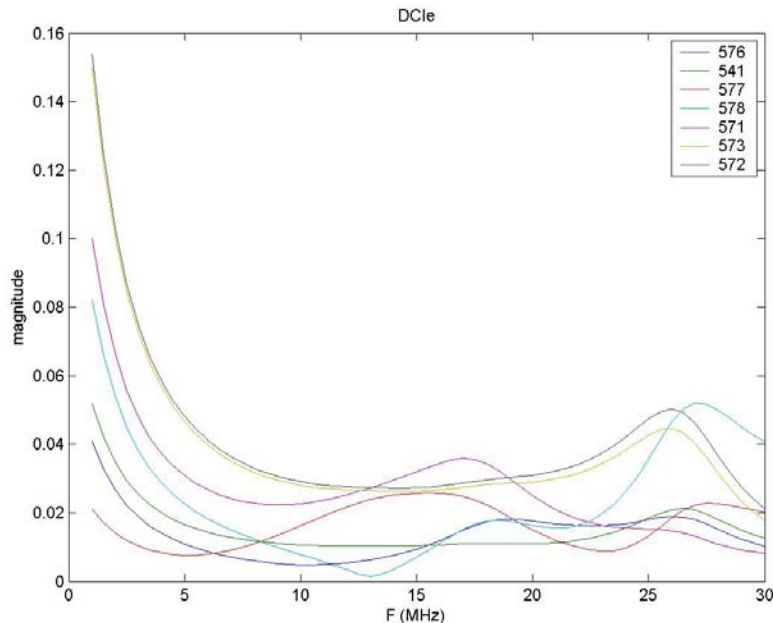
Figure 62   Eigencurrent amplitudes of the Macchi model when exposed to DCI at the nose and 50 ohm loads at the tail and wing tips.

In Figure 62, the amplitudes are shown for the eigencurrents with a 1V source applied at the nose, and 50 ohm loads applied at wingtips and tail. At the lowest frequencies, there is a high current, where effectively circuit theory currents are flowing limited by the three parallel 50 ohm resistances and low inductive reactance. This plateaus at eigencurrent amplitudes of approximately 0.02-0.04 above 6 MHz. If we were to base calibration on the 1 V/m horizontal polarised plane wave situations, we would need to raise the mode #571 to 0.65 at the 12 MHz resonance. This alone would require a 20 V source. To increase by the additional 200 fold factor for MIL-STD-464A, would require 4000 V drive to the nose of the aircraft. This corresponds to 53 kW drive power. Note this only applies at 12 MHz: away from the resonance, power requirements are typically 10 dB less. This suggests that an alternative coupling method might be used for the 12 MHZ resonance based on more efficient coupling. More exact estimation of the required power is given later.

However, one may ask, can the site to which the power is applied be improved for the purpose of preferentially and efficiently exciting the #571 mode on the fuselage? To answer this question, consideration should be given to the form of the #571 mode, shown in Figure 2 and Figure 3: The current flows from the aft fuselage towards the nose and towards the wing tips. In other words, the current flow has the same, let us say positive, sign in a radial sense on the wings and forward fuselage. The radial direction of current on the aft fuselage is opposite, however; let us say negative in sign. Thus, considering a circuit theory understanding, if we apply the source at the nose and loads to the wing tips, the relative phases of wing and forward fuselage currents will be wrong for mode #571. Co-phased wing modes #572 and #573 will be required to fit the resulting distribution. This will reduce the energy available for the #571 mode. If however, we apply the source to the tail, and loads to wings and nose, then, using the circuit theory understanding, the relative directions of current on wings and forward fuselage should be correct for the mode #571. This was modelled and is shown in

Figure 63. The above reasoning is confirmed by the modelling, with the mode #571 more efficiently excited by approximately 6dB, and no significant excitation of the wing modes being seen. Thus the 53 kW figure required for fuselage resonance from the nose driven topology would reduce to approximately 13 kW. Other benefits of this drive method are a reduced excitation of the higher-order fuselage capacitive modes, #577 and #578 relative to the nose driven method. This illustrates an important benefit of approaching DCI from the point of view of skin currents, and particularly from the point of view of eigencurrents. To achieve equivalence to vertical polarised free-space field levels of 200 V/m, as practiced at Patuxent River, about 20 dB less power would be required, thus only 100-150 W. However this would only apply to the #571 mode. Note that for horizontal polarisation the dominant eigencurrents are the inductive types. Proper fidelity would require the main inductive modes be controlled for.
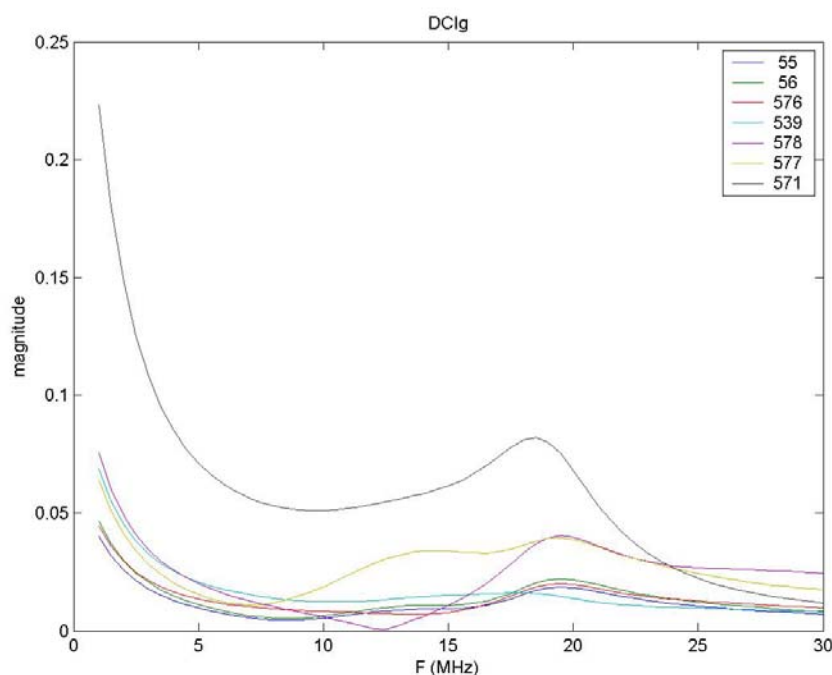
Figure 63   The source is applied at the tail and loads at the wingtips and nose to achieve a purer excitation of mode #571, than if the source is applied at the nose
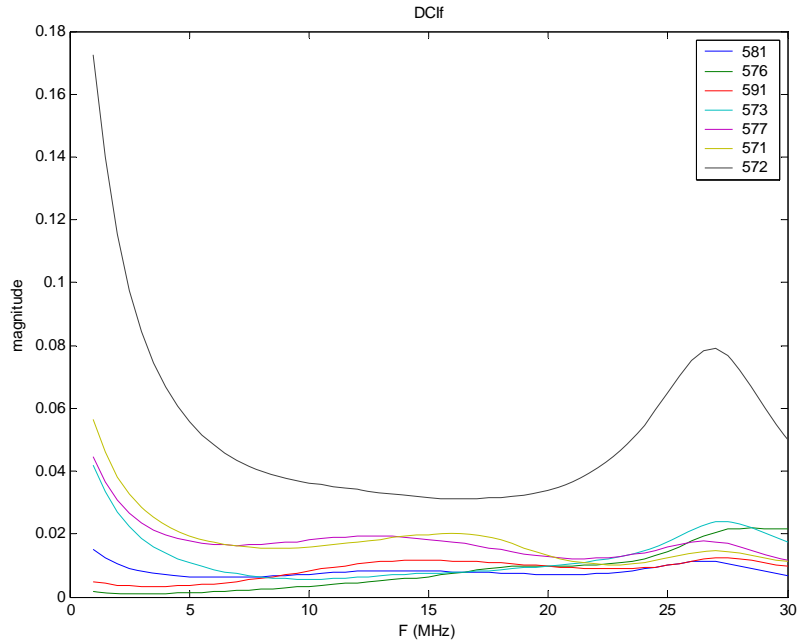
Figure 64   Eigencurrent amplitudes of the Macchi model when exposed to DCI excitation at the starboard wingtip and 50 ohm loads at nose, tail and other wingtip. The starboard wing mode is preferentially excited.

In Figure 64, the effect of applying the 1 V source at the starboard wingtip is shown. This is shown to strongly excite the starboard wing mode, #572. The amplitude is about 0.04 at the lowest, central region. Suppose we wish to control the source power to excite the #572 mode equivalent to its level when the free-space electric field of 200 V/m is parallel to the pitch axis (wings). From Figure 26 or Figure 28, the maximum amplitude required for 1 V/m may be seen to be ~0.27. Thus to achieve equivalence to 200 V/m would require a maximum of 0.27/0.04 x 200=1350 V applied at the wingtip. At 16 MHz, the input impedance is approximately 100 ohms real. Thus the required power for the wing resonance is 9 kW.

6. Bundle current comparison – DCI versus LLSC

This section is the most important of this report in that it seeks to validate the proposed DCI method against LLSC.

It is commonly accepted that the mechanism of introduction of EMI into avionics at HF is via the cable currents. Thus the fundamental criteria to compare between the two methods are the currents coupled to the cable bundles. It is irrelevant, of course, whether the cables occur in bundles or individually, or whether they are powered or terminated, provided the same conditions apply in both cases. For the purposes of this comparison, the cables are merely conductors upon which currents are coupled and which are representative of the cable layout of aircraft of the Macchi's generation.

Thus, the vitally important question to be answered in this work is:
- Can the proposed DCI method achieve the same bundle currents as LLSC?

Before proceeding with the bundle current comparison, I propose to elaborate the reasons why I believe this is a better comparison than comparing system susceptibility data. If one accepts that cable currents are the only significant mechanism for induction of EMI into avionics at HF, and none dispute this axiom, then a system upset comparison is merely a poor measurement of cable current. It is a one-bit (fail-not fail), somewhat narrow band (susceptibility bandwidth), modulation dependent (susceptibility modulation dependence), and possibly history dependent, comparison of cable current at unknown locations on the cables associated with an avionics function. Of course a small number of genuine system upsets depend on synergistic effects, but DCI is expected to provide much better performance in this regard than BCI. Thus, this characteristic of real system upsets is an argument *against* using system upsets for validation of DCI, unless the comparison data is based on FFHP testing or something of similar standard. A further problem with using BCI generated system upsets is that of current distribution inaccuracy within the bundle. Unfortunately, very few full field test systems can reach 200 V/m with horizontal polarisation. Perhaps for these reasons, others [15] have used contrived system upsets as an ultimate basis for validation. However the fundamental issue remains that a system upset is a one-bit measurement of current, and hence is a poor experimental design.

While on the subject of validation benchmarks, the LLSC skin currents and hence cable currents are not exactly representative of free space currents due to ground plane effects, as mentioned earlier. Although the aim for DCI, like any method, is to achieve equivalence to free-space exposure to an EME, it is only practical to demonstrate equivalence to LLSC, as it is impractical to measure coupling factors in free-space. However, this is not an issue for the present comparison, as the modelled LLSC skin currents (i.e. for the Macchi above ground plane) were the calibration basis for the DCI, hence the bundle currents should still coincide.

Having considered the benchmarking issues, I now proceed to describe the validation carried out. In this section, the previous results of this report become essential inputs used to compare the proposed DCI approach to LLSC measured bundle currents. The three key elements are:
- Eigencurrent amplitude analysis
- A validated numerical model of the LLSC situation skin currents
- A validated numerical model of the pyramid based DCI skin currents

In addition, measurements of bundle currents excited by LLSC and DCI are introduced.

In all the following plots, the measured currents are normalised to 1 V/m. The normalisation of the measured LLSC currents is straightforward, though complicated due to the large number of contributing transfer functions which must be separately calibrated. However, the cable current clamps themselves have not been calibrated, as the object is to compare DCI with LLSC, and the current clamp transfer functions would be the same in both cases. Thus the transfer functions plotted have the units V/(V/m), rather than A/(V/m). The only disadvantage to this is that they are not directly comparable with other published coupling data.

In the case of the DCI measured bundle currents, a transfer function is arrived at, relating the signal from the current clamp to the signal arriving at the injection point. In order to adjust this to be equivalent to LLSC, it is multiplied by the frequency dependent ratio of the eigencurrent amplitudes:

$$I_m^{n,p,q}(f) = \frac{\alpha_n^{LLSC,p}(f)}{\alpha_n^{DCI,q}(f)} I_m^q(f)$$

Where $I_m^q(f)$ is the measured DCI transfer function for bundle m, injection point q, for a 1 V forward wave, and $\alpha_n^{LLSC,p}(f)$ is the amplitude of eigencurrent n in the LLSC, antenna p, situation for 1V/m axial field at aircraft centroid, $\alpha_n^{DCI,q}(f)$ is the amplitude of eigencurrent n in the DCI, injection point q, situation for a 1V forward propagating injection wave and $I_m^{n,p,q}(f)$ is the adjusted DCI measured bundle m current, which is the same as would be measured had the DCI injection voltage been adjusted by calibrating for eigencurrent n equivalence:

$$V_m^{n,p,q}(f) = \frac{\alpha_n^{LLSC,p}(f)}{\alpha_n^{DCI,q}(f)},$$

which is what would be done in an actual test, if DCI equivalence to 1 V/m LLSC was the aim.

The concept proposed, is to concentrate on the three dominant capacitive eigencurrents: The fuselage mode #571, and the two symmetric wing modes #572 and #573. The method is to, in turn:

- Place the injection point at the tail, and control using n=571.
- Place the injection point on the starboard wing, and control using n=572
- Place the injection point on the port wing and control using n=573.

Thus, although the equations allow independence of injection point and eigencurrent, particular eigencurrents, n, are linked with particular injection points, q, that modelling has shown are well coupled.

Furthermore, the antennas used in the LLSC situation are also related to the eigencurrent most strongly excited. For example, modelling shows that the #571 eigencurrent is mainly excited by a horizontal polarised antenna to either side of the aircraft. The wing eigencurrents #572 and #573 are mainly excited by horizontally polarised antennas in front or behind the aircraft, but are also excited by a horizontally polarised antenna on either side. There is now also a linkage between p and q and n. Only a very sparse portion of the p, q, n space is thus considered.

Ten bundle sites were measured, as shown in Table 3.

Table 3 Cable bundle current locations

Input number	Loom number	Location description
1	RD6P	AC22 Forward beneath cockpit
2	X45P	AC22 Forward beneath cockpit
3	31P	AC22 Forward beneath cockpit
5	4-11P	AC54 Aft beneath cockpit
6	P-17S	AC54 Aft beneath cockpit
7	RU32P	AC54 Aft beneath cockpit
9	F16-S	AC79 Top behind cockpit
10	P-11	AC79 Top behind cockpit
11	P-12	AC79 Top behind cockpit
13	coax	AC44 Tail beneath jet pipe.

Figure 65 Current clamp locations for inputs 5, 6, and 7. It is behind access hatch AC54, on the starboard side beneath the cockpit.

In all the comparison plots, the bundle current plots were computed as follows:

- Red line: This is the **maximum** of two DCI computations of coupling. **Tail injection** is controlled using the #571 eigencurrent and related to a LLSC model with side horizontal antenna. **Wing injection** is controlled using the #572 eigencurrent and is also related to a LLSC model with side horizontal antenna. The maximum of both adjusted currents are then taken.
- Blue lines: There are 8 blue lines recording the measured LLSC cable bundle couplings with the eight different antenna positions and polarisations.

The DCI current was also controlled using #572 eigencurrent and related to a horizontally polarised free space field incident from the front, as per Figure 26, section 3.1. However the bundle current levels achieved were less than those achieved using the method generating the red lines, and so are not plotted in most of the figures for improved figure clarity. Furthermore, the method of the red line was adopted but using side incident free space horizontally polarised waves. As would be expected this resulted in a reduction in the Q of the resonances and less over-test relative to LLSC bundle currents at resonances.

The DCI bundle currents are compared with the LLSC measurements for the ten bundle locations in Figure 67 to Figure 76.

Figure 66   Current clamp location for input 13. It is beneath the jet pipe
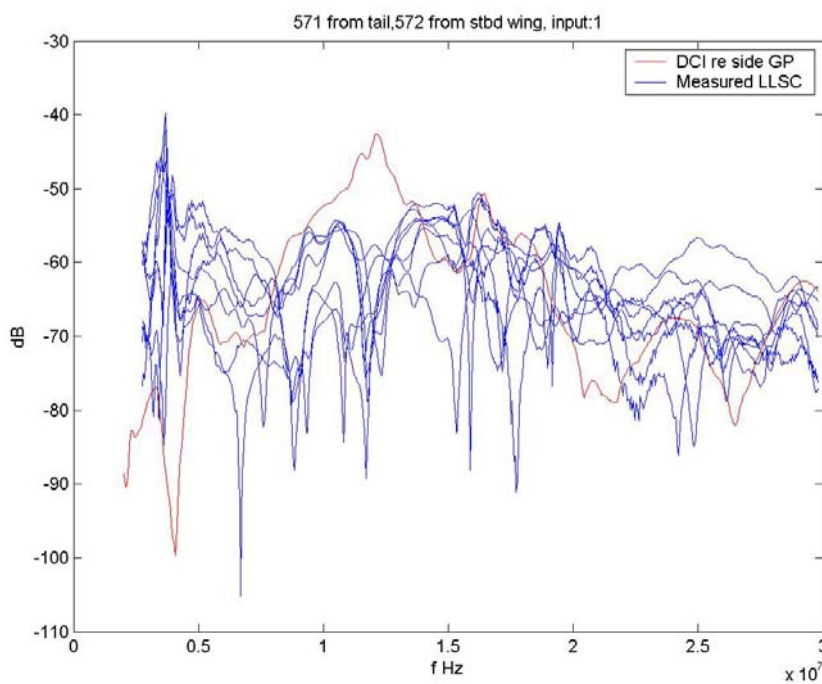
Figure 67   For bundle 1, the DCI currents are over-tested by 15 dB at fuselage resonance and under-tested 12 dB at 4 MHz and 20-25 MHz
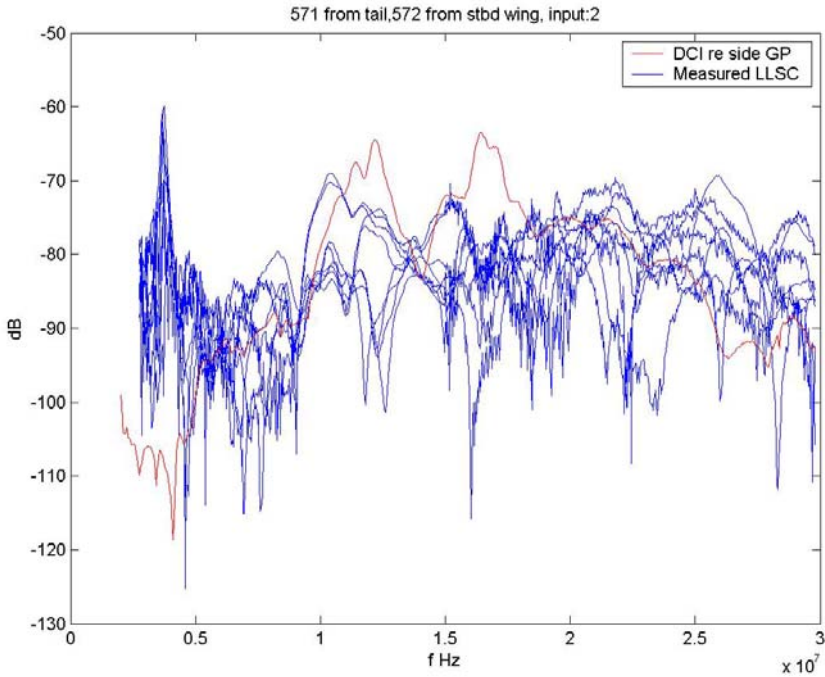
Figure 68 Using DCI, bundle 2 is over-tested at both resonances by 10 dB. Below 7 MHz, LLSC currents appear to be noise dominated. The DCI bundle is under-tested above 25 MHz by 15-20 dB.
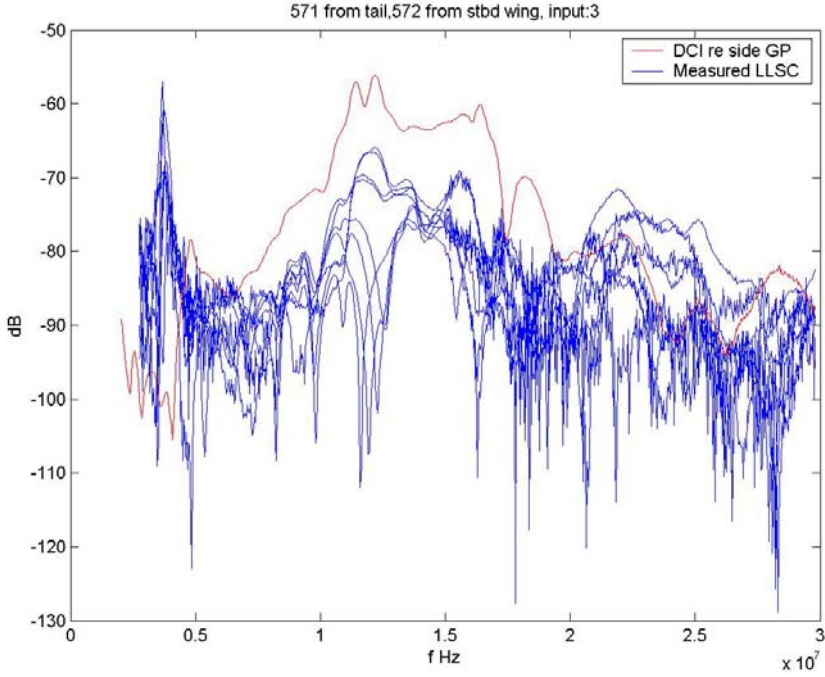
Figure 69 Using DCI, bundle 3 is over-tested 10 dBfrom 7 MHz-20 MHz, and under-tested 10 dB at 25 MHz
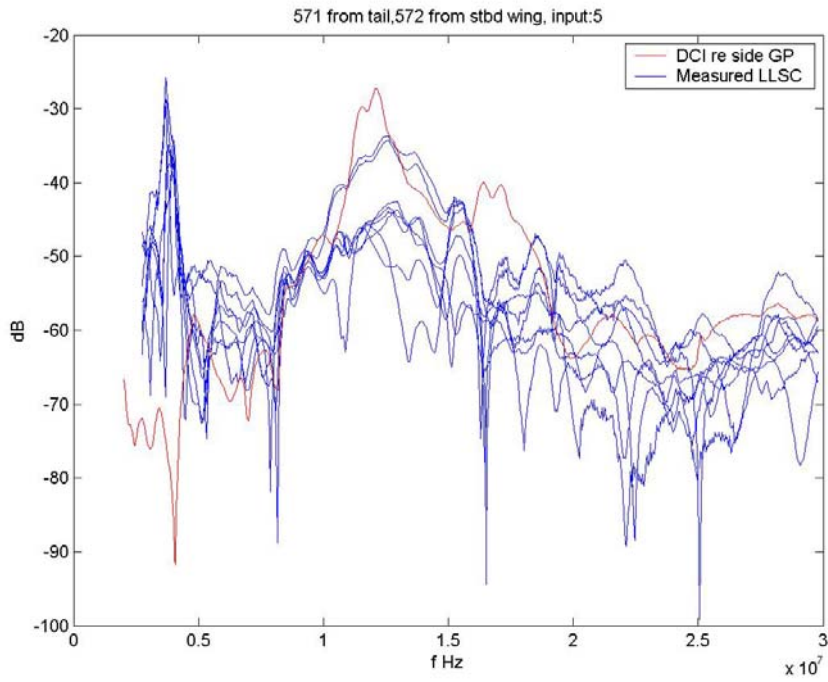
Figure 70 Bundle 5: This is a thick bundle (4-11P) with numerous origins. The DCI bundle is well tested over the whole range with errors of <10 dB.
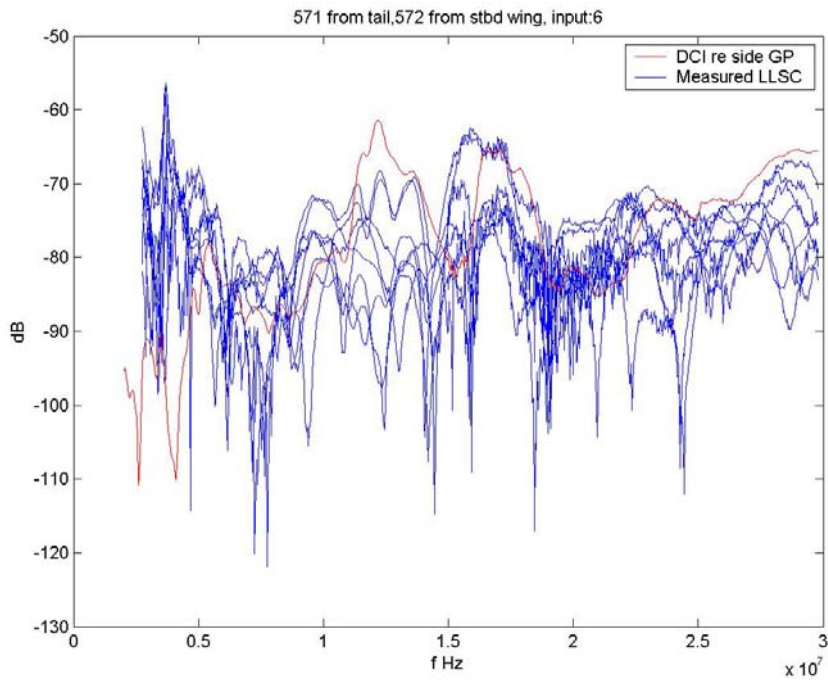
Figure 71 Using DCI, bundle 6 is well tested over the frequency range, with errors of <10 dB
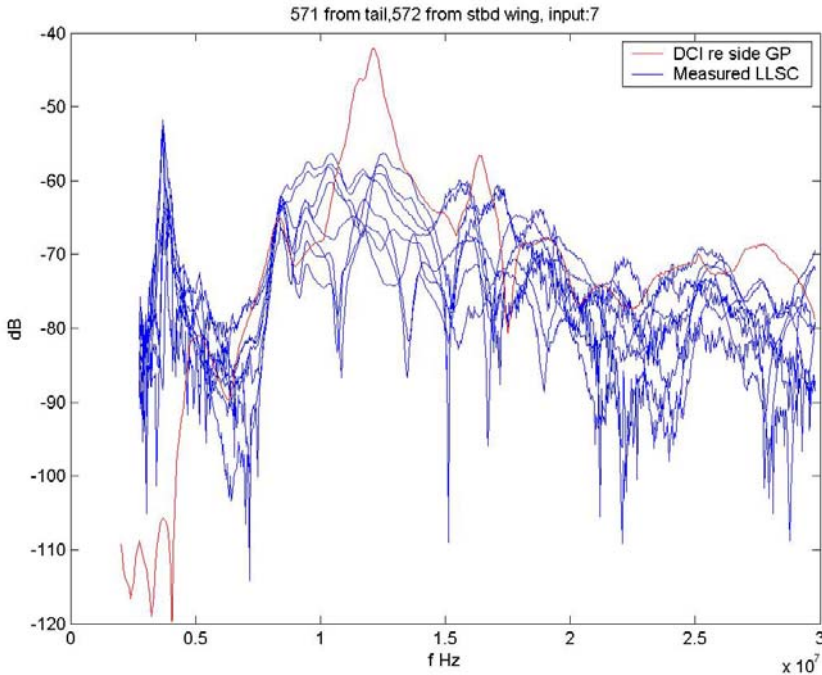
Figure 72   Using DCI, bundle 7 is well tested over most of the range but is over-tested 15 dB at fuselage resonance, (12 MHz)
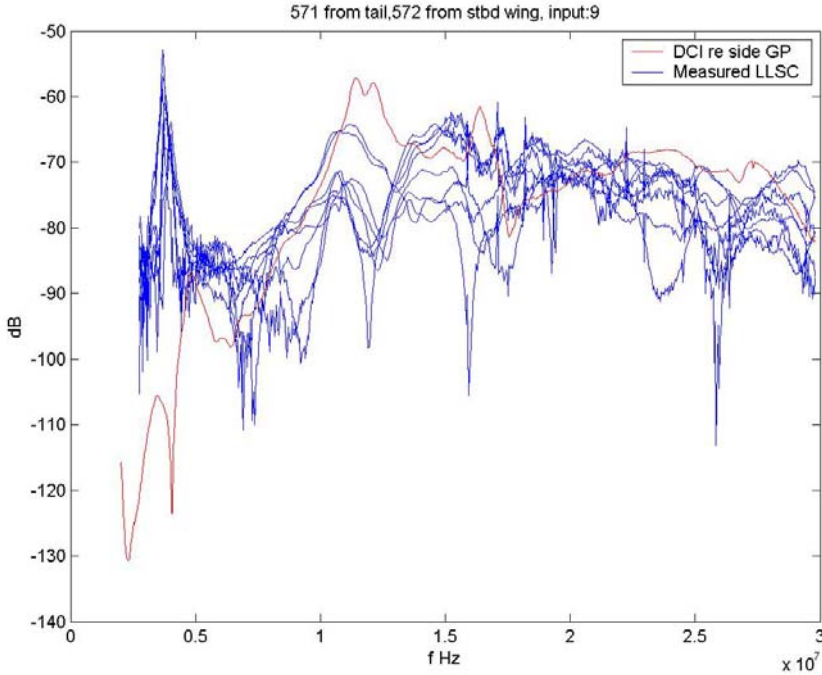
Figure 73   Using DCI, bundle 9 current agrees well with the LLSC measured currents
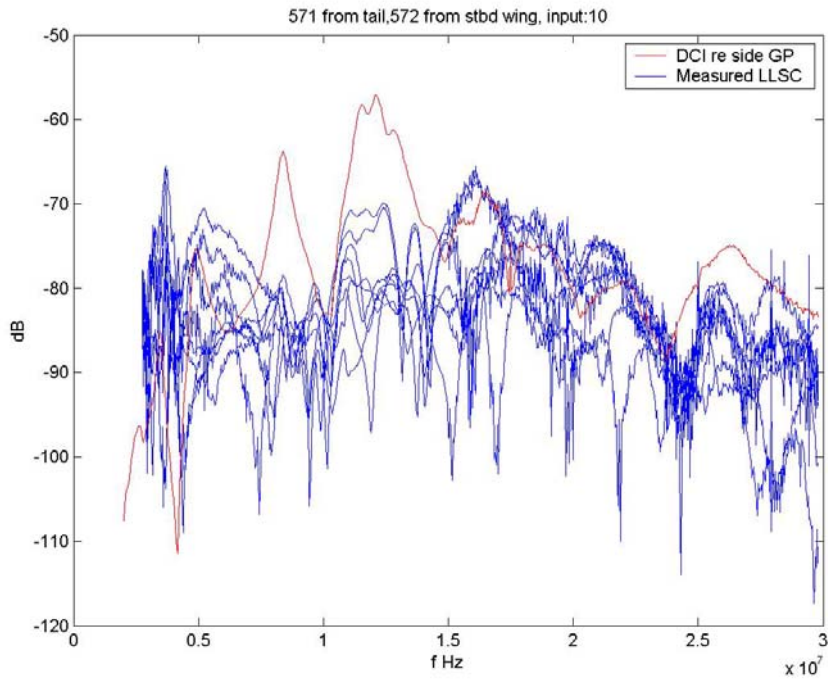
Figure 74 Using DCI, bundle 10 is over-tested at both wing and fuselage resonances. Elsewhere the agreement is good.
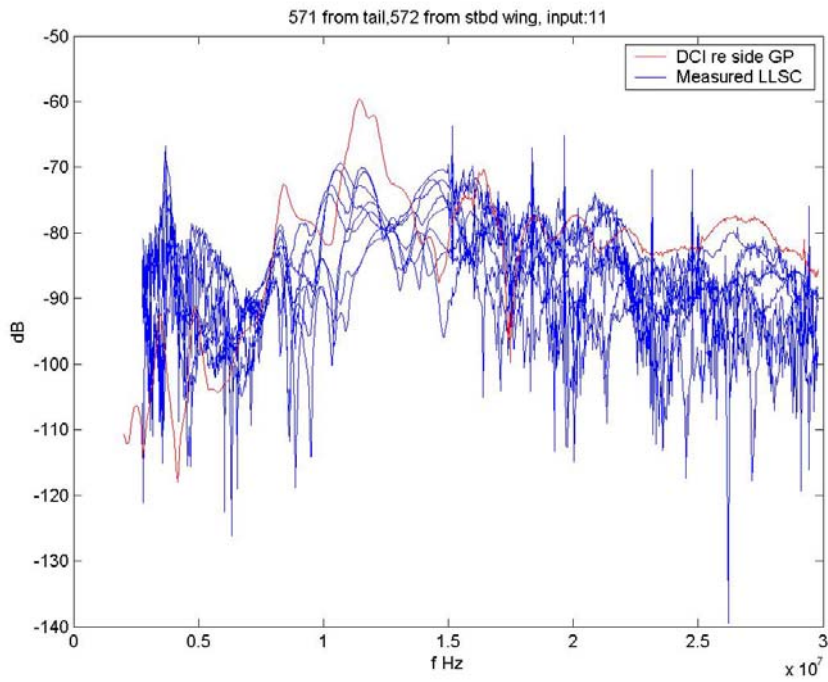
Figure 75 Using DCI, bundle 11 current agrees well with the LSC current maximum except for an overtest at fuselage resonance.
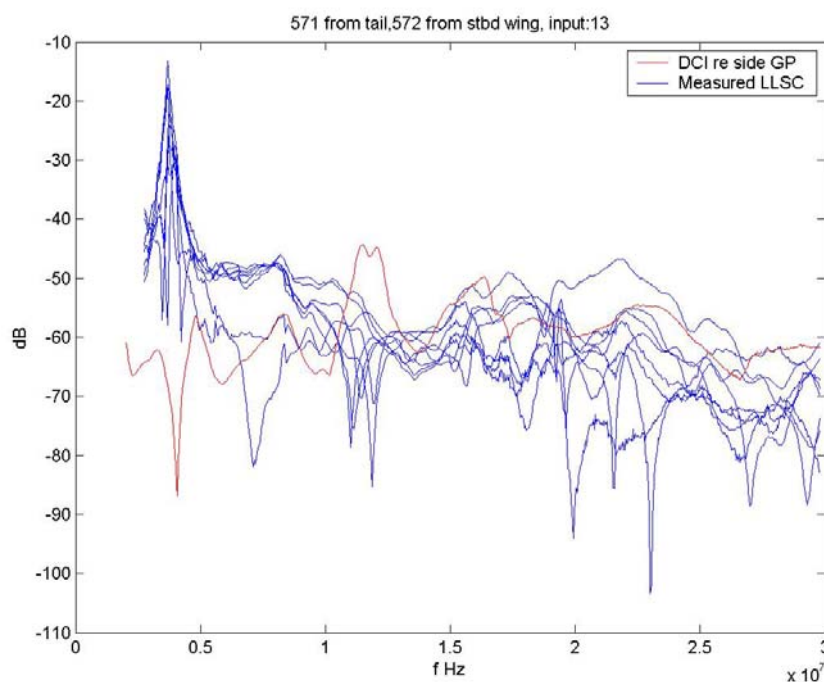
Figure 76   Using DCI, bundle 13 agrees with LLSC maximums within 10 dB over most of the band.

The following comments and conclusions may be drawn from the bundle current comparisons:

- F<5 MHz: In most cases, LLSC measurements are noise dominated below 5 MHz. The noise is then increased by the inverse of the calibration field, which is very small at low frequencies. The agreement or disagreement in this range is not considered significant.
- 5 MHz<F<10 MHz: In most cases, the LLSC measurements exceed the DCI measurements below fuselage resonance by up to 10 dB. This is consistent with the 10 dB lower level of modelled LLSC skin currents relative to measured LLSC skin currents in this frequency range, as was seen in the validation of the LLSC model. This is thus due to the LLSC modelling, rather than being a fault of DCI or the proposed eigencurrent method of calibration.
- 10 MHz<F<20 MHz: In all cases, the DCI bundles were overexcited at aircraft fuselage and wing resonances (12 MHz and 16 MHz) by the order of 10-15 dB. This is consistent with the excessive Q seen in the LLSC model, relative to measurements of LLSC skin currents. Once again, this is thus due to the LLSC modelling, rather than being a fault of DCI or the proposed eigencurrent method of calibration. In a routine, rather than experimental, aircraft test, the free space eigencurrent levels would be used to control the DCI injection voltages. It is believed that these do not exhibit excessive resonance Q: Modelling away from a ground plane is generally easier, as radiative losses are more dominant relative to resistive loss. Resistive loss is difficult to capture into a model from the aircraft geometry and design documents, as it is a complicated product of aircraft materials, fastening, grounding methods and maintenance history.
- F>20 MHz: In most cases, above 16 MHz, the agreement between DCI and the maximum envelope of the LLSC measurements was very good. However for inputs

(cable bundles) 1, 2 and 3 the DCI was significantly below the required level in this range. The cause of this effect is not yet known. The cables concerned make short runs in the nose of the aircraft. This suggests that nose injection would more successfully target these. However, none of the eigencurrents are significantly better coupled to the nose injection sites than any other, whereas there is clear coupling between the tail location and #571 eigencurrent, and the wing locations and the respective #572, 573 eigencurrents. This makes selection of an appropriate controlling eigencurrent difficult for nose injection. If an inappropriate eigencurrent is selected, gross (20 dB) over or under testing results. A linear combination of eigencurrents might prove useful to target this area.

In general the agreement is as good as that seen in the system upsets of the PUMA helicopter in [15]. The worst case disagreement in [15] was 20 dB and typically disagreement was better than 10 dB. Bolsover et al. [7] speaks of an enviable 5-10 dB disagreement with LLSC, though they used a conformal return rig and a fighter aircraft that better approximates a uniform cylinder[21], and hence it could be easier to generate a travelling wave upon.

In LLSC-DCI work, using a single bundle-current-based calibration; it is obvious that one of the resulting bundle current comparisons must necessarily agree. The extent to which DCI and LLSC disagree is just a measure of the span of calibration factors available. However, in the present work, it is shown that a calibration based only upon skin currents can produce equally good agreement with LLSC bundle currents. This is the first time that skin current distribution has been demonstrated to be the fundamental driver in HF HIRF coupling to cable bundles.

In order to demonstrate better agreement between eigencurrent based DCI and LLSC bundle currents, the modelling of the LLSC situation needs to be improved. It is expected that this could reduce the 10 dB errors seen to better than 5 dB. To eliminate the remaining 5 dB, the unrealised potential of skin current distribution analysis must be tapped using better DCI topologies to give greater fidelity to LLSC, or any arbitrary, skin current distribution. This remains an elusive goal.

6.1 Power requirements.

In this section the computed, frequency dependent power requirements are given for the DCI that would be required to be employed on the tail and both wing tips to achieve the aircraft HIRF current excitation equivalent to 200 V/m horizontally polarised plane waves in free space.

---

21 Indeed supersonic aircraft are typically designed using a constant cross-sectional area rule for the fuselage for aerodynamic reasons. This is why the fuselage is typically much narrower where the wings are attached, as the wings and fuselage are considered together to maintain the uniform cross-sectional area, apparently.
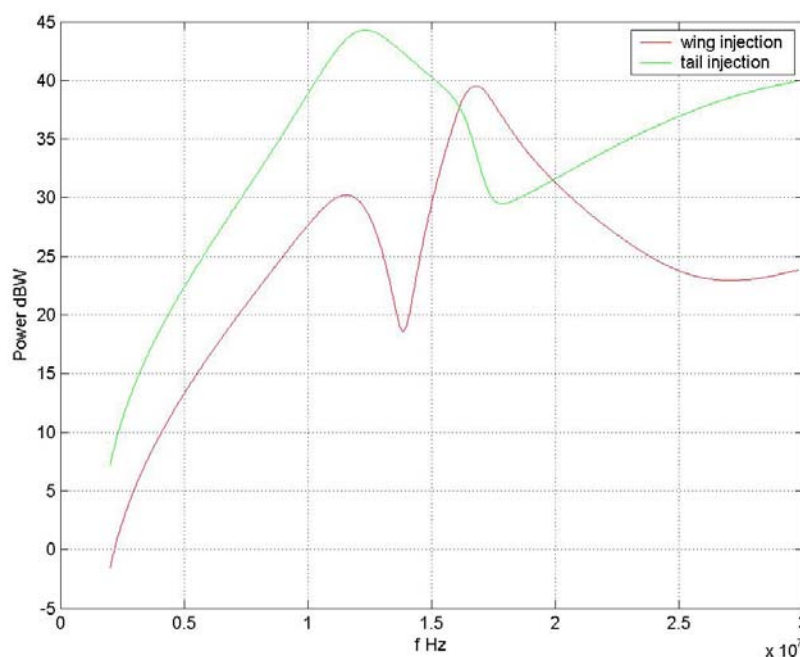
Figure 77   The DCI power levels required to achieve equivalence to 200 V/m horizontal polarisation for the Macchi. Both wing and tail injection sites are shown.

In Figure 77, the power levels are shown that would be required to achieve equivalence to 200 V/m horizontal polarisation for the Macchi, based on free-space eigencurrent levels. Both wing and tail injection sites are shown. It was estimated earlier by mental arithmetic, that the power level required to reproduce the fuselage resonance at 12 MHz is ~13 kW. This assumed perfect matching. In the Figure 77, a maximum of 20 kW (43 dBW) is required to achieve the same, but without tuning. Clearly, matching would be desirable when working in the fuselage resonance region to keep the power down to 13 kW. This compares favourably with the 50 kW found to be required for a similar test rig for the Jaguar to achieve equivalence to 200 V/m by A.M.Wellington of BAe [8]. As pointed out by Wellington, if 100 V/m is acceptable over the regions of the resonance, 6 dB less power is sufficient, and in excess of 200 V/m would still be available in other regions of the spectrum. As may be seen in Figure 77, 5 kW (37 dBW) is sufficient to achieve equivalence to 200 V/m everywhere except 10-16MHz for the Macchi without matching. A 10 kW amplifier with matching applied only in the resonance region could achieve equivalent test fields of 175 V/m. This may be compared with the 300 kW used at Patuxent river[1], which fails to achieve 200 V/m horizontal polarisation, but which does achieve 100 V/m vertical polarisation.

To achieve equivalence to vertical polarisation at 200 V/m, it is estimated that 20 dB less power is required[22] for the DCI method and hence only 200 W would be needed. This has not yet been validated however. A significant issue with achieving equivalence to vertical polarisation is that in this case the inductive modes dominate and these are not efficiently targeted with the injection locations considered here. Furthermore, no one inductive mode is greatly predominant. Thus all need to be simultaneously controlled to achieve a reasonably accurate skin current.

---

22 The eigencurrent amplitudes are <10% of those for horizontal polarisation.

7. Conclusions

In this work, phased skin current density samples were taken at 14 locations on a Macchi aircraft. These were used to validate LLSC and DCI numerical models of the Macchi aircraft. These numerical models were then subject to eigencurrent analysis – a method of reducing the complex skin current distributions to a small number of independent modal current distributions. Three of these modal current distributions were then used to control the amount of power applied to the DCI sites on the aircraft. The currents on cable bundles were finally compared using DCI controlled in this manner against LLSC.

It was found that for most cable bundles the DCI generated cable bundle currents equalled or exceeded the maximum envelope of the LLSC cable bundle currents taken over the 8 antenna polarisations and positions. In a small number of cases, over the range 20-30 MHz, the LLSC bundle current maximum envelope exceeded the DCI bundle currents by 15-20 dB. This matter requires further investigation, as a 20 dB safety margin is not practical given the powers already required. However, the typical difference seen between the LLSC maximum bundle current envelope and the DCI bundle current was of the order 6 dB. Most of this disagreement may be attributed to errors, also of the order 6 dB in the numerical model of the LLSC situation, which were propagated through the DCI calibration method through the use of the eigencurrents. It is believed that much of this error could be eliminated with an improved LLSC numerical model. In previous DCI work using a bundle-current-based calibration; it is obvious that, for example, one of the resulting bundle current comparisons, or their envelope, can be forced to agree. The extent to which bundle currents disagree is just a measure of the span of calibration factors available. However, in the present work, it is shown that a calibration based only upon skin currents can produce equally good agreement with LLSC bundle currents. Though hypothesized without much dispute among the HIRF community, this is the first time that skin current distribution has been demonstrated to be the fundamental driver in HF fields coupling to cable bundles.

The typical 6 dB error in this work is an acceptably small error, especially when compared with the errors which can occur with BCI due to multi-wire current distribution inaccuracy of the order 20 dB in some cases [3].[23] Hill [2] considered the problem of BCI multi-wire distribution inaccuracy in a simple situation that lent itself to analysis; Parallel terminated wires of equal length. In this situation differences of the order 10 dB were seen resulting from the bulk current approach. As stated by Hill: *"Further calculations of more complicated models including branching…could be performed. Such complexities would be expected to yield even greater differences between the two types of excitation."* The situation applying to an actual cable bundle in an aircraft may be imagined to be of very great complexity, with wires originating in different parts of the aircraft.

DCI has other inherent advantages over BCI including simultaneous stressing of redundant systems, speed of testing and effectively testing all cable bundles, rather than a select few.

---

23 In the section 4.11 Carter and Stevens write: "The currents induced at malfunction of the equipment during BCI tests can be typically an order of magnitude higher than those that would be produced by the radiated field." The comment relates to the situation where a low impedance grounding wire is included in a LLSC/BCI bundle and where that wire absorbs most of the BCI current. This is a special case of the problem of LLSC/BCI multi-wire bundle division of current. Hence it may be used as an estimate of the errors in whole aircraft BCI due to the multi-wire bundle division of currents error as being of the order of 20 dB.

A disadvantage of DCI is the high amplifier power required. This work concluded that 20 kW would be required for a planar ground plane test to achieve equivalence to the 200V/m horizontal polarisation full field situation. However 10 kW would provide 200 V/m over most of the HF range, and 175 V/m from 10 MHz-16 MHz. This may be compared with the 300 kW used at Patuxent River [1] for Full Field testing and powers of 200 W which are used for BCI: DCI requires approximately the geometric average of the two powers.

DCI testing equivalent to vertical polarisation, which would be representative of, for example, a helicopter approaching a 1 kW ship HF whip antenna, might be achieved with less than 200 W. However further work would be required to validate this assertion for the cable bundle currents. A significant concern is the need to control the inductive modes, which is not yet achieved. Thus far, only the fundamental capacitive modes have been controlled. Whole aircraft TEM cells are one potential means of simulating the vertical polarisation situation, and are a parallel stream of research at DSTO. It might be argued that an aircraft which passes the horizontal polarisation test, which is 20 dB harsher, would necessarily also pass the vertical polarisation test. However if susceptibilities were apparent in a horizontal polarisation DCI test, there is no clear way of analytically adapting the tested susceptibility field levels for the vertical polarisation situation. The only reliable way of discovering the vertically polarised susceptibility thresholds is through a vertically polarised test.

Even the original developers of BCI now make the point that the use of BCI at aircraft level will become increasingly difficult [3]. DCI has the potential to replace aircraft level BCI, while also solving many of the longstanding problems of BCI. However the question of how much power to apply, and where to apply it, as a function of frequency is much more complex to answer for DCI than BCI. Previous control methods for DCI have predominantly been based on the cable bundle measurements themselves. Other methods have been proposed based upon skin current measurements, but these have had the difficulty of choosing which location to use for calibration. The calibration method described in this work uses an averaged skin current distribution, rather than being based on a particular calibration site, and is hence less subject to errors due to arbitrary site choice. It does, however, require the use of several numerical models.

The DCI topologies used in this report were by no means exhaustive. Better agreement with LLSC bundle currents could be achieved using the unrealised potential of skin eigencurrent analysis. Better DCI topologies might give greater fidelity to LLSC, or any arbitrary, skin current distribution. This remains an elusive goal.

Perhaps the most challenging task is to gain test community consensus for standardised DCI techniques and then finally to persuade authorities to accept such techniques. A significant issue is the typical authority requirement that new test methods must demonstrate equivalence to old methods in terms of system upset thresholds. We must be alert to the fact that DCI may be significantly better then BCI in many regards. Thus, if system upset data is used for DCI method validation it needs to be derived from a recent test using an accurate method such as Full Field Horizontal Polarisation testing, which is done at very few, if any, sites to 200 V/m.

It is hoped that this work provides a small step along the path to such long term goals.

8. Acknowledgements

The author wishes to acknowledge the support of the work program reported here by the RAAF, through the Systems Certification and Integrity staff at DGTA.

The author is also indebted to the staff of the Electromagnetic Environmental Effects group at DSTO for their assistance with the conduct of the measurements described and for their unique insights and discussions during the work. Mr Craig Denton, Mr Stuart Thomson, Dr Andrew Walters and Mr Kevin Goldsmith were of particular assistance.

Mr Mark Bolsover provided a most valuable contribution by independently reviewing the draft document and suggesting improvements. Some of his comments on the subject of BCI, provided in the course of the review, are included in Appendix D.

9. References

[1]   F. W. Heather, "Development of a HF broadcast simulator for whole aircraft testing," presented at IEEE International Symposium on Electromagnetic Compatibility, Montreal, 2001.

[2]   D. A. Hill, "Currents induced on multiconductor transmission lines by radiation and injection," *IEEE Transactions on Electromagnetic Compatibility*, vol. 34, pp. 445-450, 1992.

[3]   N. J. Carter and E. G. Stevens, "Bulk Current Injection(BCI): Its Past, Its Present and Future (?) in Aerospace," presented at IEE Coloquium on EMC Testing for Conducted Mechanisms, 1996.

[4]   G. Spadacini and S. A. Pignari, "A bulk current injection test conforming to statistical properties of radiation-induced effects," *Electromagnetic Compatibility, IEEE Transactions on*, vol. 46, pp. 446-458, 2004.

[5]   O. Hartal, "Limitations of bulk current injection tests," presented at International Conference on Electromagnetic Interference and Compatibility, Madras, 1995.

[6]   S. Pignari and F. G. Canavero, "On the equivalence between radiation and injection in BCI testing," presented at International Symposium on Electromagnetic Compatibility, Beijing, 1997.

[7]   M. R. Bolsover, I. R. Foulkes, and I. P. MacDiarmid, "Airframe Current Injection as Part of Airframe Clearance," presented at EMC1992, Eighth International Conference on EMC, 1992.

[8]   A. M. Wellington, "Direct current injection as a method of simulating high intensity radiated fields (HIRF)," presented at IEE Coloquium on EMC Testing for Conducted Mechanisms, 1996.

[9]   N. J. Carter, "Aircraft EMC, The Past, The Present and The Future: An Overview," presented at IEE Coloquium on EMC in Aircraft, 1996.

[10]   D. McQuilton, J. M. Oakley, and C. Budd, "A computational assessment of direct and indirect current injection techniques for missile EMC testing," presented at 9th International Conference on Electromagnetic Compatibility, 1994.

[11]   A. J. Walters and C. Leat, "TEM cells for whole aircraft EMV testing," presented at International Symposium on Electromagnetic Compatibility, Chicago, 2005.

[12]   C. J. Leat, "Understanding skin current distributions on an aircraft at HF using eigencurrent expansions," presented at International Symposium on Electromagnetic Compatibility, Chicago, 2005.

[13]   N. J. Carter and P. E. Willis, "EMC Testing of High Integrity Digital Systems in Aircraft," presented at IEE coloquium on EMC in High Integrity Digital Systems in Aircraft, 1991.

[14]   S. M. Rao, D. R. Wilton, and A. W. Glisson, "Electromagnetic Scattering by Surfaces of Arbitrary Shape," *IEEE Transactions on Antennas and Propagation*, vol. Ap-30, pp. 409-418, 1982.

[15]   G. D. M. Barber, "The use of direct current injection (DCI) techniques for aircraft clearance," presented at 10th International Conference on Electromagnetic Compatibility, Coventry, 1997.

[16]   M. R. Bolsover, "Review comments on "HIRF Testing of Aircraft using DCI"," C. Leat, Ed., 2007.

This page intentionally left blank

Appendix A: OATS Skin Current Test Plan

A.1.   Introduction

The frequency range is 2-50 MHz. The source of signal to the power amplifier is the VNA in all cases. The VNA will be set for 201 points = 240 kHz frequency steps.

A.2.   Layout of skin current probes

There will be 14 skin current probes located as shown in Figure 78 and Figure 79.
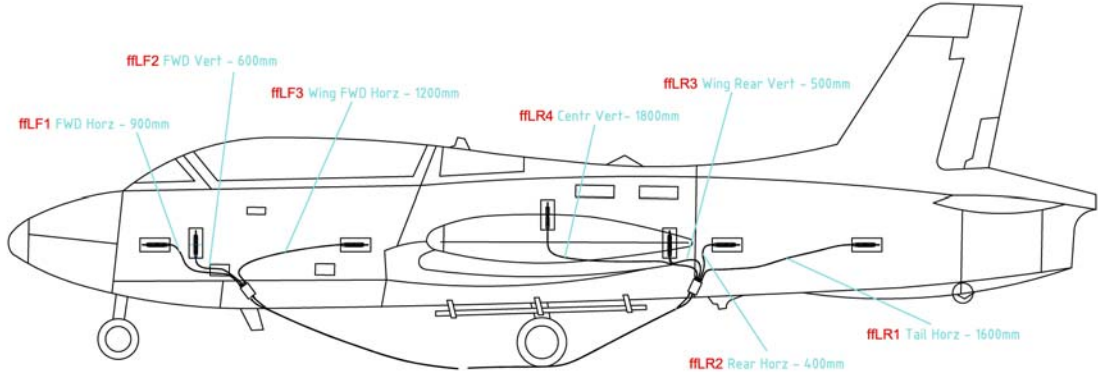

Figure 78 Port side of Macchi showing skin current probe flexi-form cable labels
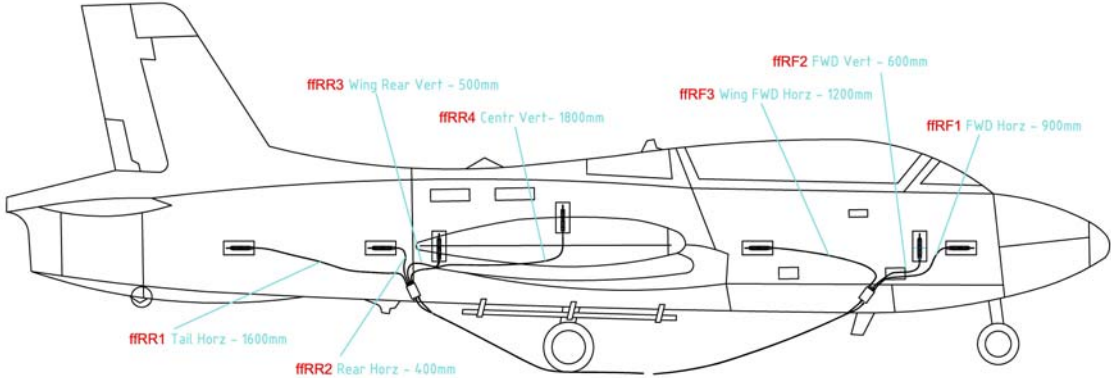

Figure 79 Starboard side of Macchi showing skin current probe flexi-form cable labels

A.3. Naming scheme of F-O cables, F-O boxes, flexi-form cables, and J-dot probes.

Table 4 'flexiform' cable names and lengths

Cable name	Cable length (m)	FOL Box and FOL Box input number		Skin current probe
ffLF1	0.9	LF (1)	1[24]	LF1
ffLF2	0.6	LF	2	LF2
ffLF3	1.2	LF	3	LF3
ffLR1	1.6	LR (2)	1	LR1
ffLR2	0.4	LR	2	LR2
ffLR3	0.5	LR	3	LR3
ffLR4	1.8	LR	4	LR4
ffRF1	0.9	RF (3)	1	RF1
ffRF2	0.6	RF	2	RF2
ffRF3	1.2	RF	3	RF3
ffRR1	1.6	RR (4)	1	RR1
ffRR2	0.4	RR	2	RR2
ffRR3	0.5	RR	3	RR3
ffRR4	1.8	RR	4	RR4

Four fibre optic cables are required in the tunnel, the names being cuLF, cuLR, cuRF, cuRR ("cable underground Left Front" etc.)

Four Fibre optic extension cables are required to go from the pit termination to the F-O boxes, the names being ceLF, ceLR, ceRF, ceRR. ("cable extension Left Front" etc.)

Four, four channel, fibre optic boxes (OAM02S) will be used labelled bLF, bLR, bRF, bRR, and each box input will have the channel names bLF1, bLF2, bLF3 etc. Boxes LF and RF will require only 3 operational channels. Each box and channel number will be marked.

Fourteen flexi-form cables will be labelled as shown in Table 4. The cable lengths shall be as shown in Table 4. Each cable will be suitably marked with its number.

In operation, the combination of cables and boxes will always be, for example cuLF – ceLF – bLF; and bLF1-ffLF1, bLF2-ffLF2, bLF3-ffLF3 and similarly for the other fibre-optic line and box combinations.

A.4. Calibration of VNA

Instead of calibrating the VNA each day using its internal calibration procedure, at the beginning of each day's work, a software run will be taken using a coaxial cable of short length, reserved for this use to connect the VNA ports. This cable will be marked specifically for this purpose. The cable includes a 6dB attenuator to prevent the software infinitely looping due to a possible small exceedance of 0dB due to VNA miscalibration. In practice, the cable without attenuator measured a transfer function of between -0.03 dB and +0.02 dB, which necessitated the use of the 6 dB attenuator (although 0.1dB would have sufficed).

---

24 If box inputs are already labelled use existing markings. The non-functional channel of one box may require one of these box input numbers to be changed.

A.5.   Calibration of F-O links and coaxial

In all of the remotely controlled calibration measurements, the same Labview software is used as for the experiments. This has the advantage of checking the operation of the Labview software and reducing the possibility of errors. In effect, because some propagation paths are changed or prevented by the calibration setups, some useless data is recorded by this method along with the desired calibration data, but the cost of disc space and RF instrument time of milliseconds is very cheap compared to programming time and error tracking.

In the Figure 80 below, the first calibration setup is diagrammatically shown. This calibration measures the propagation loss and phase delay through the 14 channels from skin probe output to VNA port 1 input. This includes several pieces of coaxial, two coaxial switches and the fibre optic links.
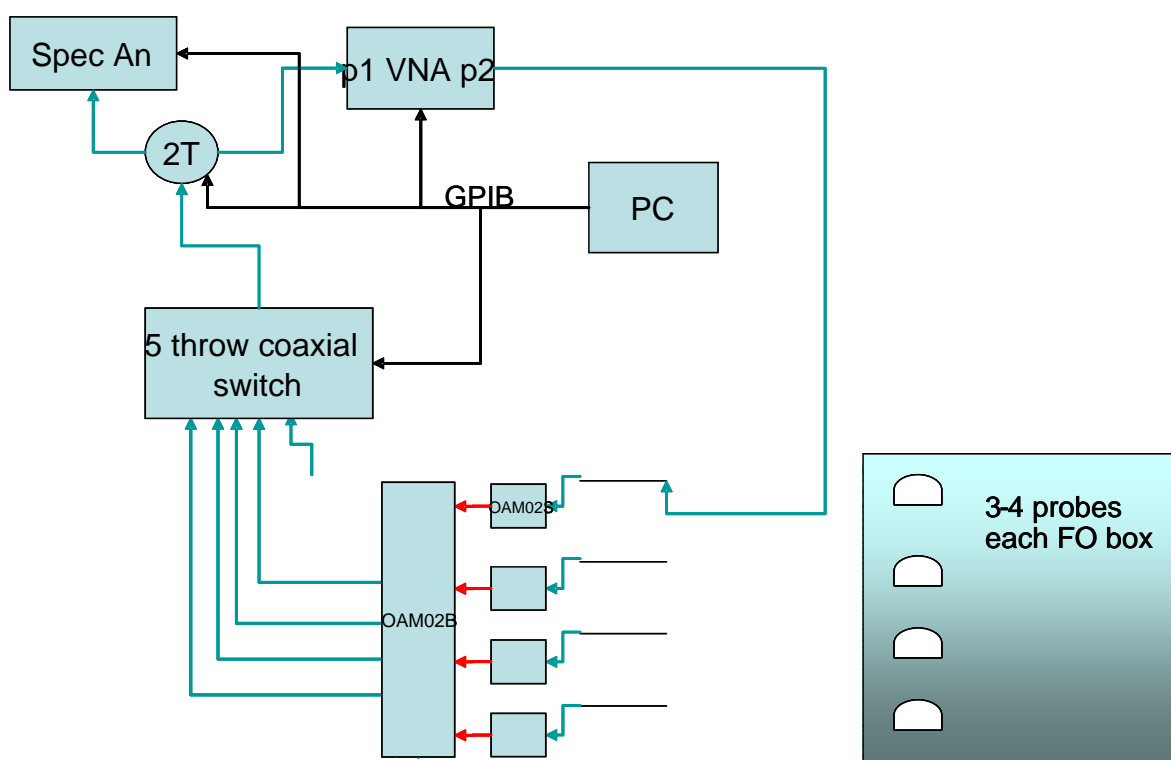
Figure 80   Calibration setup to measure transfer function of the 14 signal paths in receive side of measurement arrangement. The calibration cable combination from VNA port 2, is a combination of coaxial cables capable of reaching the OATS test site from the control room.

- The VNA is set to the standard frequency range for the S12 measurement. (port 2 output, port 1 input) The VNA output power is set to 0 dBm. This should be done by the standard operating software.
- The cables, connectors, switches on the input side (P1) of the VNA are as per the main experiment. The software of the main experiment is run 16 times: once for each connection of the CCC to each <u>flexiform</u>. Each of the 16 files will be 16/17 rubbish, 1/17 useful data.
- The 'Calibration Cable Combination' is connected directly to the second port of the VNA and is long enough to reach the test area, where the other end is connected to the

flexiform cables in turn. A 46 dB attenuator and 30 dB attenuator is connected for each of the 16 runs into the CCC.

- The OAM02S boxes and flexiform cables are in situ on the aircraft.
- The S12 measurement is taken over the calibrated frequency range and saved to file for each flexiform cable end. Both real and imaginary S12 is required – the same as for the experiments themselves. **Measurements are made at both 46 dB and 30 dB attenuator settings – the software will set FOL gain accordingly to approximately the same levels.**
- Symmetry is used to help detect errors between measurements on either side.
- Optical fibre box internal configuration and coaxial switches will be updated for each measurement automatically by the measurement software.
- Additional measurements may be required due to the FOL links using different gains than 44 dB or 30 dB.

Table 5 Run numbers of calibration measurements of receive chain

Cable name	Run number - 46dB attenuator	Run number - 30dB attenuator
Short Cal. cable		
ffLF1		
ffLF2		
ffLF3		
LF4 w/o ff		
ffLR1		
ffLR2		
ffLR3		
ffLR4		
ffRF1		
ffRF2		
ffRF3		
RF4 w/o ff		
ffRR1		
ffRR2		
ffRR3		
ffRR4		

In addition to the above calibration measurement, it is necessary to know the loss and phase shift of the 'calibration cable combination'. First, the VNA is calibrated for the S12 measurement by measuring a standard short calibration cable with 6 dB of attenuation. This short calibration cable will be measured each day that the VNA is used. The 'calibration cable combination' S12 is then measured using two runs of the software by connecting the distant end to the port 1. It is measured with the 46 dB and 30 dB attenuators in series.
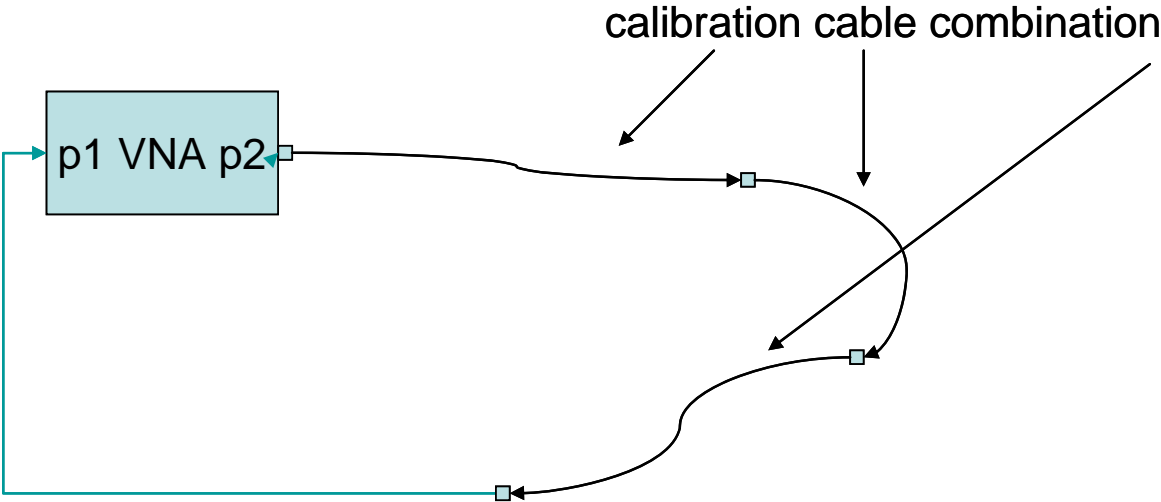
Figure 81   An additional step in the calibration: Measuring the transfer function of the "calibration cable combination" used in the first calibration step, but which is not present in the actual measurements. The aqua line is a diagrammatic connection only.

Description	Run number
Short Cal cable	
46 dB +Cal Cable Combination	
30 dB + Cal cable combination	
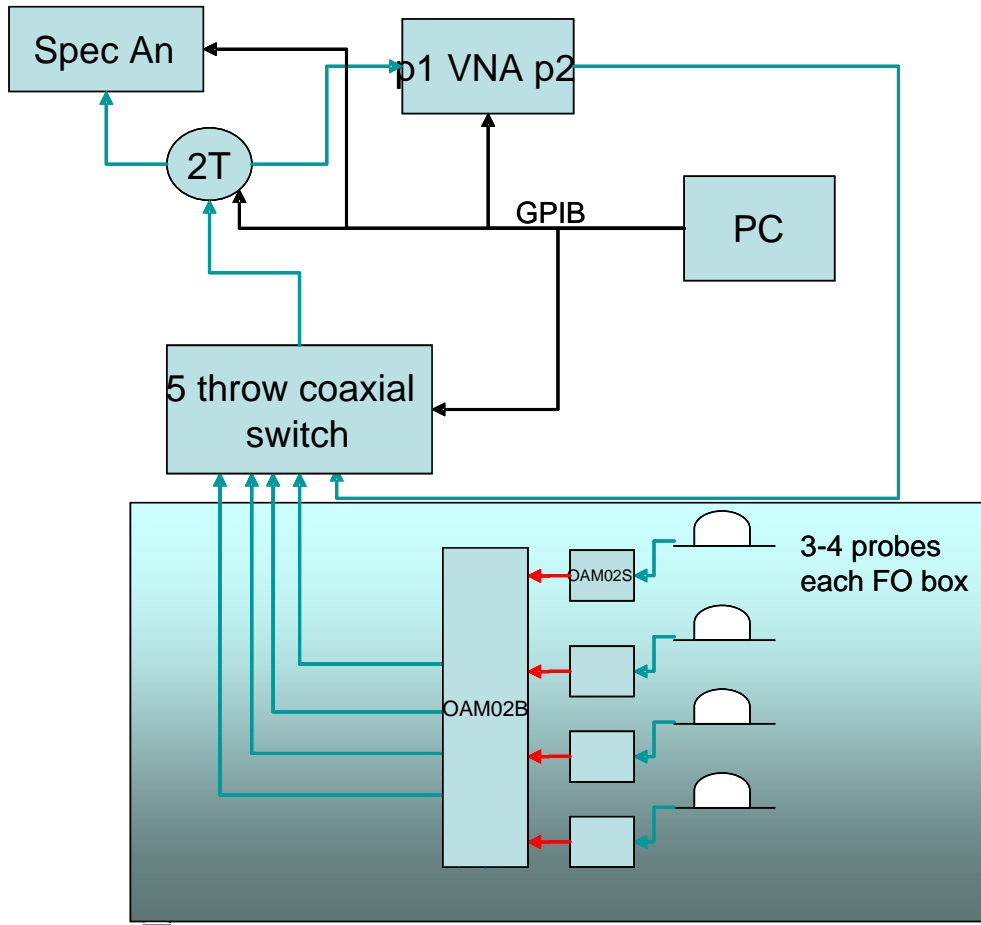
Figure 82 To measure the characteristics of the path from Directional coupler to the VNA port 1, the cable from DC is connected directly to port 2 of the VNA. The shaded area circuits are ignored for this test.

In addition, the path loss and phase change of the path from the directional coupler (-50 dB forward tap), through the coaxial switches to the VNA is measured. This is done simply by running the measurement code, with the power amplifier disconnected and the coaxial from the directional coupler (-50 dB forward tap) connected instead to port 2 of the VNA. The inputs from the loop antennas are polled by the software but the data is ignored in the file.

Table 6 Run number for calibration of DC path

Description	Run number -
Short Cal cable	
DC path	

After the Macchi is removed from the OATS, the OATS is calibrated using the VNA. This effectively measures that (complex) transfer function between the voltage at the output (forward thru) of the directional coupler, and the electric field at the centroid of the Macchi. One of the 14 flexiform inputs is used – ffRF1 – to accept the integrated output of the D-dot probe, and the measurement software is run 8 times – once for each antenna. The LN1000 may also be required.

Table 7 Run numbers for calibration of OATS antennas

Antenna	Run number -
Short cal cable	
Nose V	
Nose H	
Port V	
Port H	
Starboard V	
Starboard H	
Tail V	
Tail H	

A.6.   Measurement of skin currents

A.6.1   Check of HF antenna operation using VNA

A one-port reflection measurement is made on each of the HF antennas. Equivalent antennas (i.e. H polarised and V polarised) are compared to each other in terms of input impedance and resonance frequency. This will detect major alterations of performance due to open connections etc. in the baluns.

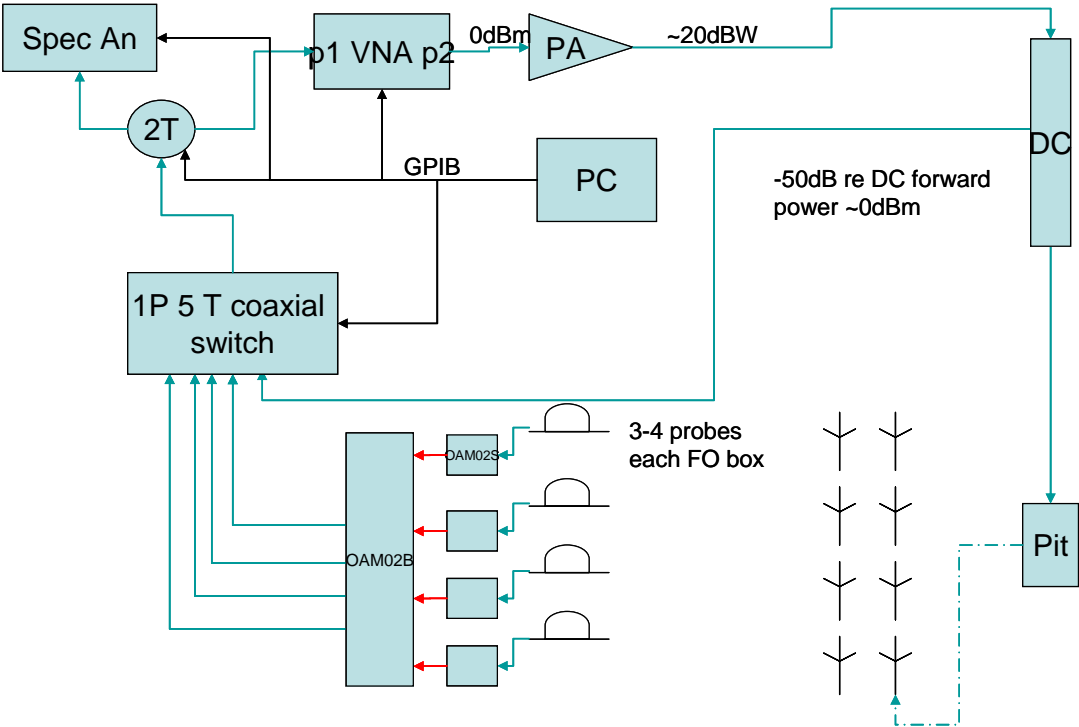### A.6.2   OATS (Antenna driven) measurement of skin currents

Figure 83   Diagrammatic layout of experiment. A computer controlled coaxial switch is used to switch alternately the port one input of the VNA to the directional coupler and the measured skin currents.

The measurement setup is shown in Figure 83.[25] For clarity, only one loop probe is shown connected to each FOL box. However either 3 or 4 loop probes are connected to each FOL box. A PC controlled coaxial switch selects between the received path and the output of the directional coupler.

The measurement procedure is as follows:

- The VNA is calibrated for S12 to 2-50 MHz in 201 steps. (we may have to control this via PC software to avoid loss of cal data)
- VNA is swept at 0dBm output power and the S12 is monitored by switching the coaxial switch to directional coupler input: The analogue gain of the Power Amplifier is adjusted to ensure the measured S12 is a little less than 0dB at all frequencies .
- Default TESEO gain is 30 dB.

The algorithm executed by Labview for data collection is shown in pseudo-code below, and contains two nested loops for TX antenna (outer loop), and skin current probe (inner loop).

- ❖ For each TX antenna (Na) (8 x)
  - ➢ Indicate run number, and request human confirmation/input that appropriate TX antenna is connected
  - ➢ set correct VNA frequency scan 2-50 MHz, 201 steps, S12, and port 2 output power (0 dBm)

  - ➢ set coaxial switch to Dir. Coup. output
  - ➢ 50: measure S12 and display
  - ➢ IF S12 exceeds 0 dB or is <-6 dB at any frequency, pause and alert operator (PA gain may need adjustment) and go to 50 (this loop needs to be able to be disabled to prevent infinite looping in the calibration procedure where the DC is not connected)
  - ➢ save three column by Nf rows ascii file with rows: [frequency(MHz)] [Real(S12)] [Imag (S12)] filename includes run number and 'DC'

  - ➢ For each skin current probe (Ns) (14 x)
    - ▪ Set coaxial switch to measurement path from FOL and TESEO inputs appropriately
    - ▪ 100: measure S12 and display
    - ▪ If S12 is greater than 0dB, reduce TESEO gain to 17 dB and goto 100
    - ▪ save four column file [frequency(MHz)] [TESEOgain(dB)][Real(S12)][Imag (S12)] filename includes run number and 'FOL'
  - ➢ Next Skin current probe
- ❖ Next TX antenna

Files should be placed in a subdirectory which has a name based on the measurement date.

---

25 A double throw coaxial switch, controlled by software is also used to switch the output from the six-way switch to either the VNA or a GPIB controlled spectrum analyser: This is used to check the batteries and performance of the FOL satellites.

Table 8 Run numbers of antenna excited skin current measurements

Antenna	Run number -
Short cal cable	
Nose V	
Nose H	
Port V	
Port H	
Starboard V	
Starboard H	
Tail V	
Tail H	

A.7.   Measurement of bundle currents

The experimental setup is identical to that above except some of the satellite inputs are connected to current transformers on the bundles. The same flexiform cables are used. Up to 14 bundles may be measured. Skin current probes are left in situ.

Table 9 Run numbers of antenna excited bundle measurements

Antenna	Run number -
Short cal cable	
Nose V	
Nose H	
Port V	
Port H	
Starboard V	
Starboard H	
Tail V	
Tail H	

A.8.   Checking procedure for code

Explicit checking of code will not be required, as the calibration procedure uses and checks the code.

A.9.   Measurement of DCI excited skin currents.

The precise setup for the coupling of the RF power to the aircraft is still being finalised (and we may try several during the experiments). However the layout of the measurement equipment will be almost identical:
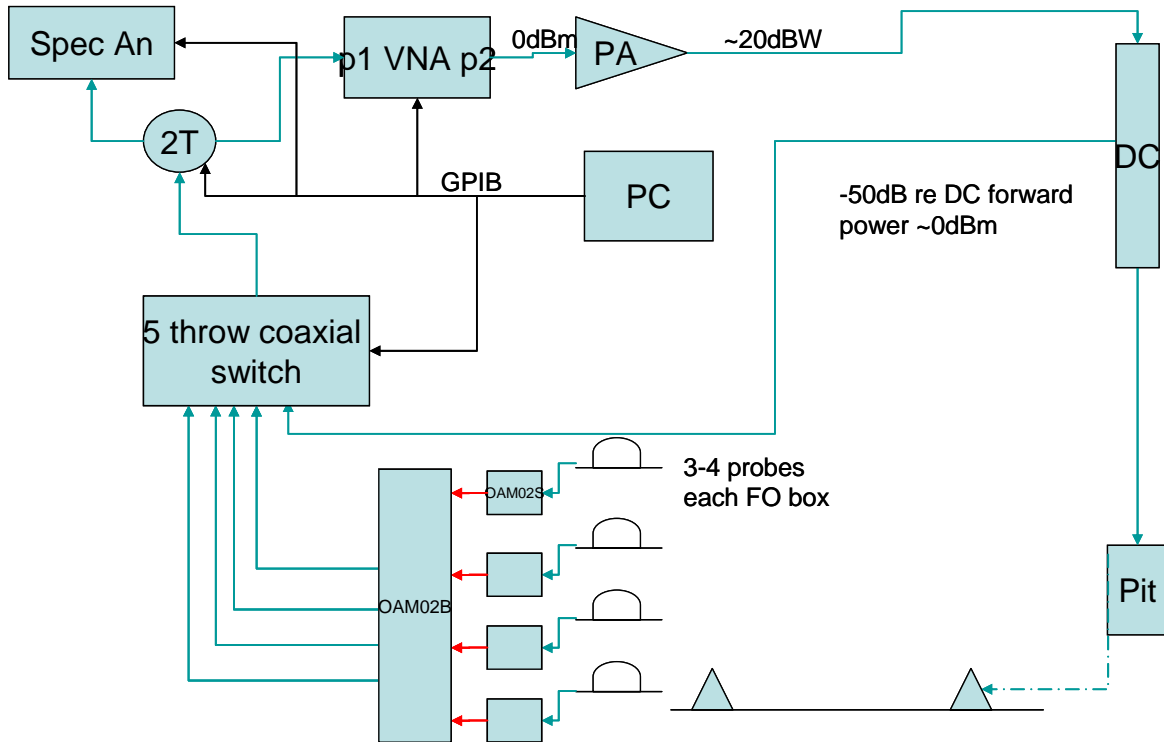
Figure 84 Diagram for measurement of DCI excited skin currents.

One 'DCI' measurement uses a 15 m dipole supported in close proximity (~0.3 m) above the fuselage.

Table 10 Run numbers of nearfield dipole excited skin currents.

Antenna	Run number -
Short cal cable	
Above Macchi	

Table 11 Run numbers of nearfield dipole excited bundle current measurements

Antenna	Run number -
Short cal cable	
Above Macchi	

The other method uses a set of four pyramid structures with the aircraft on its wheels. One pyramid is powered and the other three are connected to 50 ohm, 100 W loads through their N connectors at the base. Three of the pyramids will be powered: nose, right wingtip and tail.

Table 12 Run numbers of DCI skin currents

Driven Pyramid	Run number -
Short cal cable	
Nose	
Tail	
Starboard wingtip	

Table 13 Run numbers of DCI excited bundle measurements

Driven Pyramid	Run number -
Short cal cable	
Nose	
Tail	
Starboard wingtip	

A.10. Order of Work

- Writing of code; next :checking of code combined with calibration.
- calibration of 14 receive side paths: 14 runs of measurement software; infinite loop for Dir. Coupler disabled; power amplifier not used.
- calibration of CCC: measured manually
- calibration of path from dir. coupler out (-50 dB) to VNA: 1 run of software. **No radiation to the atmosphere in any prior stage. Target date for completion: 3/3/06**
- measurement of OATS (antenna) skin currents: 8 runs of software. **Target date for test 13-17/3/06**
- Setup nearfield dipole
- measurement of 'nearfield dipole' skin currents (1 run of software). **Target date for test 23-24/3/06**
- setup to measure bundle currents (satellites inside, current clamps)
- measurement of 'nearfield dipole' bundle currents (1 run of software) **Target date for test 3-4/4/06**
- stripdown of nearfield dipole
- measurement of OATS (antenna) bundle currents (8 runs of software) **Target date for test 5-7/4/06**
- lower Macchi to U/C; change wings; install pyramids
- measurement of DCI bundle currents (3 runs of software) **Target date for test 24-28/4/06**
- setup to measure skin currents (satellites outside, skin probes)
- measurement of DCI skin currents (3 runs of software) **Target date for test 1-5/5/06**
- remove Macchi from site
- calibration of site (8 runs of software) **Target date for test 15-16/5/06**

This page intentionally left blank

Appendix B: J-dot Probes

B.1. Purpose

The DSTO E3 team is developing J-DOT probes to enable skin current measurements on the Macchi when excited on the OATS and with Direct Current Injection, and possibly a full scale TEM cell. Multiple copies of the J-DOT probe will be constructed and attached to the Macchi skin at selected locations to simultaneously measure the vector components of skin current density. The J-DOT probe's sensitivity, though capable of theoretical calculation, needs to be measured. In addition, it needs to be determined:

- Whether the presence of aircraft paint or other insulating films will affect the accuracy of the skin current measurement, and
- The degree to which the J-DOT probe is sensitive to skin charges (i.e. normal electric fields)

The purpose of this test is to calibrate the power output (dBm) of the J-DOT probes relative to skin current density (A/m). The skin current on the TEM cell septum will be used because DSTO AMS has well validated models that include the septum current density and adjacent magnetic and electric field levels across the required frequency band.

Inadequate sensitivity to current, or excessive probe inductance, or sensitivity to surface charge may require a probe redesign.

B.2. J-DOT probes

The J-DOT probe is a balanced-feed half-loop working against a ground plane. The loop is formed of thin copper strap of width 20 mm and radius 80 mm. Semi-rigid coax is used to bring the feed out from the tapered feed gap at the centre. Dummy coax is used on the opposite half of the loop to enhance balance. The thin, brass sheet ground-plane is intended to be sufficiently flexible to conform to the curvature of the aircraft skin, to which it will be attached with self tapping screws[26].
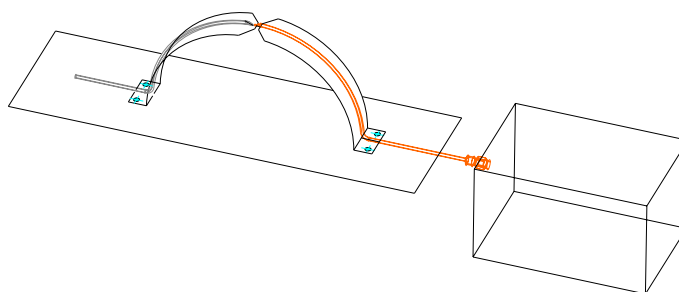

Figure 85 schematic of J-dot probe and Fibre Optic satellite.

---

26 The measurements will be taken on a de-commissioned Macchi, on which drilling of holes is acceptable.

B.3. Equipment setup:

The equipment setup will be identical to that used in the latest TEM cell measurements, that is, frequency, forward and reflected power and electric field components will be measured and recorded. In addition, the software will continue to ensure that resonances don't create field strengths hazardous to the E field probes.

The main differences between this test and the previous test is the recording of received power level from the J-DOT probe attached to the septum. The probe will be attached in two orientations, and both with and without paint layers on the septum at its installation site. This will result in 4 test runs. The measurements with loop plane horizontal will measure the skin current sensitivity. The measurements with loop plane vertical will measure skin charge sensitivity. In the latter case, some slight tweaking of the probe orientation may be necessary to ensure that it is exactly transverse to the skin currents on the septum. Sensitivity to skin charge is undesirable since it will be difficult to determine from the subsequent field measurements how much of the total output of the loop is due to skin currents alone.

The J-DOT data is recorded via the FO link. Various FO gains may be needed to optimise the S/N ratio. The gains used will also need to be recorded. The other differences are:

- An increased frequency step size of 500 kHz
- A reduced frequency range requiring one PA (1 MHz-80 MHz)
- Software needs to ensure power level into the FO satellite remains safe (<0 dBm) and that SNR is adequate (scale gain or power input).

B.4. Expected sensitivity

To help with adjusting gains, the expected maximum sensitivity of the J-DOT probe relative to nett TEM cell input power has been calculated:
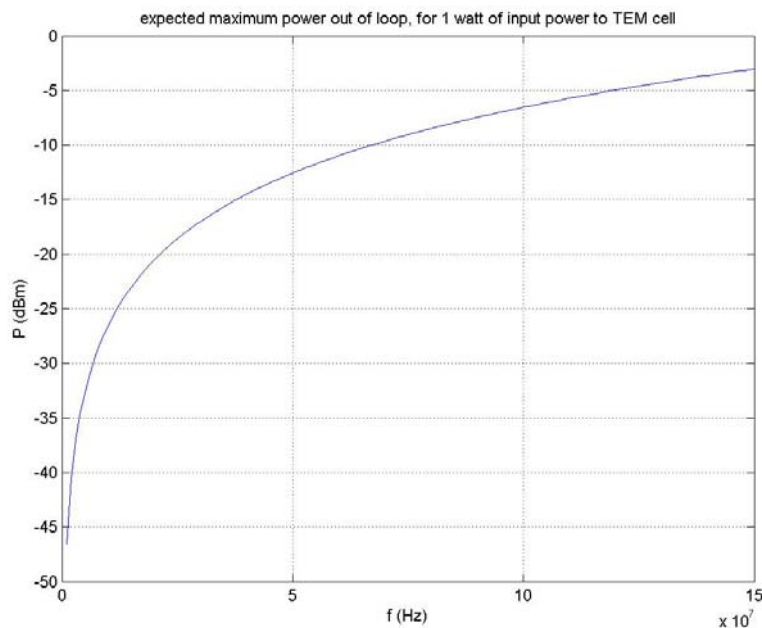

Figure 86 Expected power output from probe, neglecting probe inductance

It can be seen that at 80 MHz, a level of –6 dBm will be produced for a TEM cell input of 1 W. The absolute maximum power input to the TEM cell would therefore be 4 W at 80 MHz, to protect the input to the FO link. (unless an attenuator is used) Sensitivity increases by 6 dB per octave, and at 10 MHz, the sensitivity is –24 dBm for 1 W input. Below 10 MHz, therefore, 100 W of PA power can be used.

The sensitivity varies by 36 dB over the frequency range measured. A combination of PA power changes and FO gain should be used to ensure that the Signal to Noise Ratio remains adequate (>20 dB), and the input power to the FO remains below 0 dBm.

B.5.   Data recorded

- Frequency,
- Forward power,
- Reverse power,
- E field components,
- Spec. An. power,
- FO link gain. (or the latter two combined and recorded as J-DOT power)

B.6.   Test Results:

B.6.1   Sensitivity to current density parallel to the loop plane

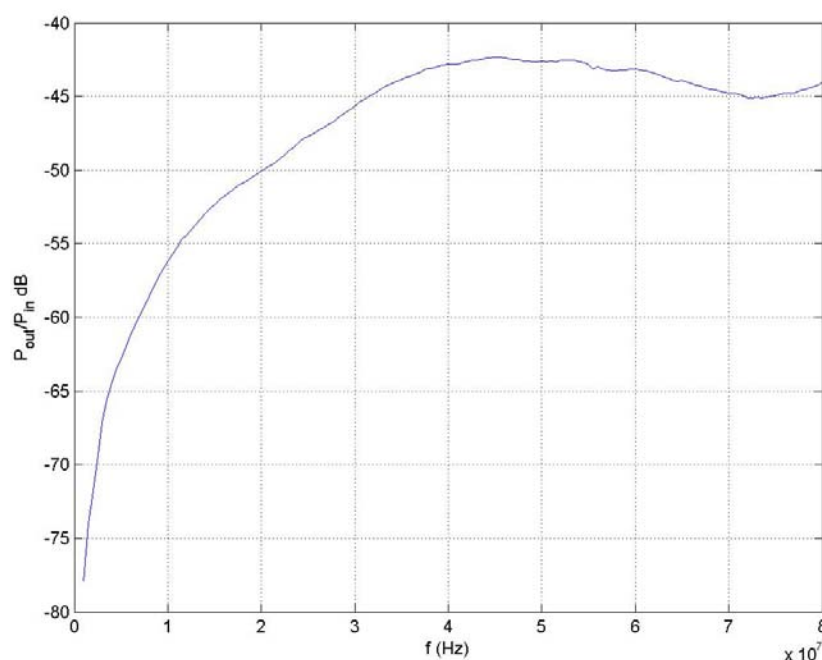*Figure 87   Measured output power (dBW) for one Watt input power to TEM cell*

The received power, after adjusting for Fibre Optic Link gain relative to a nett input power of 1 W is shown in Figure 87. This figure may be compared with Figure 86. It can be seen that both plots commence at 1 MHz with a level of –77 dBW (-47 dBm). At 50 MHz, the measured value is –43 dBW, which also agrees with the figure 1 value of –13 dBm.

A useful measurement parameter, which factors out the time derivative effects is the apparent area, A_{ap}, of the probe into 50 ohms, which is analogous to the equivalent area of a D-dot probe. The voltage out of the probe can be written:

$$v = \dot{B}A_{ap} = \mu H\, 2\pi f A_{ap}$$

Inverting the above,

$$A_{ap} = \frac{v}{2\pi f \mu H} = \frac{\sqrt{50P}}{2\pi f \mu H}$$

where P is the power into 50 ohms, and H is the magnetic field strength immediately adjacent the conducting surface. H can be shown using Maxwells curl equation for magnetic field to equal to the current density on the conducting surface.

We can also calculate the apparent probe area based on the physical area of the loop and using a value of inductance obtained from numerical modelling of a similar loop.
The physical area of the loop:

$$A_o = \frac{1}{2}\pi r^2 = 0.01 m^2 \text{, using 80 mm for the radius.}$$

A voltage divider approach can be used to calculate the apparent area from the physical area, by treating the loop as a lumped circuit consisting of a voltage source and a series inductor feeding the 50 ohms resistive impedance of the cable:

$$A_{ap} = A_o \frac{50}{50 + j2\pi f L}$$

Inductance values varied between 0.155 uH and 0.175 uH for a FEKO model of a loop without tapered feed area and associated soldered feed connections. A value of 0.2 uH was found to fit the measured data well and to be consistent with the above modelling, when the effects of tapered feed and soldered wire connections are taken into account. The modelled and measured data are compared in Figure 88. It can be seen that the measured and modelled data agree within about 1 dB generally. The variations may be ascribed to errors in the TEM cell model from which local values of magnetic field strength were obtained as well as to measurement errors including non-linearities in the fibre-optic links.
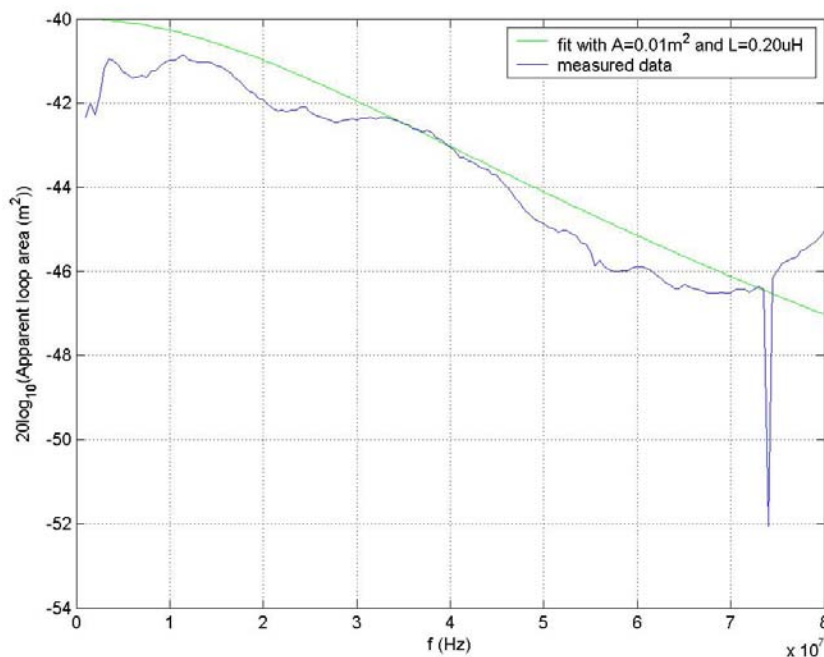
Figure 88 Measured and theoretical apparent loop area compared. Note the use of the dB scale for area for which 0.01 square metre is -40 dB square metres. This is appropriate since area is proportional to output voltage.

The probe is intended to measure surface current density, so the sensitivity can be conveniently expressed as

$$P = k\dot{J}^2 = k'J^2$$

where

$$k = magnitude\left(\frac{(\mu A_{ap})^2}{50}\right) = magnitude\left(\frac{50\mu^2 A_o^2}{(50 + j2\pi f\, 2E - 7)^2}\right)$$

and

$$k' = magnitude\left((2\pi f)^2\frac{(\mu A_{ap})^2}{50}\right) = magnitude\left(\frac{(2\pi f)^2 50\mu^2 A_o^2}{(50 + j2\pi f\, 2E - 7)^2}\right)$$
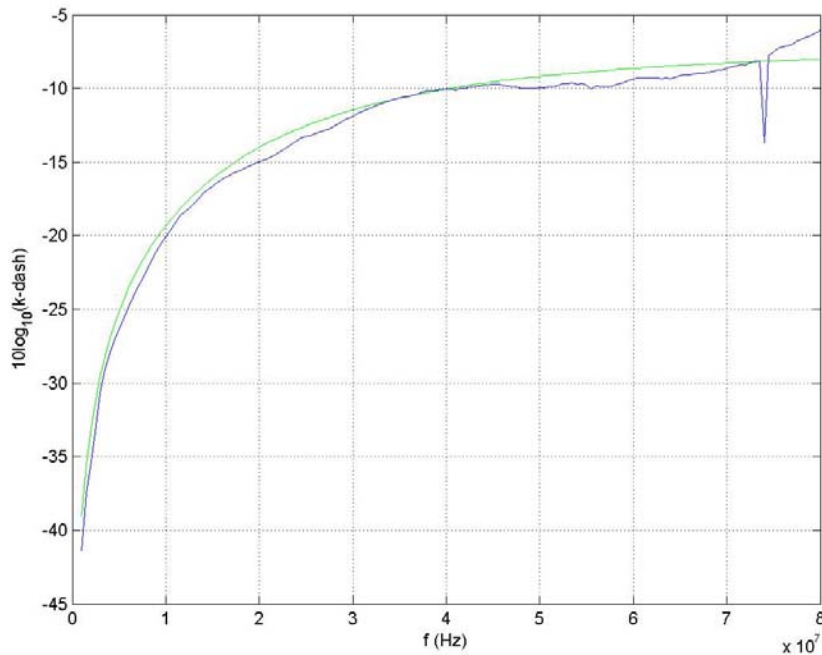
Figure 89 Comparison of sensitivity factor k' between theory and measurement. k' provides the link between squared current density and received power, and has the units Wm²/A².

When using the above equation for k' users should compare against the data of Figure 89, or note that at 10 MHz, k'=0.0117 Wm²/A².

B.6.2 Sensitivity of output to painted or insulated surfaces

One of the objectives of the measurements was to ensure that the calibrated sensitivity of the probes was not strongly dependent on the presence of paint layers on the aircraft's skin causing the ground plane of the loop to be insulated from the metal layer actually carrying the current. The septum of the TEM cell was painted with spray enamel under the probe contact area , and the output power of the probes measured again. The results are shown in Figure 90. The difference between the two cases is very small and is probably due to random experimental error as much as to the effects of the paint layer.

Figure 90   A comparison of probe output power measured before and after the application of a paint layer between the probe and the septum. The data have not been normalised to input power or current density.
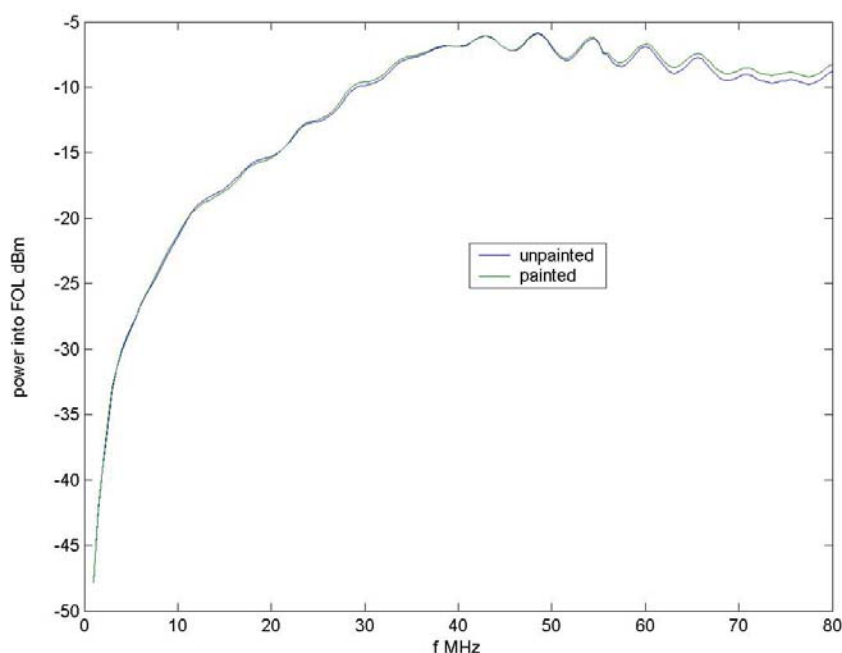
B.6.3   Sensitivity to electric charge.

This probe is intended to measure the flow of charge parallel to the loop plane, by measuring the adjacent magnetic field. However it is also inevitable that time varying charge density, on the surface to be measured, will also induce some output from the probe. The mechanism for this is as follows: The normal electric fields produced by the charges will interact with the two quarter-loop arms of the loop, which may be thought of as monopole antennas. Any asymmetry in the two arms will then result in a differential voltage between the arm ends, to which the feed is sensitive.

A method was used to determine an upper bound to the E field sensitivity of the probe, by positioning the probe transverse to the current flow direction on the septum. While the resulting output signal may be due to current effects from imperfect transverse orientation, the method at least provides an upper bound for the electric field sensitivity. It might be thought that an orientation of the probe could be found where the current generated output exactly cancelled the charge-derived output. This is most unlikely however.
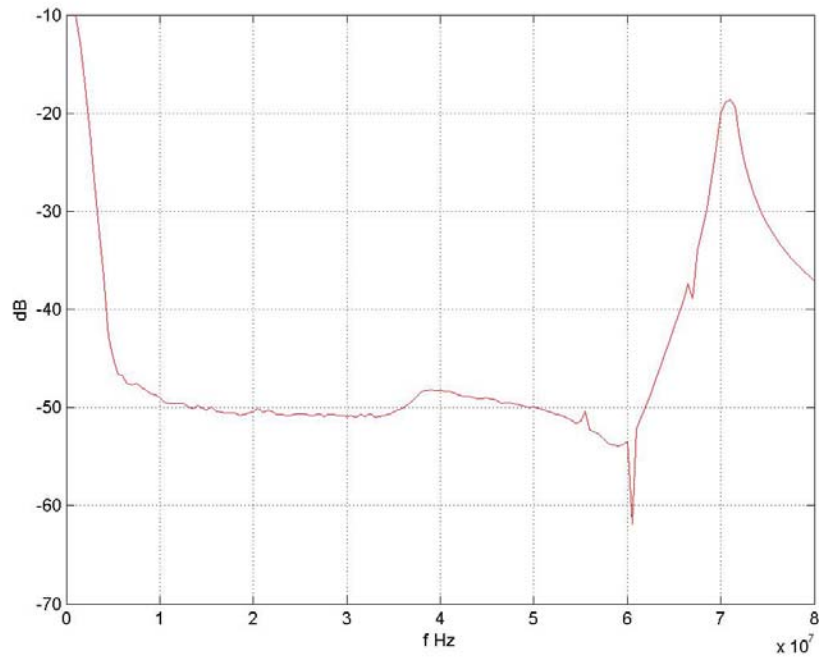
*Figure 91   Power output from the probe when oriented with the loop vertical, relative to power output
when oriented horizontally on the TEM cell septum.*

In Figure 91, the output power when transverse, minus the output power when parallel to the
TEM cell septum axis is shown. Over most of the range, the level is seen to be down by 50 dB.
At the low frequencies, the rise is due to a DC error in the spectrum analyser being viewed
though the resolution bandwidth of 3 MHz. At 70 MHz, the high output power was found to
be due to a cross-septum resonance occurring in the TEM cell, to which the J-dot probe has
legitimately responded. This cross-septum resonance is not expected to be a problem in the
TEM cell as it can be seen to be 20 dB below the main (parallel to axis) mode.

Using the –50 dB figure, and treating the J-dot probe as a D-dot probe, we obtain an
equivalent area in the D-dot mode as less than 2.5% that of the J-dot probe:
Now,

$$V_{Ddot} = 50 A_{eq}^{Ddot} \varepsilon \dot{E} \leq 10^{-50/20} A_o \mu \dot{J}$$

and using the fact that $\dot{J} = \dot{H}$ and $E/H = \eta$

$$A_{eq}^{Ddot} \leq \frac{\mu}{50\varepsilon\eta} 10^{-50/20} A_o,$$

hence

$$A_{eq}^{Ddot} \leq 0.0239 A_o.$$

B.7. Summary

Table 14 J-dot probe calibration results

J-dot Probe equivalent area A_o (not corrected for inductance) (m²)	0.01
Probe inductance, L (uH)	0.2
Intended frequency range (MHz)	1-60
Probe apparent area (corrected for inductance into 50 ohms) (m²)	$A_{ap} = A_o \dfrac{50}{50 + j2\pi fL}$
Probe equivalent area as a D-dot probe (m²)	$A_{eq}^{Ddot} \leq 0.024 A_o$

This page intentionally left blank

Appendix C: Skin current validation.

C.1. Direct Current Injection

In this section the plots comparing modelling and measurements of skin current density at 14 directed locations are indexed. The plot figures are on the attached CDROM

In all the DCI cases, the model and experiment had the following conditions:
- A 1V peak forward propagating wave in the coaxial line is applied.
- In the model, this is approximated by a 2V peak voltage source loaded with a 50 ohm series resistor.
- In the measurements, the calibration measurements are combined in such a way as to achieve equivalence to a 1V peak, zero phase, incident wave on the coaxial line arriving at the side junction in the source pyramid. This represents a slight difference compared to the model in that the phase delay inside the pyramid is not taken into account. The difference can be expected to cause a linearly increasing error in phase up to 1.5 radians at 30 MHz.
- 50 ohm loads are applied.
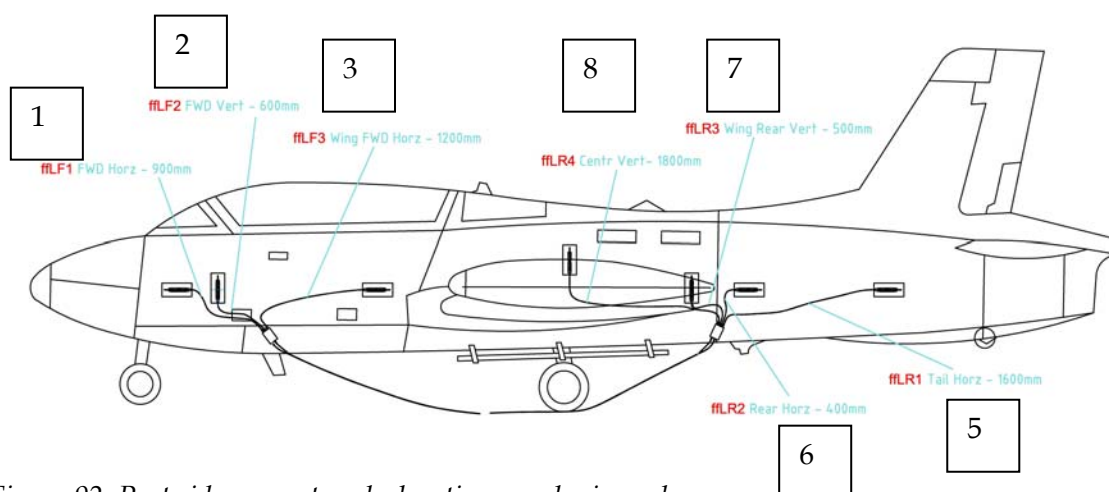
Figure 92 Port side current probe location numbering scheme
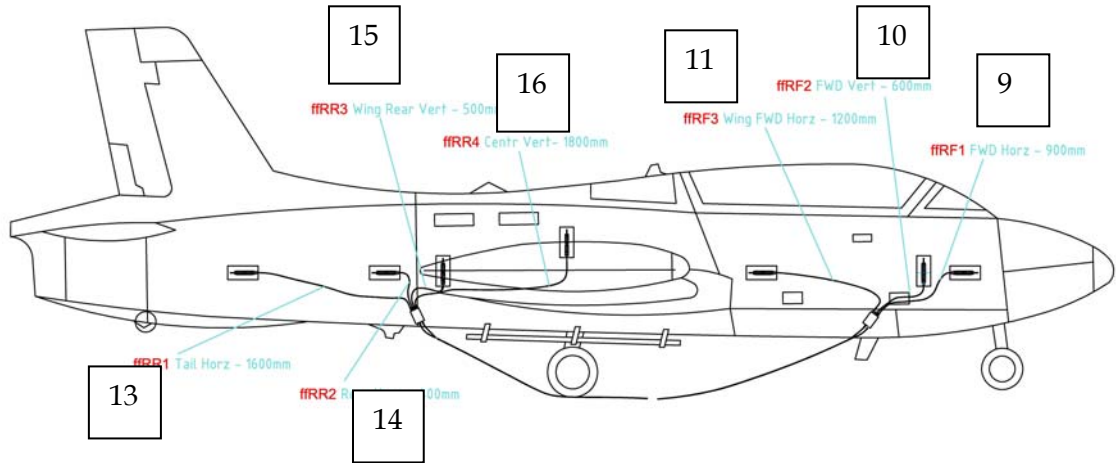
Figure 93 Starboard side skin current probe numbering scheme

The figures showing the comparison between numerical model and measurements for the various measurement locations are contained on the attached CDROM.

For the tail driven case, the directory is /DCI model validation/Tail driven/. The filenames are as shown in the Table 15

Table 15 CDROM file names for the DCI Tail Driven validation figures.

Current location	Magnitude file name	Phase file name
1	tailmag1	tailphase1
2	tailmag2	tailphase2
3	tailmag3	tailphase3
5	tailmag5	tailphase5
6	tailmag6	tailphase6
7	tailmag7	tailphase7
8	tailmag8	tailphase8
9	tailmag9	tailphase9
10	tailmag10	tailphase10
11	tailmag11	tailphase11
13	tailmag13	tailphase13
14	tailmag14	tailphase14
15	tailmag15	tailphase15
16	tailmag16	tailphase16

For the nose driven case, the directory is /DCI model validation/Nose driven/. The filenames are as shown in the Table 16

Table 16 CDROM file names for the DCI Nose Driven validation figures

Current location	Magnitude file name	Phase file name
1	nosemag1	nosephase1
2	nosemag2	nosephase2
3	nosemag3	nosephase3
5	nosemag5	nosephase5
6	nosemag6	nosephase6
7	nosemag7	nosephase7
8	nosemag8	nosephase8
9	nosemag9	nosephase9
10	nosemag10	nosephase10
11	nosemag11	nosephase11
13	nosemag13	nosephase13
14	nosemag14	nosephase14
15	nosemag15	nosephase15
16	nosemag16	nosephase16

For the wing driven case, the directory is /DCI model validation/Wing driven/. The filenames are as shown in the Table 17.

Table 17 CDROM filenames for the DCI Wing Driven validation figures

| Current location	Magnitude file name	Phase file name
1	wingmag1	wingphase1
2	wingmag2	wingphase2
3	wingmag3	wingphase3
5	wingmag5	wingphase5
6	wingmag6	wingphase6
7	wingmag7	wingphase7
8	wingmag8	wingphase8
9	wingmag9	wingphase9
10	wingmag10	wingphase10
11	wingmag11	wingphase11
13	wingmag13	wingphase13
14	wingmag14	wingphase14
15	wingmag15	wingphase15
16	wingmag16	wingphase16
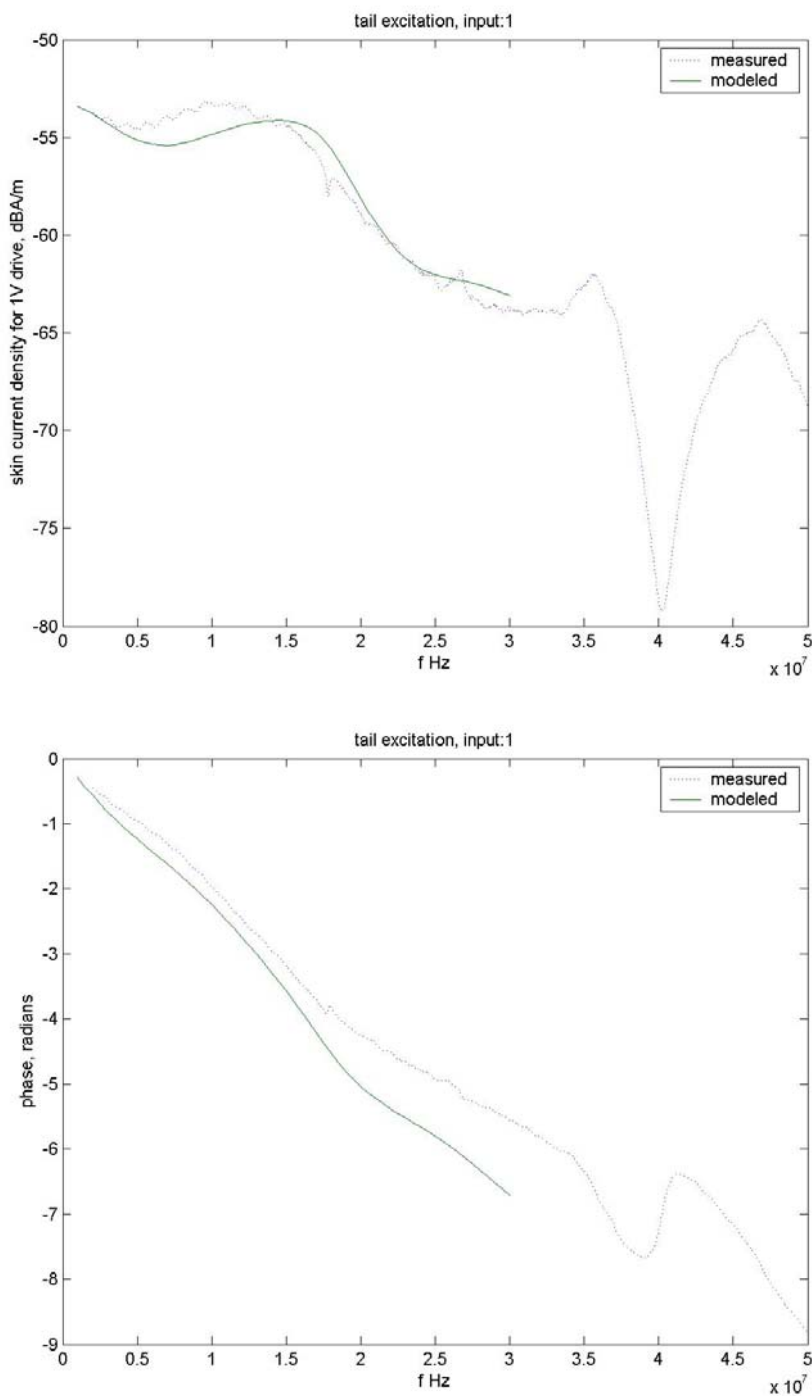
Figure 94   An example comparison for one current location of DCI model and measurement current densities and phases. In this case location 1 is shown. The other figures are in the CDROM.

C.2.   Low Level Swept Coupling validation

In this section the plots comparing modelling and measurements of skin current density at 14 directed locations are indexed. The plot figures are on the attached CDROM

The only situation modelled was for a horizontally polarised antenna abeam and to port of the aircraft as shown in Figure 41.

Current location	Magnitude file name	Phase file name
1	OATSSH6Emag1	OATSSH6Ephase1
2	OATSSH6Emag2	OATSSH6Ephase2
3	OATSSH6Emag3	OATSSH6Ephase3
5	OATSSH6Emag5	OATSSH6Ephase5
6	OATSSH6Emag6	OATSSH6Ephase6
7	OATSSH6Emag7	OATSSH6Ephase7
8	OATSSH6Emag8	OATSSH6Ephase8
9	OATSSH6Emag9	OATSSH6Ephase9
10	OATSSH6Emag10	OATSSH6Ephase10
11	OATSSH6Emag11	OATSSH6Ephase11
13	OATSSH6Emag13	OATSSH6Ephase13
14	OATSSH6Emag14	OATSSH6Ephase14
15	OATSSH6Emag15	OATSSH6Ephase15
16	OATSSH6Emag16	OATSSH6Ephase16

This page intentionally left blank

Appendix D: Comments on BCI from Mr M. Bolsover

The following is an extract of comments upon the matter of BCI and LLSC fidelity and practicality issues provided to the author as part of review comments upon this document.[16]

- The use of individually shielded or over-braided wiring effectively shorts the BCI injection probe to ground. This has several implications
    o If the cable loom is segmented by bulkhead with the shields terminated at the bulkhead disconnects then only the coupling associated with the segment injected upon will be represented at best. This can change not only the amplitude of the current required to represent a particular HIRF threat but also the frequency at which the maxima occurs (bear in mind that the individual wires inside a bundle can effectively have electrical lengths many times greater than the shielded segment terminated for example at an LRU and bulkhead disconnect)
    o The use of Break-out boxes during both the LLSC and BCI phase is necessary to overcome this limitation, however the practicality of furnishing multiple different break-out boxes (necessarily built using expensive and invariably scarce aircraft connectors and wiring practices) for complex systems is both time consuming and expensive and in practice rarely justifiable to a project.
    o A current certification practice is to disconnect shields to prevent the shorting of the injection probe, however the true impact this has on the system performance can at best only be guessed and is far from satisfactory (Shift in resonance, diversion of current from the natural low impedance path, removing the coupling attributed to the surface transfer impedance to name but a few factors)

- Increasingly densely packaged avionics compartments make installing even a single current probe difficult. The need to install the injection probe as well and maintain separation from the structure and monitor probe in many cases is impossible
- Complex Multi-channel systems utilise voting techniques to establish data validity, injecting on a single channel is not an acceptable technique of testing such a system since the stressed channel may be voted out and the threshold of a system upset may go undetected. Multi-Loom and Multi-point BCI has severe limitations since in practice different looms often share common wires or branches so current balancing in transfer function ratio is in many cases impractical. (one of the injection points tends to drive multiple looms sharing common wires)
- BCI on bundles containing relatively low impedance power supply wiring can drive current onto electrical bus-bars that can in turn stress systems sharing the bus but not intended as part of the test. Some less critical systems with lower levels of protection can suffer damage
- Since the monitor probe only measures common mode current, the actual stress on individual wires in a bundle is not known. Individual wires can carry currents orders of magnitude higher than the common mode currents measured on the bundle, which can result in unknown levels of stress at the LRU. This has implications with re-certifying the LRUs as free from damage post-test. In the reviewers experience one particular manufacturer insisted on having a complete set of weapons systems LRU´s quarantined and used only for BCI testing. This particular manufacturer would not re-certify these units for flight even though they passed the ATP and Functional Tests on the grounds that unknown stresses were imposed during BCI. (as an aside this reviewer has observed on more than one occasion the progressive apparent "hardening" of a system repeatedly subjected to BCI under controlled conditions. Clearly some lasting change to the internal LRU circuitry was occurring but the specific mechanism and any non-observed side effects were unquantifiable). Whilst this overstressing phenomenon is not unique to BCI, it could be argued that the localised injection close to a particular LRU, where the LRU represented the lower impedance current path relative to the extended wiring bundle on a simple potential divider principle would exacerbate the effect in the case of BCI.

- Local ground wires also short out the current probes and should not be included in the injection probe. In practice they are often integral to a wire bundle at least for part of the routing and removal for test purposes often difficult or impractical.

Even in the laboratory qualification environment BCI is reaching its practical limitations. The increasing use of well shielded cables may require the partial or complete disconnection of the shields during testing in order to stress the core wires. In the case of lightning pulse testing it is then required to measure the Surface Transfer Impedance for the cable bundle shield combination to define the relationship between shield currents and internal core wire levels. This technique is now appearing in standards such as DO160E for Lightning Pulse testing (RTCA DO160E, section 22, para 22.5.2). For Conducted Susceptibility testing this same standard requires the isolation of bulkhead terminated shields to ensure that a representative length of inner core wire is stressed during testing (see RTCA DO160E, section 22, para 20.4.c).

One of the problems with LLSC which is not touched on is that over the frequency range considered by this report, the aircraft is usually in the near field. In fact it is often the case that the aircraft extremes such as a wing tip can be very close (typically 5 m) from the illuminating antenna in some cases. Effects have been observed which would indicate the antenna is driving the aircraft extreme i.e. acting as a point source almost akin to the DCI technique itself.

DEFENCE SCIENCE AND TECHNOLOGY ORGANISATION DOCUMENT CONTROL DATA		1. PRIVACY MARKING/CAVEAT (OF DOCUMENT)	
2. TITLE The Safety of Aircraft Exposed to Electromagnetic Fields: HIRF Testing of Aircraft using Direct Current Injection		3. SECURITY CLASSIFICATION (FOR UNCLASSIFIED REPORTS THAT ARE LIMITED RELEASE USE (L) NEXT TO DOCUMENT CLASSIFICATION) Document　　　　　(U) Title　　　　　　　(U) Abstract　　　　　(U)	
4. AUTHOR(S) Chris Leat		5. CORPORATE AUTHOR DSTO Defence Science and Technology Organisation PO Box 1500 Edinburgh South Australia 5111 Australia	

6a. DSTO NUMBER DSTO-RR-0329	6b. AR NUMBER AR-013-938	6c. TYPE OF REPORT Research Report	7. DOCUMENT DATE June 2007

8. FILE NUMBER 2007/1013393/1	9. TASK NUMBER AIR 06/007	10. TASK SPONSOR DGTA	11. NO. OF PAGES 106	12. NO. OF REFERENCES 16

13. URL on the World Wide Web http://www.dsto.defence.gov.au/corporate/reports/DSTO-RR-0329.pdf	14. RELEASE AUTHORITY Chief, Air Operations Division

15. SECONDARY RELEASE STATEMENT OF THIS DOCUMENT *Approved for public release* OVERSEAS ENQUIRIES OUTSIDE STATED LIMITATIONS SHOULD BE REFERRED THROUGH DOCUMENT EXCHANGE, PO BOX 1500, EDINBURGH, SA 5111
16. DELIBERATE ANNOUNCEMENT No Limitations
17. CITATION IN OTHER DOCUMENTS　　　　　　　　Yes
18. DEFTEST DESCRIPTORS Avionics Electromagnetic Environments; Electromagnetic Compatibility Testing

19. ABSTRACT
Even the original developers of Bulk Current Injection now make the point that the use of BCI at aircraft level will become increasingly difficult. Direct Current Injection has the potential to replace aircraft level BCI, while also solving many of the longstanding problems of BCI. These problems include lack of synergism, inaccurate current distribution within bundles and limited numbers of injection sites due to time and cost considerations. However, calibration, the question of how much power to apply as a function of frequency, is much more complex to answer for DCI than BCI. One potential method of calibration, the use of modal skin currents, is developed in this work. This is the first time that DCI calibrated using skin-currents has been shown to generate cable currents which are at least as accurate as BCI. Power levels of approximately 20 kW are required for small aircraft. Numerical modelling based on Method of Moments, and skin and bundle current measurements are employed.